Spring 5-25-2019

Catalysis by Design: Predicting Materials with Fischer Tropsch Catalytic Activity

Suraj Gyawali
Louisiana Tech University

CATALYSIS BY DESIGN: PREDICTING MATERIALS WITH FISCHER TROPSCH CATALYTIC ACTIVITY

by

Suraj Gyawali, BS., MS

A Presented in Partial Fulfillment
of the Requirements of the Degree
Doctor of Philosophy

COLLEGE OF ENGINEERING AND SCIENCE
LOUISIANA TECH UNIVERSITY

May, 2019

LOUISIANA TECH UNIVERSITY

THE GRADUATE SCHOOL

_____
Date

We hereby recommend that the prepared under our supervision by xxxxxxxxxxxxxxx

Suraj Gyawali, BS., MS

entitled **Catalysis by Design: Predicting Materials with Fischer Tropsch Catalytic Activity**

be accepted in partial fulfillment of the requirements for the Degree of

Doctor of Philosophy in Engineering

_____
Supervisor of Research

_____
Head of Department

College of Engineering and Science

Department

Recommendation concurred in:

_____

_____

Advisory Committee

_____

_____

Approved:

Approved:_____

_____ _____
Director of Graduate Studies Dean of the Graduate School

_____Dean of the College

GS Form 13
(8/10)

ABSTRACT

Experimental work has been extensive in the catalysis field; however, the cost to move nano-engineered catalysts from the laboratory to industry using only experimental research is prohibitively high. Macroscopic phenomena (i.e. melting, defect formation, miscibility) can be understood in terms of the nano-scale mechanism using molecular simulations. Thus, using molecular simulations in combination with experiments lowers the costs related to design, as simulations can be used to rapidly screen candidate materials, so that experimental efforts can be limited to the catalyst candidates deemed as most promising by simulations. This work employs molecular simulation tools to predict the relative effectiveness of Fischer-Tropsch catalysts. The study presented in this work has concentrated on 3d (Co, Fe, Ni) and 4d (Ru) metal clusters formed by pure and binary metal combinations of these elements, as they are the ones known to exhibit Fischer-Tropsch activity.

Regardless of how the Fischer-Tropsch process takes place on a given catalyst material, all Fischer-Tropsch mechanisms proposed to date begin with a first and crucial step, which is the adsorption of CO onto the catalyst surface. The CO adsorption onto the catalyst surface is followed by its dissociation to further formation of long-chained hydrocarbons. Thus, CO adsorption and dissociation energies are hypothesized in this work to be predictors of the effectiveness of a given Fischer-Tropsch catalyst, aiding in the search and design of the most efficient material for this process.

First principle calculations on pure nanoclusters based on CO adsorption and dissociation on iron, cobalt, nickel, and ruthenium without support provides a starting reference for the study of this material as a Fischer Tropsch catalyst. These calculations were carried out using the Generalized Gradient Approximation (GGA) functional RPBE, with the double numerical polarization (DNP) basis set. Our results show that cobalt and iron based bimetallic nanoclusters in a core-shell arrangement containing 14 total atoms with the 10:4 Co to iron ratio and vice versa have stronger cohesive energy than the pure 14 atom clusters of the respective elements, as well as any other bimetallic combinations. The bimetallic cluster in a core-shell arrangement containing 14 atoms in total with the 10:4 Co to iron ratio shows the best CO adsorption and its bond breaking for later release. Similarly, 13 atom clusters with icosahedron symmetry were identified as the most stable symmetry at this theory level. Our study reveals that pure ruthenium and Co clusters consisting of 13 atoms show the best performance in CO adsorption and CO bond breaking compared to all the bimetallic (core-shell arrangement) nanoclusters. An initial predictor that can be used to anticipate potentially effective catalysts was identified as a percentage difference, based on the difference between the CO adsorption energy and the CO dissociation energy. A greater catalysts performance is expected when that percentage difference is maximized. The percentage differences calculated for the ruthenium (46%) and Co (38%) clusters confirm these findings.

Results obtained on pure systems for the first step in the Fischer Tropsch reaction mechanism (adsorption of CO onto the catalyst surface) indicate that not only the nature of the support but the crystallographic plane of the surface of the support that is exposed to the catalyst nanoparticle have an effect on the energy barrier for this reaction to take

place. Nanoclusters on support such as silica and rutile with different miller planes were studied with the GGA functional with plane wave basis sets. Co and ruthenium clusters on rutile <110> plane were found to have increased performance with percentage differences of 50% and 60% respectively. Our results indicate that CO adsorbs more strongly on a hollow site of Ru cluster supported on the <110>-terminated rutile support than in any other investigated case. For CO adsorption on supported Co nanoparticles, the silica support is preferred rather than the rutile. The <100>-terminated silica support works best with Co cluster for CO adsorption, followed by the <111>, and finally <110>-terminated silica support. The percentage difference calculated on supported single metal systems shows that the order of preference (best to worst) of potential catalyst seems to be: Ru/rutile <110>, Co/rutile <110>, Ru/rutile <100>, and Fe/rutile <100>.

APPROVAL FOR SCHOLARLY DISSEMINATION

The author grants to the Prescott Memorial Library of Louisiana Tech University the right to reproduce, by appropriate methods, upon request, any or all portions of this . It is understood that "proper request" consists of the agreement, on the part of the requesting party, that said reproduction is for his personal use and that subsequent reproduction will not occur without the written approval of the author of this . Further, any portions of the used in books, papers, and other works must be appropriately referenced to this .

Finally, the author of this reserves the right to publish freely, in the literature, at any time, any or all portions of this .

Author _____

Date _____

DEDICATION

This dissertation is dedicated to my beloved parents, Govinda Prasad Gyawali (father) and Rama Regmi Gyawali (mother), to my brother; Sumit Gyawali, to my wife; Jwala Parajuli Gyawali; and to all my family, friends, and my advisors that have made the completion of this dissertation possible.

TABLE OF CONTENTS

LIST OF FIGURES

LIST OF TABLES

ACKNOWLEDGMENTS

I would like to thank Dr. Daniela Mainardi for allowing me to be a part of her research group at Louisiana Tech University. I am greatly indebted for all her support and guidance at every step of the research program. I would also like to acknowledge financial support from the National Science Foundation (NSF) under the following grant: EPSCoR LA-SiGMA project under award # EPS-1003897.

I express my profound gratitude to Dr. Ramu Ramachandran, member of my advising committee, for always being there for everything that I have needed. Your compassion has helped me to become a confident person.

My sincere thank you to Dr. Collin Wick, member of my advising committee, for always having his door open whenever I had confusions and clearing out my doubts about my computational approach.

Thank you, Dr. Pedro Derosa, and Dr. Shengnain Wang for the courses they taught which helped me to develop my interest in computational material science and engineering research.

I would also like to thank my wife, Jwala Parajuli Gyawali, for always being there with motivation and support and helping me to be a better person.

Thank you very much, my father, Govinda Prasad Gyawali; my mother, Rama Regmi Gyawali; my brother, Sumit Gyawali; and my colleagues, Dr. Pratik KC, Dr. Suvhashis Thapa, and Sumegha Godara, for all the support and encouragement during all these years at Louisiana Tech University.

CHAPTER 1

INTRODUCTION

1.1 Background

Fischer Tropsch synthesis (FTS) is a catalytic chemical process that converts a mixture of carbon monoxide and hydrogen into liquid hydrocarbons (high-quality transportation fuel) [1-8]. Fischer Tropsch (FT) reaction process is based on the chemical reaction given in **Eq. 1-1.**

$$\mathrm{nCO} + (2\mathrm{n}+1)H_2 \rightarrow C_n H_{2n+2} + H_2O \qquad \textbf{Eq. 1-1}$$

where n=number of molecules

This process dates back to 1902 when Sabatier and Senderens synthesized hydrocarbons from CO and H_2 (Syngas) [2]. Later, in 1922, aliphatic oxygenated compounds were produced from the mixture of carbon monoxide and hydrogen by Hans Fischer and Franz Tropsch, and this synthesis process is named after them. The feedstock for this process is gas, and the products are synthetic lubrication oil and synthetic fuel. This process requires the presence of a catalyst, typically iron (Fe), cobalt (Co), ruthenium (Ru), or nickel (Ni) [3]. The use of Ru as catalyst yields highly pure fuel and oil. With its use, synthesis of the highest molecular weight of hydrocarbon (poly-methylene) has been reported [4]. Ru acts as a pure metal FTS catalyst without any promoters. However, Ru is an expensive and rare element. Due to this limitation, the industrial process of making fuel with Ru is more expensive

than the present-day cost of producing crude oil. Another material used as the catalysts is Ni, which yields methane as a byproduct. Methane is extremely flammable, an air pollutant, and may form explosive mixtures with air [5]. Therefore, due to the drawbacks of Ni and Ru, Fe and Co are preferred as the safer and easily available alternative catalysts for the Fischer Tropsch reaction. Fe is found in abundance in nature. The use of Fe as the active Fischer Tropsch catalyst is a cheaper means of producing fuels because of its low price. However, with the use of Fe based catalysts, the process leads to excessive methane formation as a byproduct, lowering the formation of olefinic products [6-7] . Therefore, Fe based catalyst needs alkali promoters for higher activity and selectivity towards linear alkane fuels. The alkalized Fe based catalysts exhibit water gas shift activity due to which, the activity of the catalysts decreases through product inhibition by water. This feature leads to the restrictions of the attainable degree of conversion [7]. Therefore, identifying the optimal FT catalyst continues to be an open problem.

Fischer Tropsch process is mainly operated under two modes known as high-temperature process and low-temperatures process [8]. In the high temperature process, the temperature ranges between 573 K and 623 K. This high temperature process is mainly carried out in a fluidized bed reactor, and Fe is used as catalysts. The feeding ratio of H_2/CO is normally less than 2 and the operation is carried out in around 20-40 bars of pressure. Hydrocarbon ranging from C1-C15 is yielded in this process with other valuable chemicals such as α-olefins and oxygenates. On the other hand, both the Co and Fe catalysts can be used in the low temperature process. The major yield of this process is C1-C100 linear paraffin. The operating temperature in this mode is between 473 and 513

K. This process is mainly carried out in a fixed bed or slurry reactor with the pressure of 20-45 bars [9].

The Fischer Tropsch process has always been a topic of interest because Fischer Tropsch produced fuels are free of sulfur, contains almost no aromatic compounds, and the Fischer Tropsch fuels have low emissions during internal combustion in the engines [10].

1.2 Reaction Mechanism

As indicated in **Eq. 1-1**, Fischer Tropsch (FT) is a surface catalyzed polymerization reaction that synthesizes hydrocarbons by hydrogenation of carbon monoxide in the presence of hydrogen. During the reaction, carbon monoxide is first adsorbed on the surface of the catalyst and is hydrogenated to produce CH_x monomers. Then these CH_x monomers propagate to form a wide product range of long chain hydrocarbons. The catalysts play an important role in the product selectivity since the products can vary from olefins, paraffin, and/or alcohol. The complex chemistry of FTS is not fully understood, despite being an established industrial technology since 1926 [2]. Moreover, it is a process of complex reactions involving many surface intermediates and reaction steps [3]. Hydrocarbon formation proceeds in the following sequence: chain initiator generation; chain growth or propagation and chain growth termination or desorption [4]. Central to the FT mechanism is the identity of the chain initiator. Despite the experimental and theoretical work, several mechanistic details for the FT reaction remain unclear and unpredictable. For example, the CO dissociation pathways remain largely unresolved [6-9]. Thus, FT reactions require detailed atomistic studies of the hydrocarbon formation sequence. For a given chemical reaction, the reactant conditions

and sources (i.e. natural gas, coal, and biomass) are relevant. However, in the FT synthesis, the reaction kinetics is highly dependent on the catalyst. Hence, appropriate catalysts reduce costly investments in the production of syngas. Typically, high–surface–area supports (i.e. silica, alumina, or zeolites) [2] are used as support for these catalysts. Consequently, the ability to control or engineer the catalyst surface provides leverage for controlling reaction pathways and product distribution. Indeed, catalysis already plays a key role in the continuing development of clean energy conversion processes [10], particularly, for the conversion of syngas to clean fuels using FT [11]. In order to implement the FT synthesis process at a large–scale, two fundamental issues need to be addressed: i) Identification of atomic sites for CO adsorption (i.e. stepped surfaces, nanocluster surfaces) on the surface of the catalyst to initiate the catalytic reactions ii) Identification of intermediate species and identification of preferred reaction pathways, given the choice of catalysts for this process. There are many reaction mechanisms proposed for the FT chemical reaction, but the most widely accepted mechanism are surface carbide mechanism and surface enol mechanism [12-13].

1.2.1 Surface Carbide Mechanism

CO adsorption is the key step in any kind of proposed FT reaction mechanism. In this proposed mechanism CO adsorbs and dissociates to form carbide and surface oxygen species. In Figure 1-1, we can see that in the reaction mechanism of Fischer Tropsch, CO and Hydrogen adsorption is the key step to begin with the chemical reaction process according to this mechanism. This is shown in the yellow box in this Figure. To the left of the yellow box in Figure 1-1 is the surface carbide mechanism, where CO dissociates to form C* (* means adsorbed on the catalyst surface) and O*. Then the adsorbed

hydrogen reacts with the C* and O* to form CH* monomer and OH* group. More hydrogen comes and reacts with this CH* and OH* to form CH_2^* and water molecules (H_2O). Possible chain initiators, methylene (CH_2) groups, are generated via hydrogenation of carbide species [12], and this polymerizes to form long chain hydrocarbons.

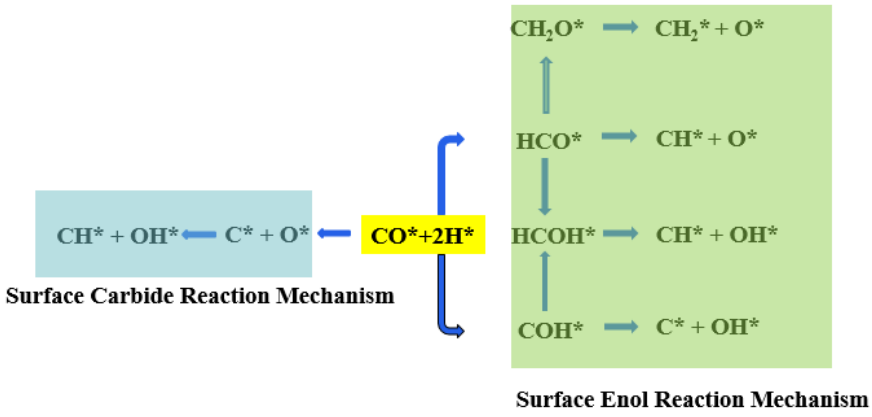

Figure 1-1: Commonly accepted Fischer Tropsch reaction mechanisms

1.2.2 Surface Enol Mechanism

In Figure 1-1, the right side of the yellow box is the surface enol mechanism. After the adsorption of CO and H_2 on the surface of the catalyst surface (yellow box), the CO* does not dissociate; instead, H* comes to react with CO* to form formyl species HCO* or COH*. At this stage, the CHO* or HCO* species may dissociate to form C* and OH* or CH* and O*, respectively on the surface of the catalysts or the CHO* or HCO* may further react with H* to form enolic species HCOH* or CH_2O*. Now the HCOH* will break down into CH* and OH* and CH_2O* will break down into CH_2* and O*. Thus the separation of O from the CO* with the assistance of H* leads to the formation of the first monomer CH* or CH_2*, and they further polymerize to form long chained hydrocarbons [11].

1.3 Related Research

Considerable work is being done seeking an alternative to fossil fuels from sources such as solar, wind, and biomass, in order to meet future global energy needs as well as to ensure environmental protection [13]. CO_2 emissions from fossil fuels is an important factor in global warming.

Research has shown that the chemical reaction mechanisms in the FT process are highly sensitive to catalyst structure. Therefore, there are several studies done on modified surfaces such as kinked and stepped surfaces to predict whether the reactions are more favorable on flat or modified surfaces [14-15]. The reaction kinetics of the FTS on the surface of the catalysts can be further enhanced by addition of promoters or can be affected by the support [16]. Studies have shown that Co catalysts can be promoted with the use of the oxides such as ZrO_2, La_2O_3, CeO_2, and MnO_2 which would modify the porosity and the texture of the catalysts. These oxide promoters also help to reduce the formation of hardly reducible Co mixed oxides [17]. Potassium and copper are very popular promoters used for Fe catalysts for FTS [16]. Promoters facilitate the reduction of the catalysts, improve the selectivity, help to retain a high metal surface area, and improve the mechanical properties which are very important for the smooth stability of the catalysts. Similarly, there are extensive research work being done in bimetallic catalysts [18]. Kintaichi *et al.* reported that the bimetallic catalysts which contained a pair of metals from group VIII have an impact on the selectivity [19]. According to their study, bimetallic catalysts made from Ir and Ru on silica support have highest CO conversion, low methanol selectivity, and higher alcohol selectivity. These studies are

important scientifically because it aids in the optimal design of the catalysts for any kind of catalytic reaction.

Therefore, the catalyst is the heart of the FT Synthesis. The first priority that should be given in the FT Synthesis is the design an FT active catalyst with higher activity to the desired product selection and longer life with less catalyst deactivation.

1.4 Goals and Objectives of this Work

Researches have shown that the FT reaction is a structure sensitive reaction process. The selectivity of the process also depends on the surface of the catalysts due to which pure and bimetallic nanocluster catalysts have gained a lot of attention [18-19]. The high surface to volume ratio of the nanoclusters provides more active sites for CO adsorption: therefore, favoring the FT reaction process. Also, the nanoclusters exhibit different properties such as lower coordination of surface atoms and higher electron affinity than their bulk counterparts and the properties the properties can be manipulated by alloying them in order to enhance the catalytic activity of the nanoclusters [17].

According to surface carbide mechanism, the CO adsorption is followed by CO bond breaking on the surface of the catalyst and is the rate determining steps. It is also obvious that in order to hydrogenate carbon, the oxygen atom has to detach from CO on the surface of the catalysts. Therefore, the goal of this research is to identify the potential nanocluster catalyst (Co, Fe, Ru, and Ni) for FT applications based on the CO adsorption and its bond breaking on their surfaces.

Hypothesis: *CO adsorption and dissociation energy on a catalysts surface can be used to predict the effectiveness of a material as catalysts for FT applications.*

CHAPTER 2

THEORY AND SIMULATION DETAILS

This chapter outlines the theoretical basis of Density Functional Theory (DFT) which is an electronic structure calculation method employed in this work to calculate properties such as energies, structure, and thermo-chemistry. Two different software packages were used in this work:

- DMoL3; which is a module of the Biovia Materials Studio suite [20].
- Vienna Ab Initio Simulations Package (VASP) [21–23].

The DFT theory levels employed in each case are detailed in this chapter.

2.1 Background

It is a well-established fact that quantum mechanics is a fundamental theory to calculate different properties of a system comprised of electrons and atomic nuclei [24]. The system could be a single atom or the assemblies of atoms because quantum mechanics describes and explains chemical bonds. By solving the Schrödinger equation for the electrons and the nuclei, the fundamental properties of any system can be understood [25]. But solving the Schrödinger equation for many body systems, which means a system of two or more electrons, is computationally more expensive as the number of the electrons in the system increases. The full, time dependent form of the Schrödinger equation is given by **Eq. 2-1.**

$$\left(-\frac{\hbar^2}{2m}\nabla^2 + \Upsilon\right)\Psi(r,R,t) = i\hbar\frac{\partial\Psi(r,R,t)}{\partial t} \qquad \textbf{Eq. 2-1}$$

where $\nabla^2 = \frac{\partial^2}{\partial x^2} + \frac{\partial^2}{\partial y^2} + \frac{\partial^2}{\partial z^2}$,

$\hbar$ = Plank's constant divided by 2π,

m = mass of the electron moving through the space,

Υ = external field such as electrostatic potential,

E = energy,

I = an imaginary unit,

$\Psi(r, R, t)$ = wave function which characterizes the particle motion.

When the external potential is independent of time, the time-independent Schrödinger equation can be written as:

$$\left(-\frac{\hbar^2}{2m}\nabla^2 + \Upsilon\right)\Psi(r,R) = E\Psi(r,R) \qquad \textbf{Eq. 2-2}$$

The simplest way to write the time-independent Schrödinger equation is:

$$H\Psi(r,R) = E\Psi(r,R) \qquad \textbf{Eq. 2-3}$$

where $H = \left(-\frac{\hbar^2}{2m}\nabla^2 + \Upsilon\right)$ = Hamiltonian operator,

r and R=positions of the electron and nuclei respectively,

H = nuclear kinetic energy, electronic kinetic energy, nuclear-nuclear repulsion, electron-electron repulsion, and electron-nuclear attraction.

Eq. 2-3 is a partial differential eigenvalue equation in which an operator acts on a function to return the same function but multiplied by a scalar value. The wavefunction for a system of two and more electrons is expressed in the form of a Slater determinant to satisfy Pauli's principle [24]. Schrödinger equation for poly-electronic atoms and molecules is not easy to solve because it is a function of too many variables. Hence, in

order to solve the Schrödinger equation for a molecular system, an assumption was made and proposed by Max Born and Robert Oppenheimer in 1927 which became very popular in chemical physics known as Born-Oppenheimer Approximation [26]. In the Born-Oppenheimer approximation, the electronic motions and the nuclei motions are separable due to the fact that the nuclei are much heavier than the electron; hence, the motion of the nuclei is much slower than the motion of the electron. Therefore, the molecular wavefunction for the Schrödinger equation at a fixed nuclear position (R_a) that can be separated into its electronic components and nuclear components as described by **Eq. 2-4** and gave birth to the electronic wavefunction equation.

$$\Psi(r, R_a) = \Psi_{el}(r) * \Psi_{nu}(R_a) \qquad \textbf{Eq. 2-4}$$

The electronic Schrödinger equation for a given set of nuclear positions is calculated by ignoring the motion of the nuclei and can be represented as:

$$H_{el}\Psi_{el}(r, R) = E\,\Psi_{el}(r, R) \qquad \textbf{Eq. 2-5}$$

where H_{el} represents H as in **Eq. 2-2** but omits the nuclear kinetic energy.

Different computational methods were developed to solve **Eq 2-5** for the electronic wave function, such as semiempirical, Hartree-Fock, and various post-Hartree-Fock methods.

2.2 Introduction to DFT

Density functional theory is a method to obtain the electronic ground state structure of atoms and molecules based on the electron density distribution $\rho(r)$ as opposed to the many-electron wave function $\Psi(r1, r2, r3, \ldots)$ [24]. In 1964, Hohenberg and Kohn came up with a break through, showing that there is a one-to-one relationship between the ground state electronic energy and electron density [27]. Many of the

properties of a system such as the ground-state energy can be defined through the electron density. Later, in 1965, Kohn-Sham [28] came up with an approach to calculate the total ground state energy based on electronic density. The Kohn-Sham equation is given as:

$$E = T_s + V_{ne} + \frac{1}{2} * \iint \frac{\rho(r1)\rho(r2)}{|r1-r2|} * d^3r1\ d^3r2\ +\ E_x + E_c \qquad \textbf{Eq. 2-6}$$

where *Ts* = non-interacting kinetic energy of the electrons,

V_{ne} = interaction of electron with external potential,

$V_{ee} = \iint \frac{\rho(r1)\rho(r2)}{|r1-r2|} * d^3r1\ d^3r2$ = columbic repulsion between two electrons,

E_x and E_c = exchange and correlation functions.

Density Functional Theory [29] is the method that has been applied in this research for the computation of the structures and energies of the different molecules. Unlike semiempirical and Hartee-Fock methods, DFT includes the computation of electron correlation which is denoted as E_c in the **Eq. 2-6**. The Density Functional Theory computes the ground state total energy and the spin densities of the molecules based on quantities such as T_s, V_{ne}, E_x, E_c and V_{ee} as mentioned in the above **Eq. 2-6**. DFT method has become very popular for the last three decades among theoretical and computational chemists, and it has been used in the study of the electronic structure of many body systems, in particular atoms, molecules, and condensed phases [30].

2.2.1 Potential Energy Surface

All the quantum chemistry methods such as DFT, Hartree-Fock, and other semi-empirical methods are used to calculate the energy of a molecule for solving the electronic energy for a fixed set of nuclear positions. Movement in the nuclei positions of a system lead to change in the electronic configuration thus changing the energy of the

system. In the absence of external fields, the potential energy of a molecule does not change if it is translated or rotated in space. Hence, the potential energy of a system only depends on its internal coordinates (*x*, *y*, *z*) for each atom, minus three translation and three rotation. Potential energy surface (PES) is defined as the set of points representing the geometries and the corresponding energies in a 3N-6 (N= number of atoms) dimensional space. Change in the nuclear positions bring a change in bond length, bond angles, dihedrals, and energy of a molecular system [31].

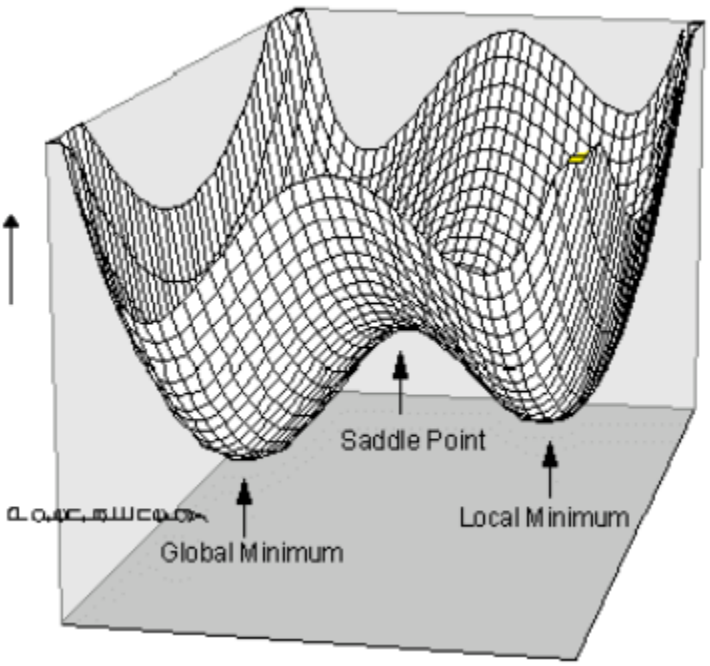

Figure 2-1: Schematic representation of a Potential Energy Surface of a molecule consisting of 3 atoms. Note: the dimension for the Potential Energy Surface is 3N-6, where N = number of atoms

The potential energy surface shown in Figure 2-1 has two cusps and are labeled as global minimum and local minimum. The ground state structure lies on these cusps and is minima of PES. At these cusps, the first derivative of the energy is zero and the second derivative of the energy is positive with respect to the coordinates of the system. In order

to move from one minimum to another minimum, the system has to come over the barrier called saddle points as in Figure 2-1. Saddle points are the points on the PES where the first derivative of the energy is zero and the second derivative is negative.

2.2.2 Exchange and Correlation Functional

One of the key reasons for the success of the density functional approach is the exchange and correlation functions. The total energy for the density functional theory is described in **Eq. 2-6**. In the equation E_x and E_c are the exchange and correlation energies which include all many-body contributions to the total energy [32]. All the functions in **Eq. 2-6** can be calculated exactly except for the exchange and correlation functional. If the exact exchange and correlation functional were known, then the DFT theory would yield exact results.

There are various approaches to approximating the XC (exchange and correlation) functionals such as the local density approximations (LDA), generalized gradient approximations (GGA), meta-GGA, and hybrid methods. Since the XC energy in LDA at point **r** only depends on the local electron density, it can be written as [29]:

$$E_{xc}(\rho) = \int (\rho(r) e_{xc}(\rho\uparrow(r), \rho\downarrow(r)))d^3r \qquad \textbf{Eq. 2-7}$$

where e_{xc} = exchange and correlation function

$\rho\uparrow(r)$ and $\rho\downarrow(r)$ = spin densities,

$\rho(r) = \rho\uparrow(r) + \rho\downarrow(r)$.

For an infinite uniform electron gas, LDA functionals are exact but most of the real systems have inhomogeneous density distributions and LDA functional yield approximate results [33]. Some of the inaccuracies of LDA are an overestimation of the binding energy as compared with the corresponding experimental ones. In LDA, the

typical errors in bond energies are about 30 kcal/mol [34]. In order to improve LDA, GGA was introduced which has information about the electron density like LDA, but it also includes the gradient of the electron density ($\nabla\rho(r)$). This can be called as a straight forward approach to improve LDA as GGA accounts for inhomogeneity in the density. GGA can be represented as [29]:

$$E_{xc}(\rho) = \int \rho(r) e_{xc}(\rho\uparrow(r), \nabla\rho\downarrow(r), \nabla\rho\uparrow(r), \rho\downarrow(r)) d^3r \quad \textbf{Eq. 2-8}$$

2.2.3 Basis sets

Basis sets are the set of mathematical functions used to approximate the orbitals within a system which in turn combine to approximate the total electronic wavefunction [35]. One of the methods to describe molecular orbitals (MO) is to combine the atomic orbitals (AO). An atomic orbital describes an electron in an atom while a molecular orbital describes an electron in a molecule. One way to express MOs is to use the linear combination of AOs (LCAO) as:

$$\Phi i(r) = \sum_a C_i^a \chi_a(r) \qquad \textbf{Eq. 2-9}$$

where χ_a =atomic orbital,

Φi = molecular orbitals,

C = coefficient to be determined.

In order to represent the atomic orbitals, two types of functions are commonly used: Gaussian-type orbitals (GTO) and Slater-type orbitals (STO). The mathematical representation of the GTO and STO are given as:

$$\chi^{GTO} = N x^l y^m z^n e^{-ar^2} \qquad \textbf{Eq. 2-10}$$

$$\chi^{STO} = N r^{n-l} e^{-ar} Y_{lm}(\theta, \varphi) \qquad \textbf{Eq. 2-11}$$

where N = normalization factor,

α = exponent,

(x,y,z) = Cartesian coordinates,

(r, Θ, φ) = spherical coordinates,

l and m = angular momentum,

Y_{lm} = spherical harmonic.

From the above equations, the major difference between GTO and STO is the dependence in the exponential function. The quadratic dependence of GTO on the exponential function makes it computationally cheaper than STO, although STOs represent a much better wave function in the proximity of the nuclei. On the other hand, a linear combination of the GTOs gives approximations almost as accurate as to the STOs. The set of functions, Gaussian or Slater, which describes the atomic orbitals and later can be combined to form molecular orbitals is called basis sets. Some examples are the Minimal basis sets, Double-Zeta (DZ) basis sets, Triple-Zeta (TZ) basis sets, and Split-Valence (SV) basis sets. In minimal basis sets, a single basis function is used to describe each orbital on each free atom [36]. Double-Zeta and Triple-Zeta basis sets use two basis functions and three basis functions for each atomic orbitals respectively [37]. Split-Valence basis sets use two STOs for each valence atomic orbitals and only one for inner core atomic orbitals [37]. Similarly, Polarization basis functions add polarization functions in order to give additional flexibility to describe molecular orbitals more accurately. For example, adding *p*-functions to *s* orbitals of lighter atoms such as hydrogen or adding *d*-type functions to atoms with valence *p* orbitals [37]. Likewise, another common function added to the basis sets is the diffuse functions (s,p_x,p_y,p_z) on

hydrogen and heavy atoms; which improves the accuracy of the basis sets and is termed as Diffuse basis functions [38].

In addition to these basis sets available in quantum chemistry packages, there are other types that exist e.g. plane waves [39], wavelets [40], and numerical basis sets [41-42]. In this work, two types of basis sets have been used, which are numerical basis sets implemented in DMoL3 and plane wave basis sets which are employed in the Vienna Ab initio Simulation Package (VASP).

Numeric basis sets can also be represented by **Eq. 2-9**, but in this case, the mathematical expression for the atomic orbital is different from those of GTO and STO. In numeric atom centered basis functions, the atomic orbital can be represented as

$$\chi^{NAO} = \frac{u(r)}{r} Y_{lm}(\Omega) \qquad \textbf{Eq. 2-12}$$

where *u(r)* = radial function,

$Y_{lm}(\Omega)$ = complex spherical harmonics [42].

The radial portion of the function, *u(r)*, is obtained by solving the DFT equation numerically. Atomic basis sets are confined within a cutoff value, r_c, which leads to much faster calculations. The major advantage of the numeric atom centered basis sets over localized atom centered basis sets like GTO and STO is the almost elimination of basis set superposition error (BSSE) which is caused by overlapping of basis functions.

On the other hand, plane wave basis sets are the ideal basis functions for the periodic system. The plane wave method is based on Bloch's theorem. With the use of the Bloch's theorem, it is possible to describe the wavefunction of an infinitely long crystal system in terms of wavefunctions at reciprocal space vector of a Bravais lattice [43]. From the above statement, it can be deduced that the properties of an infinite long

crystal system can be calculated just by calculating the wavefunctions from the number of electrons in the unit cell of the crystal. With the use of the Bloch's theorem, the wavefunction of an electron in a periodic system can be written as:

$$\Psi_{i_k}(r) = exp(ikr)u_{i_k}(r) \qquad \textbf{Eq. 2-13}$$

where Ψ_{i_k} = wavefunction of an electron within the periodic potential,

exp (ikr) = wavelike part,

u_{ik} has the periodicity for the lattice,

k is in the first Brillouin zone (BZ).

Further, the periodic lattice can be represented as:

$$u_{i_k}(r) = \sum_G C_i\,(G)\exp(iGr) \qquad \textbf{Eq. 2-14}$$

where C_i = coefficient of expansion,

G = reciprocal lattice vector.

Thus, **Eq. 2-13** and **Eq. 2-14** can be combined to form a linear combination of plane waves.

2.2.4 Pseudopotentials

Pseudopotentials are the method of calculating the effective potential for the electrons and its nucleus in an atom [43–45]. In a pseudopotential approach, the electrons in a system can be divided into valence and core electrons. Core electrons are the electrons in the inner closed shell which are close and tightly bound to the nuclei. On the contrary, valence electrons are far from their nucleus and are the ones that form bonds, get ionized, conduct electricity, and perform all other atomic activities.

In terms of the wavefunctions, the wavefunctions of the valence electrons are orthogonal to core electrons wavefunctions and oscillates rapidly. This kind of

wavefunctions has many nodes and are not easy to express. Basis sets with no pseudopotential consider all the electrons that are present in a molecular system or solid, and this can be computationally expensive. In the pseudopotential approach, the core electrons are frozen and represented by the pseudopotential thus reducing the computational effort. Therefore, the main requirement of the pseudopotentials approach is to reproduce the same valence charge densities as reproduced by all-electron methods in order to predict chemical bonds and other properties by replacing the core electrons potential by an effective electron potential.

There are different ways to treat the core electrons using DMol3 and VASP. DMol3 offers Density functional Semi-core Pseudopotentials (DSPP), Effective core potentials (ECP), and all-electron schemes, while VASP offers Norm-conserving pseudopotentials, Ultrasoft pseudopotentials, and Projected Augmented wave methods. The use of pseudopotentials will be discussed in the respective chapters.

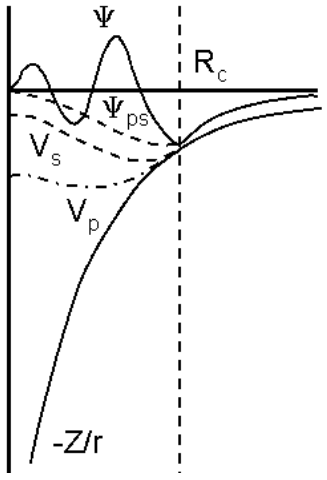

Figure 2-2: Schematic representation of the all-electron and pseudo wavefunctions and potentials where R_c is the cut-off radius, Ψ is all electron-wavefunction, Ψ_{ps} is pseudo-wavefunction, V_p is the Coulomb potential pseudo potential, and V_s is the pseudo potential [45]

Hamman *et al.* have shown that the pseudo and all electron wavefunctions behave identically beyond the core radius as shown in the Figure 2-2.

2.2.5 Transition State Theory

During a chemical reaction, starting with the reactants, the potential energy increases to a maximum and then decreases to the energy of the products. The maximum energy along the reaction pathway is called the transition state energy or saddle point energy and the structure associated with this is called transition state structure [46]. Reactants and products are the local minima points on the molecular potential energy surface. After performing the geometry optimizations, minima corresponding to the reactant and the product on this potential energy surface are located. The reactants must overcome this saddle point on the potential energy surface in order to form products. The structure linked to the maximum on the potential energy surface is called transition state structure. With the energy value of the reactant and saddle point, the barrier energy can be calculated. The barrier energy is the energy needed by the reactants to overcome the saddle point on the potential energy surface for the reaction to proceed [46].

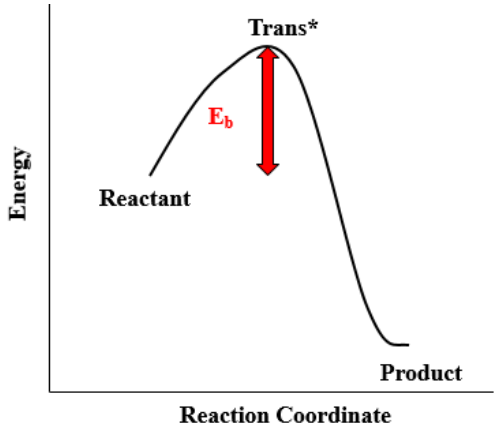

Figure 2-3: One-dimensional potential energy surface of the reactant, transition state (Trans*), and the product as well as the associated energy barrier (E_b) over the reaction coordinate

After finding the ground state structure of the reactant and the product, the transition state structure is linked by interpolating the atomic coordinates of the reactant configuration to the product configuration by following the minimum energy path (MEP) on the PES. This MEP also gives detailed information of all the intermediate configurations along the reaction coordinates. There are various methods for calculating the MEP, such as the drag method, nudged elastic band (NEB) method, and estimate of the tangent methods [47]. In this work, the synchronous transit method is used which is employed in DMol3 for the DMol3 calculations, and for all the VASP calculations, the NEB method is used.

2.2.6 Synchronous Transit Methods

Synchronous transit methods are used to find the transition state when the ground state structure of the reactants and the products are known. During the process, the reaction pathway is interpolated from an existing ground state structure of the reactants and the products. The Linear Synchronous Transit (LST) method first uses linear interpolation between the reactants and the products to find the maximum in the potential energy surface. Further refinement is performed using the Quadratic Synchronous Transit method (QST) which performs conjugate gradient minimization to find the maximum energy [48]. After finding the transition state, the geometry optimization of the structure is carried out using the eigenvector following method. The eigenvector following method uses the Newton-Raphson methods for the minimization along the potential energy surface. Instead of searching for the minimum energy, it searches for the maximum energy by calculating the Hessian matrix along with one normal mode. This ensures the

most accurate transition state structure for a particular reaction is obtained [49]. The Hessian matrix is calculated using frequency or vibrational analysis. This method is implemented in DMol3 and for the DMol3 transition state calculations, the LST/QST technique is used to generate the minimum energy path for a given reaction.

2.2.7 Nudged Elastic Band Method

In this method string of images are created to describe the MEP unlike in LST/QST, which creates a trajectory path along the MEP. These images are the intermediate images, which are created based on the ground state structures of the reactant and the product. Equal spacing between the images along the reaction pathway is ensured by the spring forces. Spring force interactions between the adjacent images also ensure the continuity of the path, thus producing an elastic band. The force projection scheme is used for relaxing the images to the MEP which involves minimization of the forces acting on the images [50]. In order to ensure that the nudged elastic band passes through the saddle point, the component of the restoring force that is normal to the reaction path is removed. In such case, the motion perpendicular to the reaction path is guided by the gradient of the potential energy surface and gradient of the spring guides motion parallel to the path [50-51]. Hence, a tangent to the path at each image and every iteration during the minimization is estimated in order to decompose the true force and the spring force into parallel and perpendicular components along the path [52]. The NEB method gives a discrete representation of the MEP, and the energy of the saddle points are obtained by interpolation.

2.3 Procedure to Calculate Energetics

In order to screen the effectiveness of the catalysts for the Fischer Tropsch reaction, parameters such as CO adsorption and CO bond breaking has been studied using DFT. The CO adsorption energies, E_{ads} (CO) were calculated using **Eq. 2-15**. According to this equation, negative binding energy corresponds to a stable CO adsorption onto the cluster surface.

$$E_{ads}\,(CO) = E(CO*) - E\,(catalyst) - E\,(CO) \qquad \textbf{Eq. 2-15}$$

where $E(CO*)$ = energy of the cluster with 1 CO molecule adsorbed on its surface,

E(cluster) = energy of the catalyst,

$E(CO)$ = energy of a single CO molecule.

In order to calculate the CO breaking energy, energetically stable ground state structure of fully CO cleaved species (product) on the surface of the catalyst is required. After finding the most stable CO bound on the active site of the cluster, preferred adsorption sites (PAS) on the catalyst, the structure was taken as a reference structure to construct the product. The O atom was cleaved from the surface of the catalysts and put 3 Å away from the C atom. Next, the minimization of the structure was performed to find the ground state structure of the product. To determine the transition state structure and the energy associated with it, the LST/QST technique was performed using DMoL3, and the NEB method was performed for the VASP runs. After locating the transition state and the energy associated with it, the CO bond breaking energy (E_{diss}) is calculated using the following equation:

$$E_{diss}(CO*) = E(Trans)* - E(CO*) \qquad \textbf{Eq. 2-16}$$

where $E(Trans)^*$ = energy of the transition state,

E(CO)* = energy of the reactant species.

Eq. 2-15 was used to calculate E_{ads} (CO) for isolated catalysts (models with no support). In chapter six and seven, silica and rutile are used to study the interaction of the support with the catalyst models. The calculation of E_{ads} (CO) when the catalyst support is present is given by **Eq. 2-17:**

$$E_{ads}\,(CO) = E(CO*) - E\,(catalyst/support) - E\,(CO) \qquad \textbf{Eq. 2-17}$$

where $E(CO*)$ = energy of the support catalyst with 1 CO molecule adsorbed on its surface,

E(catalyst/support) = energy of the catalyst with support,

$E(CO)$ = energy of a single CO molecule.

Based on the CO adsorption energies and CO breaking energies, a percentage difference is calculated using **Eq. 2-18**. This percentage difference is defined as an indicator of catalyst performance.

$$\%Diff = \frac{[|E_{ads}(CO)| - E_{diss}(CO)]}{Average[|E_{ads}(CO)|, E_{diss}(CO)]} * 100 \qquad \textbf{Eq. 2-18}$$

Dissociation energy is always required to be smaller than the absolute value of the CO adsorption energy. This helps to facilitate the bond breaking of CO on the surface of the catalysts. If the energy for breaking the CO bond on the surface of the catalysts is greater than the absolute value of the CO adsorption energy, the CO molecule desorbs from the surface of the catalysts instead. Negative adsorption energy calculated using DFT in this chapter ensures that the CO is chemisorbed on the surface of the catalyst, and the catalysts are suitable for any kind of heterogeneous chemical reactions that involves synthetic gas and begins with CO adsorption.

CHAPTER 3

RESULT I – PURE AND BINARY 14 ATOMS COBALT AND IRON CATALYST MODELS

3.1 Pure and Alloyed Co-Fe Catalysts Models

Since cobalt and iron are the catalysts mainly used for commercial purposes, we first investigated pure and binary combinations of these metals as catalysts for FT reactions. The pure metal models are made up of 14 atoms of corresponding pristine elements arranged in non-periodic face-centered cubic structures. A face-centered cubic structure is selected because, in a face-centered cubic structure, there is one atom on each face of the cube, thus six atoms from six faces and one atom on each corner of the cube, thus eight total atoms from all corners of the cube as shown in Figure 3-1. Hence, summing up all the atoms gives a nanocluster of 14 atoms in a non-periodic representation.

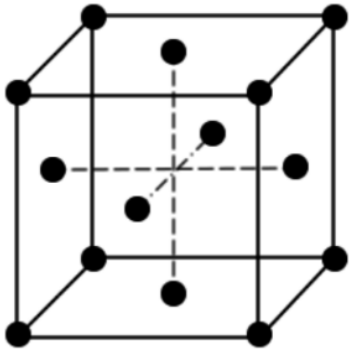

Figure 3-1: Face-centered cubic structure

At first, pure nanoclusters of Co and Fe were created, and geometry optimization was performed to find the ground state of the structures. Then the pure Co cluster was alloyed with Fe atom in increasing fashion to build bimetallic nanoclusters with different concentrations of Fe. After finding the ground state structures of the pure and bimetallic nanoclusters, only the stable structures were chosen based on the cohesive energy of the nanoclusters for further study (CO adsorption and breaking). The computational details of this study are explained in the next section.

3.2 Computational Details

The Generalized Gradient Approximation (GGA) method within the Density Functional Theory (DFT) formalism, as implemented in the DMOL3 module of the BIOVIA Materials Studio 6.0 software [53], was used in this work. Using GGA method such as the Revised Perdew- Burke-Ernzerhof (RPBE) [54], the calculation of molecular geometries and cluster structures, ground state energies, adsorption energies of molecules, cohesive energies of solids, and the energy barriers for molecular reactions are performed with great accuracy. In particular, GGA is typically found to be superior for the description of the energetic of atomic and molecular bonding than LDA.

In this work, geometry optimization calculations were performed using the double numerical with polarization (DNP), all-electron basis set. The DNP basis set considers a polarization *d* function on heavy atoms and a polarization *p* function on hydrogen atoms. DNP basis set can be compared to the split-valence double zeta 6–31G** in size; however, DNP basis sets are more accurate than the Gaussian basis sets of the same size [55]. The convergence criterion for the force parameter on the atoms was 0.004 Ha/Å and for the energy was $2x10^{-5}$ Ha during the geometry optimization. The geometrical and electronic

structures are calculated with the all-electron method with the real space cut off of 4.5 Å. Harmonic vibrational frequency calculations were performed to ensure that stationary points on the potential energy surface of the molecular systems were, in fact, local minima (all real frequencies) or transition states (only one imaginary frequency). Spin multiplicity states were also checked, and zero-point energy corrections are considered in all calculations. The energies obtained for the different minima were compared, and only the ground state conformations were considered for further calculations.

The Cohesive energies of pure and bimetallic nanoclusters were determined by **Eq. 3-1:**

$$E_{coh}(A_nB_m) = \frac{[E\,(Co_nFe_m) - nE(Co) - mE(Fe)]}{N} \qquad \textbf{Eq. 3-1}$$

where $E(A_nB_m)$ = energy of the A_nB_m binary core(A)-shell(B) clusters (A, B: Co, Fe) containing $N = n + m$ total number of atoms,

$E(Co)$ and $E(Fe)$ = energies of the pure elements *Co* and *Fe* per atom respectively,

n and m = total numbers of atoms of *Co* and *Fe* type in a Co_nFe_m cluster respectively.

Thus, for instance, the Co_2Fe_{12} notation will be used when referring to a cluster containing 2 Co atoms in the core and 12 Fe atoms in the surrounding shell.

3.3 Nanoclusters Structural Stability

Fischer-Tropsch reaction is a catalytic surface polymerization reaction, and the selectivity of products also depends on the catalyst stability and its active sites. Therefore there has been intensive research done in studying the FT reactions by modifying the surface of the catalyst, either by doping catalysts with different kinds of promoters or by

investigating the effect of the catalysts particle size in the reaction [56–57]. Thus, the bimetallic catalyst of transition metals also has high potential as an FTcatalyst.

Nanoclusters always exhibit unique geometrical structures, physical and chemical properties. The properties of the nanoclusters depend on the size and composition, hence a suitably designed nanocluster promises tailored properties and are helpful in the synthesis of the materials [58]. The structural stability of bimetallic nanoclusters based on Co and Fe were studied based on cohesive energy. The results obtained from the 14 atom nanoclusters are presented in this section.

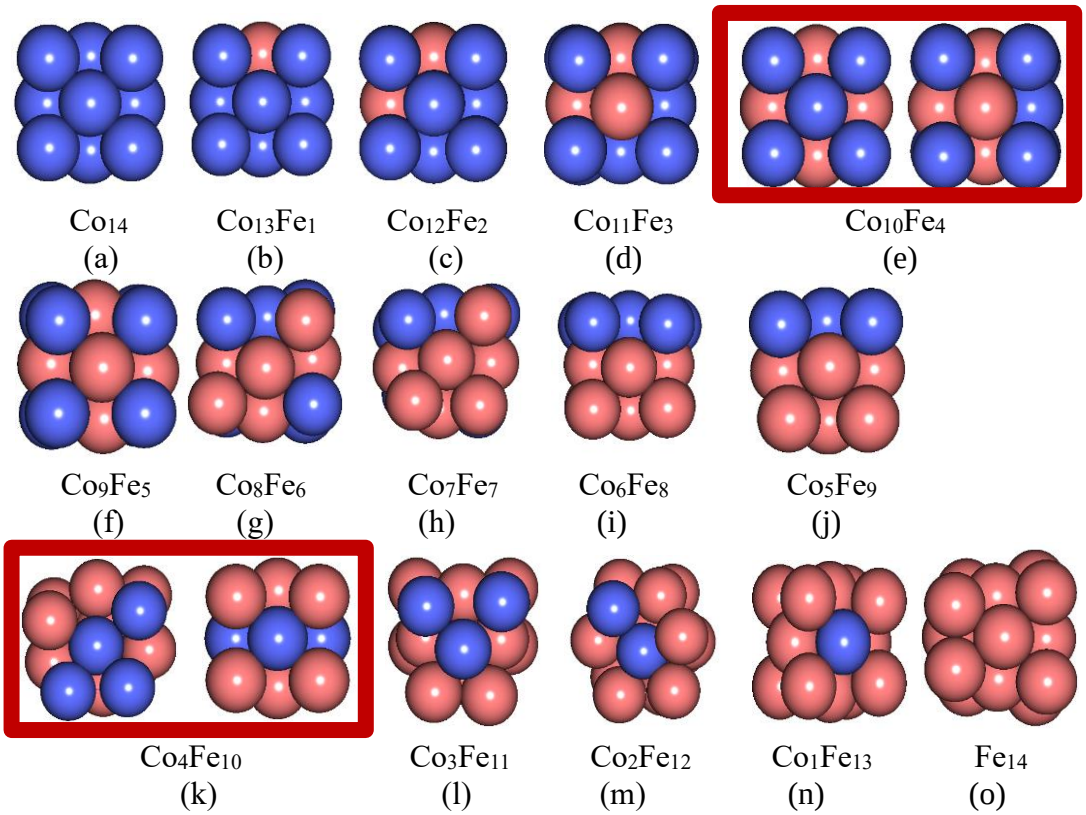

Figure 3-2: Pure and bimetallic nanoclusters of Co and Fe, Co_nFe_m where n, m = 0, 1, 2,… 14 (Blue: Co, Pink: Fe)

In Figure 3-2, the structures of pure and bimetallic nanoclusters of Co and Fe are shown. After finding the ground state structure of the pure Co cluster (Figure 3-2 (a)), an

atom from the pure Co cluster was replaced by a Fe atom. Similarly, at every following structure, increasing numbers of Co atoms were replaced by Fe atoms until the pure Fe nanocluster was obtained. All the structures were subjected to geometry optimization to find the corresponding energetically stable ground state structures. For $Co_{10}Fe_4$ and $Fe_4Co_{10,}$ two different configurations have been investigated. In Figure 3-2, these structures are outlined with red borders. Figure 3-2 (e) shows two isomers of a $Co_{10}Fe_4$ cluster. One of the isomers consisted of four Fe atoms that substitutes a Co atom randomly in the cluster, while on the other structure, four Fe atoms were sandwiched between two layers of five Co atoms each. Similarly, Figure 3-2 (k) shows an isomer of $Fe_{10}Co_4$ cluster. In the cluster, one of structures had Fe atoms randomly substituting Co atoms, while the other structure consisted of four Co atoms sandwiched between two layers of five Fe atoms each. Sandwiched structures can be represented as core-shell models and are a subject of interest for this study. These sandwiched structures with ten Co atoms and four Fe atoms ($Co_{10}Fe_4$) will be represented as CoFe, and with ten Fe atoms and four Co atoms ($Fe_{10}Co_4$) will be represented as FeCo in this study.

There are abundant low-lying structural isomers of all the bimetallic clusters whose ground state energies could be very close to each other. This can be examined through performing geometry optimization of all the isomers of each bimetallic cluster which need running frequency analysis on each structure to ensure ground state structures are found. This is beyond the scope of this work, but frequency analysis was done to each bimetallic cluster used in this study to confirm that these nanoclusters are the local ground state structures. Dmol3 computes the vibrational properties based on the finite-difference method. The vibrational spectra are plotted in Figure 3-3. In the figure, it can

be clearly seen that all the bimetallic clusters do not exhibit any imaginary frequency. This assures that the structure lies in the local minima cusp of the potential energy surface and is ground state structures.

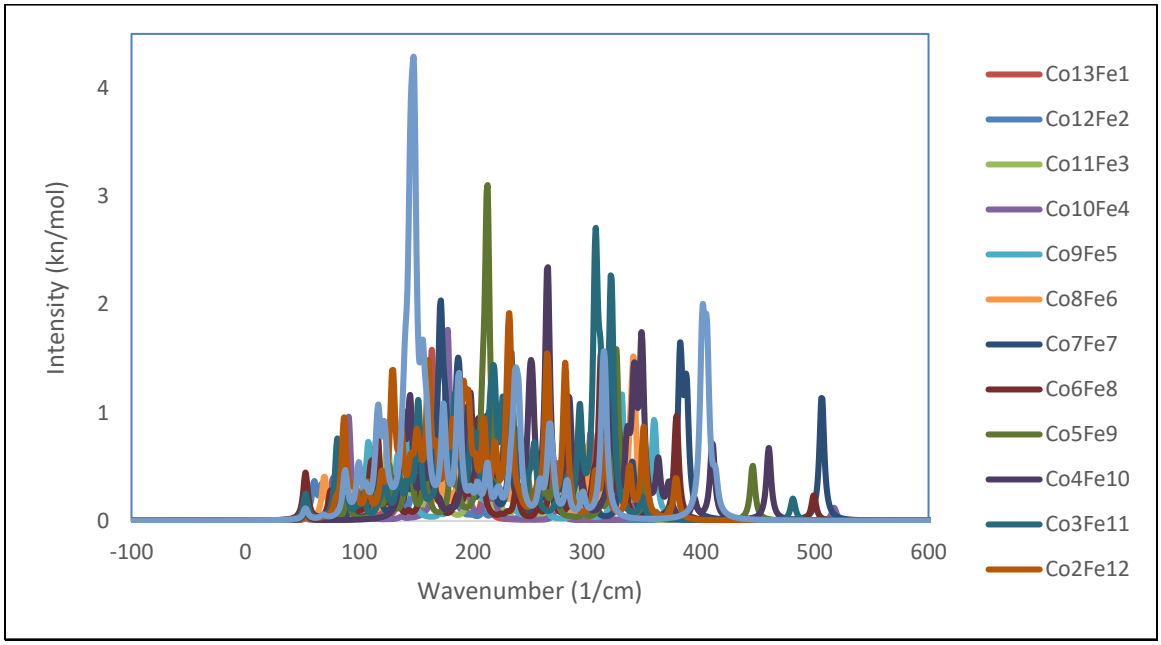

Figure 3-3: Frequency analysis of bimetallic clusters. The IR spectra do not have any peaks at the negative numbers and confirms the ground state geometry

3.3.1 Cohesive Energy of Bimetallic Cluster

The cohesive energies of the bimetallic clusters were computed using **Eq. 3-1**. According to this equation, the energies of the bimetallic clusters are computed in reference to the pure Co cluster and the pure Fe cluster. Negative cohesive energies in this equation indicate that the structures are more energetically favorable than the pure clusters and hence they can be designated as stable bimetallic clusters. The cohesive energies of the bimetallic clusters are shown in Figure 3-4.

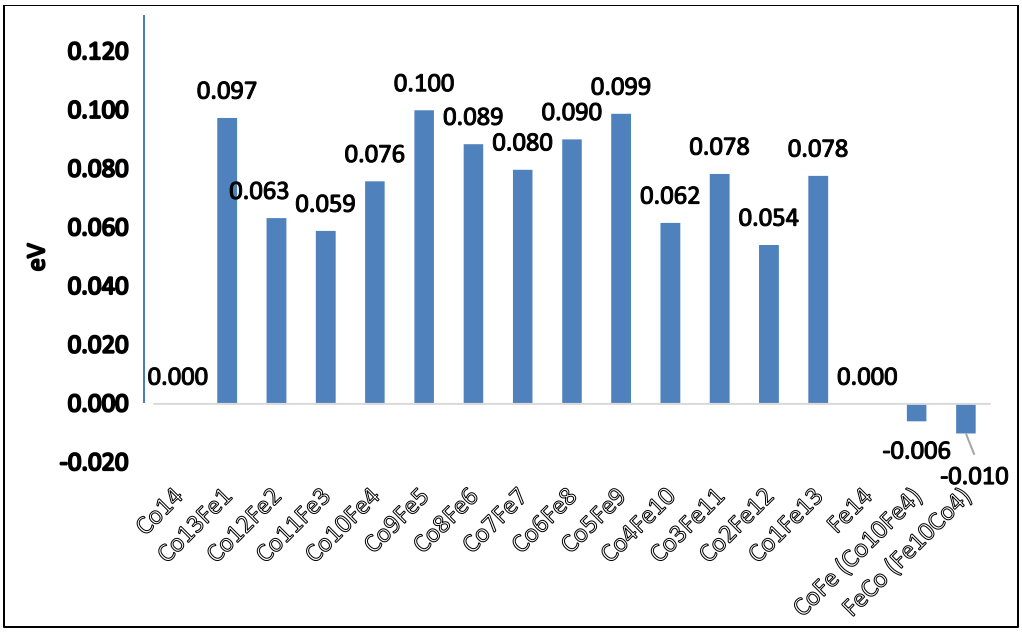

Figure 3-4: Cohesive energies of bimetallic clusters

In Figure 3-4, we can see that the pure clusters, which are represented as Co_{14} for Co cluster and Fe_{14} for the Fe cluster, do not show any cohesive energies. This is because the energies of these pure clusters are the baseline for comparing the energies of the bimetallic clusters. On the other hand, the cohesive energies for all the bimetallic clusters are positively valued except for CoFe and FeCo systems. All these positive cohesive energies of the bimetallic clusters convey the information that the clusters are not energetically favorable when compared to the energies of the pure clusters. Thus, it can be deduced that only CoFe and FeCo systems are energetically favorable when compared to pure clusters. The cohesive energy of CoFe and FeCo systems are lower by -0.006 eV and -0.010 eV respectively than those of pure clusters. Hence, these two clusters including pure clusters were selected based on the stability test to study the CO adsorption and its bond breaking on their surface, which is presented and discussed in the next section.

3.4 CO Adsorption and Its Bond Breaking

3.4.1 CO Adsorption

CO adsorption was calculated on pure Co, Fe, CoFe, and FeCo clusters using **Eq. 3-2**. Different CO adsorption sites were investigated which includes top, bridge, and hollow sites for each case. The adsorption sites for the pure cluster are shown in Figure 3-5.

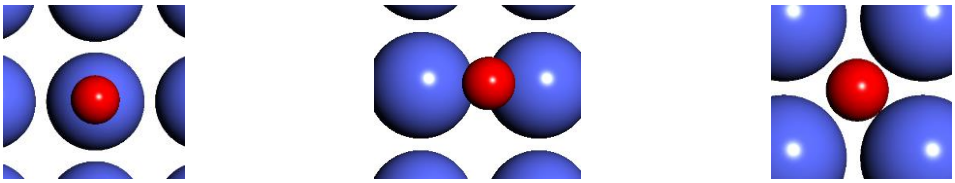

Top Bridge Hollow

Figure 3-5: Different adsorption sites of CO adsorption on pure clusters (Grey: C, Red: O)

When CO is adsorbed directly on top of the metal atom then this is called top adsorption sites. If CO is adsorbed between two metal atoms, then this adsorption is called bridge adsorption, and if CO is adsorbed between three metal atoms, then it is termed as hollow adsorption. In the case of bimetallic clusters, there are at least two top sites, two bridge sites, and two hollows sites, thus bimetallic clusters have more adsorption sites than the pure clusters. All the possible active sites of the bimetallic cluster are shown in Figure 3-6.

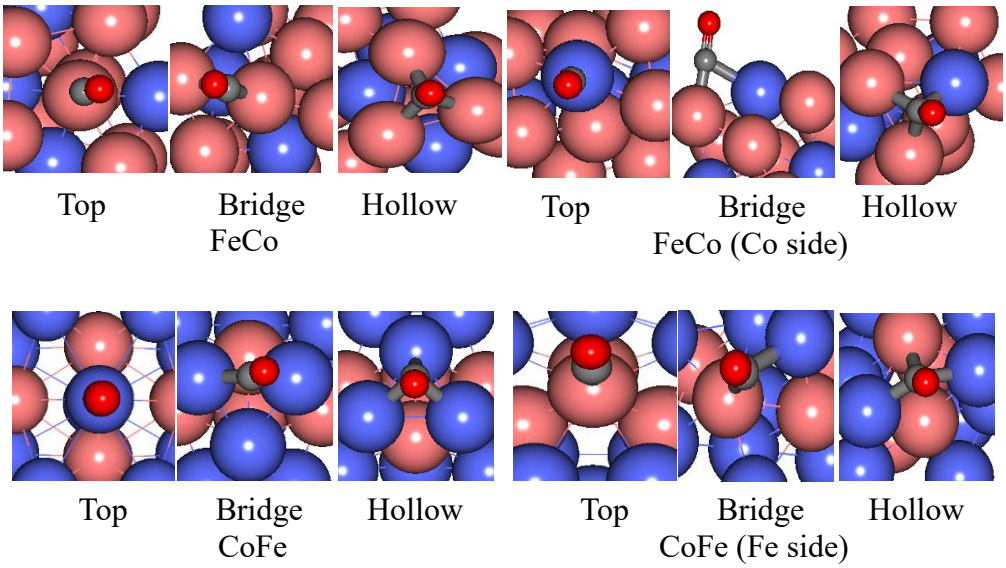

Figure 3-6: Different adsorption sites for bimetallic CoFe and FeCo clusters

The adsorption energies (E_{ads}) of CO on all the possible sites in pure nanoclusters and the energies for breaking the CO bond on the surface of the cluster is presented in Table 3-1. The adsorption of CO on the top, bridge, and hollow sites of pure Co cluster suggest that the adsorption is favorable on the top site followed by the bridge position and then hollow position. The overall CO adsorption values are higher for the pure Fe cluster than the pure Co cluster.

The adsorption of CO is found to be stronger on the bimetallic clusters than the pure ones. The adsorption is the strongest on the top sites of a Fe atom for the FeCo bimetallic cluster with the adsorption energy of -2.60 eV and on the hollow site of the same system with a CO bound to two Fe atoms and one Co atom with the adsorption energy of -2.72 eV. The adsorption energies of CO are the strongest in the CoFe cluster on all of its adsorption sites compared to all the clusters studied here. In this system, CO strongly adsorbs on the hollow position (CO bound to three Co atoms). This is followed by the adsorption of CO on the top position of a Fe atom. From the study of CO

adsorption, it is observed that the binding of CO with Fe atoms is preferable than the Co atom. Similarly, CO adsorption on the bimetallic clusters also suggests that Fe atom plays an important role during the CO adsorption process.

CoFe system shows strong interaction with CO adsorption along with lower CO dissociation energy compared to Fe, and FeCo clusters. CoFe system has 10 Co atoms at the shell and 4 Fe atoms at the core. Similarly, FeCo system which contains higher concentration of Fe atoms than Co atoms has lower CO dissociation energy compared to pure Fe cluster. Therefore, it can be realized that bimetallic system based on Co and Fe show strong interaction to CO adsorption as well as lower CO dissociation energy when compared with pure Fe cluster. And bimetallic cluster with higher concentration of Co atoms and lower concentration of Fe atoms are preferable.

PAS on the clusters is determined which suggests that the CO adsorption and further reaction is favored on the respective adsorption site. Once the PAS is saturated with the CO molecule, the CO adsorption takes place on the next adsorption site with the minimum adsorption energy. Moreover, the values computed as the CO adsorption energies are chemisorption of CO and strong chemisorption energy also indicates that there is a tendency of forming a long chain hydrocarbon on the surface of the cluster.

Table 3-1: CO adsorption energies (E_{ads}), Adsorptions sites (Top, Bridge, and Hollow), Preferred adsorption site (PAS), and CO bond breaking energies (E_{diss}) on pure nanoclusters and bimetallic nanoclusters

Catalyst	Adsorption sites/ E_{ads} (eV)			PAS	E_{diss} (eV)
	Top	Bridge	Hollow		
Co	**-1.73**	-1.64	-1.36	Top	2.21
Fe	**-2.00**	-1.81	-1.65	Top	3.2
FeCo	**-2.60**	-2.44	-1.85	Top	3.02
(Co side)	-2.35	-2.28	**-2.72**	Hollow	2.78
CoFe	-3.74	-3.8	**-3.81**	Hollow	2.67
(Fe side)	**-3.94**	-3.15	-3.75	Top	2.71

3.4.2 CO Bond Breaking

After finding the CO adsorption energy on the selected nanoclusters, the energy cost for breaking the CO bond on the surface was studied next. CO bond breaking is a reaction step included in Surface Carbide FT mechanism which was already discussed in chapter 1.

CO bond breaking on the surface of the nanoclusters was studied using LST/QST transition state theory as implemented in DMol3. The theory level at which the transition state calculation were performed is already discussed in section 3.2 and all the structures with PAS selected for CO bond breaking study along with transition state structure can be seen in Figure 3-7. The structures for the product and the reactant are the ground state structures ensured by vibrational analysis with no imaginary frequency. Transition state structures are the structures at the energy maxima of the potential energy surface confirmed with one imaginary frequency.

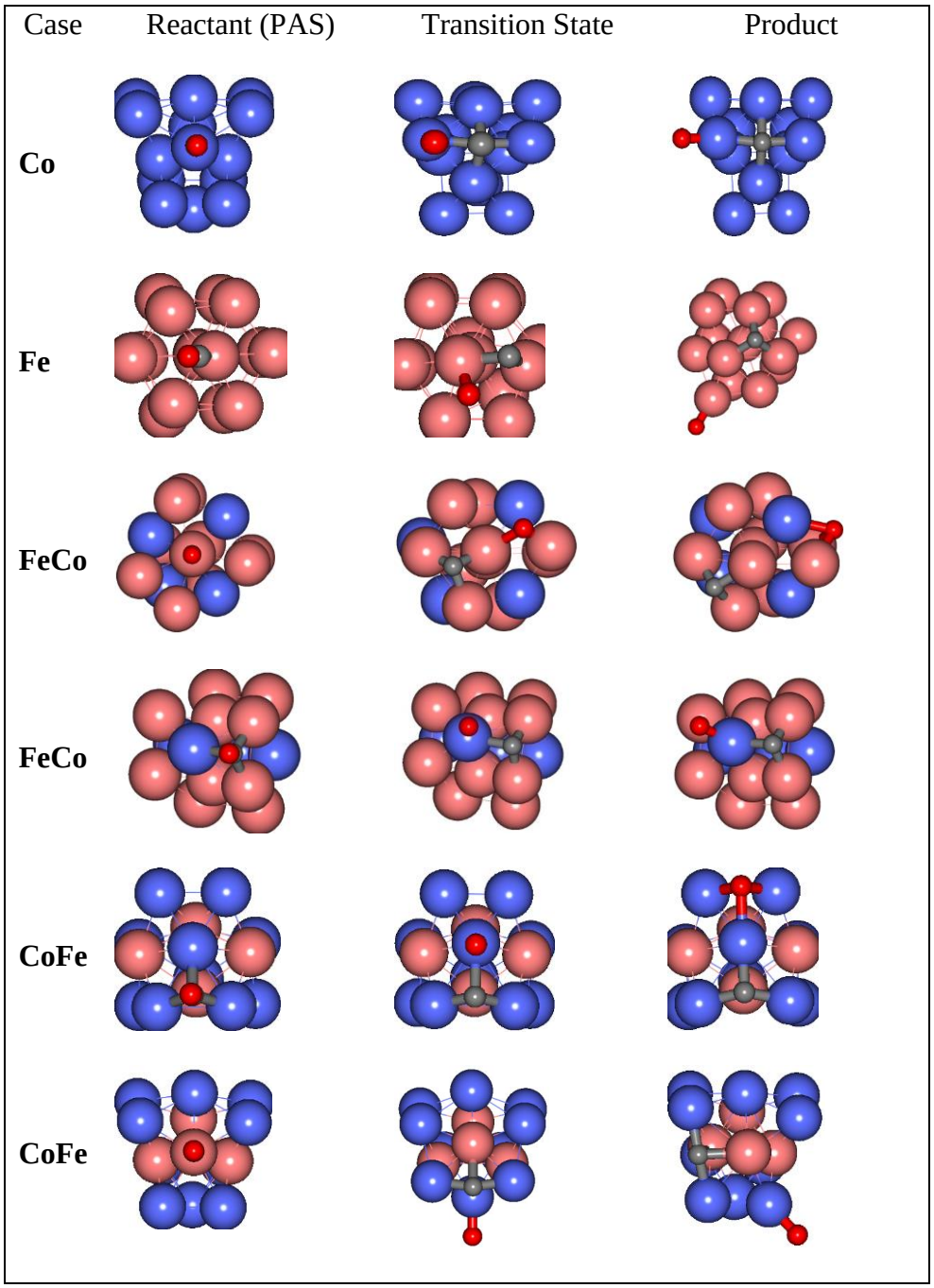

Figure 3-7: CO bond breaking pathway on pure Co_{14}, Fe_{14}, FeCo, and CoFe nanoclusters. The first picture on each set corresponds to the reactant (cluster with CO adsorption on PAS), the middle corresponds to the transition state, and the last picture is the product

Table 3-2 shows the bond length of the adsorbed CO molecule on the PAS, transition state, and fully cleaved CO bond (product) on the surface of the cluster. For instance, the bond length of the CO molecule is 1.18 Å when adsorbed on the top site (PAS) of the pure Co cluster, while during the transition state, the oxygen atom completely detaches from the carbon atom and is 2.07 Å away. The carbon atom forms four bonds with the Co atoms as shown in Figure 3-7 during transition state. The energy calculated to break the CO bond on the surface of the pure Co cluster is 2.21 eV (Table 3-3). At the product state, fully cleaved CO bond on the surface of the cluster, the oxygen atom is 3.36 Å away.

Table 3-2: The bond length of CO when adsorbed to nanoclusters, during the transition state, and at the final product

CO bond length (Å)			
	PAS	Transition state *	Product
Co	1.18	2.07	3.36
Fe	1.18	1.93	5.24
FeCo	1.20	1.78	5.18
(Co side)	1.18	2.13	3.04
CoFe	1.18	2.11	3.82
(Fe side)	1.19	4.52	4.85

Based on the CO adsorption energies and CO dissociation energies, a percentage difference is calculated using the **Eq. 2-17**. The CoFe system showed the best performance with 37% and 35% percentage difference. All the other systems show negative percentage difference such as -24% for the pure Co cluster, -46% for the pure Fe

system, and -15% and -2% for the FeCo system. This indicates that the CO bond breaking is least favorable on these systems.

3.5 Summary

In Table 3-3, we can see that the adsorption of CO on the binary clusters such as FeCo and CoFe systems are much stronger than the pure cases. Our study based on %Diff show that the pure Fe catalyst is the least favorable choice followed by the pure Co catalyst. The binary catalysts have shown an increased performance when compared with the pure cases.

Table 3-3: Summary of the findings, PAS represents preferred adsorption site, E_{ads} is the CO adsorption energy on PAS, E_{diss} is the energy required to break the CO bond, and %Diff is the catalyst performance indicator based on CO adsorption and its bond breaking

System	PAS	E_{ads} (eV)	E_{diss}(eV)	%Diff
Co_{14}	Top	-1.73	2.21	-24
Fe_{14}	Top	-2.00	3.20	-46
FeCo (10:4)	Top	-2.6	3.02	-15
FeCo (10:4)	Hollow	-2.72	2.78	-2
CoFe (10:4)	Hollow	-3.81	2.67	35
CoFe (10:4)	Top	-3.94	2.71	37

CoFe catalyst, which has 4 Fe atoms sandwiched between 10 Co atoms, shows the best performance with the %Diff of 35% and 37% approximately.

CHAPTER 4

RESULT II - MAGIC NUMBER CLUSTERS CO, FE, NI, AND RU CATALYSTS MODELS

Magic number study helps us to identify the clusters with a certain number of atoms that are much more energetically favorable and stable than others. For the closed packed metal nanoclusters, the geometrical magic numbers are generally exhibited by 13, 55, 147, 309, 561, and 923 atoms with a highly symmetrical structure such as icosahedral, octahedral, and decahedral [56–58]. In this chapter, we will discuss the magic number clusters of Co, Fe, Ni, and Ru atoms, which are the most preferred catalysts for the FT process, mainly ranging from 1-20. The second energy difference is calculated to determine the pure structural stability given by the following equation.

$$\Delta E_2 = E(N+1) + E(N-1) - 2E(N) \qquad \textbf{Eq. 4-1}$$

where *E(N), E(N+1), and E(N-1)* = energies of the clusters containing N, N+1, and N-1 atoms respectively,

N = total number of atoms in the cluster.

Cohesive energy (E_{coh}) is calculated as:

$$E_{coh} = N * E(C) - E(N) \qquad \textbf{Eq. 4-2}$$

where *E(N)* = energy of the cluster comprising N number of atoms,

E(C) = energy of a single atom.

4.1 Computational Details

All the calculations to determine magic number clusters for Co, Fe, Ni, and Ru were performed using the generalized gradient approximations (GGA) with the exchange and correlation as defined by revised Perdew-Burke-Ernzerhof (RPBE) functional [54] implemented in DMol3. Spin-polarized calculations were performed with DND basis set (Double numerical $+d$ basis set with no p functions are used on hydrogen) which is comparable to Gaussian 6-31G* basis sets in combination with effective core potentials (ECP). The convergence tolerance of energy is 2×10^{-5} Ha, maximum force is 0.002 Ha/Å, and the maximum displacement was set to 0.005 Å during geometry optimization. Space-group symmetry is used with symmetry turned off during the geometry optimization. Using space group symmetry helps to detect the symmetry by transforming the coordinates of the molecule automatically to the most energetically favorable orientation.

4.1.1 Cobalt Cluster

Geometry optimization at the above-mentioned theory level was performed on a Co cluster containing 1 through 19 atoms. The second energy and the cohesive energy plot are shown in Figure 4-1.

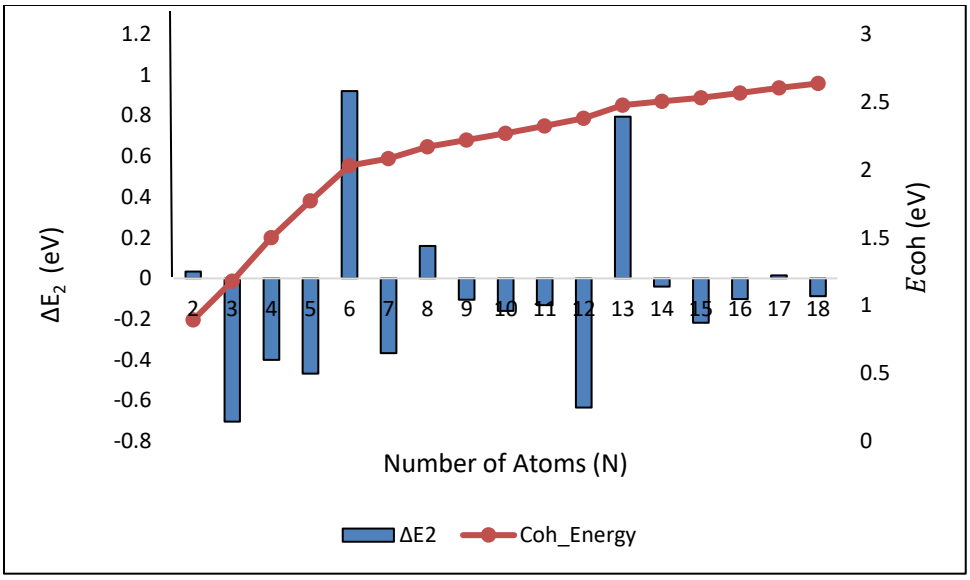

Figure 4-1: Stability test of pure Co cluster (Co_N, N = 1-19 atoms) showing second energy difference (ΔE_2) and cohesive energy (E_{coh}) results

According to Figure 4-1, the second energy difference shows a strong peak at 6 and 13 for the Co cluster with the cohesive energy of 2.45 eV. Therefore, it can be assured that Co clusters containing 6 and 13 atoms are more stable clusters than their neighboring clusters.

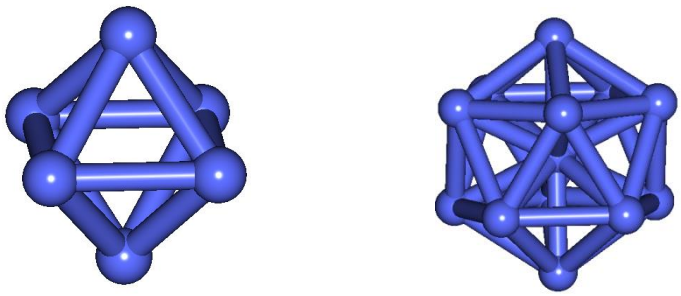

Figure 4-2: The geometric structures of the most energetically stable Co clusters with 6 atoms and 13 atoms respectively

The most stable configuration of Co_6 is found to be tetragonal bipyramid and for Co_{13} is distorted icosahedral which can be seen in Figure 4-2. For 13 atoms cluster, the

other possible isomers could be decahedral, cub-octahedral, and regular icosahedral structures. The initial configuration of the Co_{13} cluster was regular icosahedral, which changed to the distorted icosahedral structure during the group symmetrical geometry optimization.

4.1.2 Iron Cluster

Fe clusters ranging from 3 to 21 were optimized for the magic number cluster generation at the same theory level as mentioned above. The second energy difference graph and the cohesive energy for the Fe cluster are shown in Figure 4-3. A strong peak is seen at 13 atoms Fe cluster for the cohesive energy as well as the second energy difference. Cohesive energy for 13 atoms Fe cluster is 3.52 eV per atom which is the strongest among all the cohesive energies for each cluster.

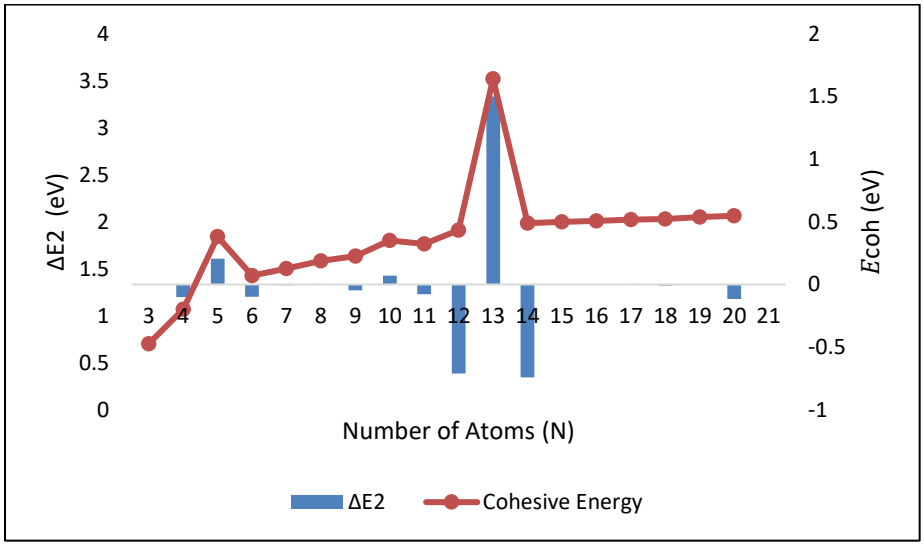

Figure 4-3: Stability test of the pure Fe cluster (Fe_N, N = 3-21 atoms) showing second energy difference (ΔE_2) and cohesive energy (E_{coh}) results

One more peak is seen for the second energy graph with the total number of 5 atoms, but this peak is small compared to the peak for the 13 atoms cluster. The cohesive energy for the 5 atoms cluster is 1.84 eV which is even higher than the cohesive energies obtained up to 11 atoms cluster. Therefore, two structures one with 5 atoms and the other with 13 atoms are considered the most stable clusters for Fe_n with $n < 20$. The theoretical calculations of Fe_5 found that the most stable ground state structure to be trigonal bi-pyramid with D_{3h} symmetry. On the other hand, the theoretical calculation for the Fe cluster with 13 atoms predicts distorted icosahedral structure as the most stable structure same as for the Co cluster with 13 atoms (Figure 4-4).

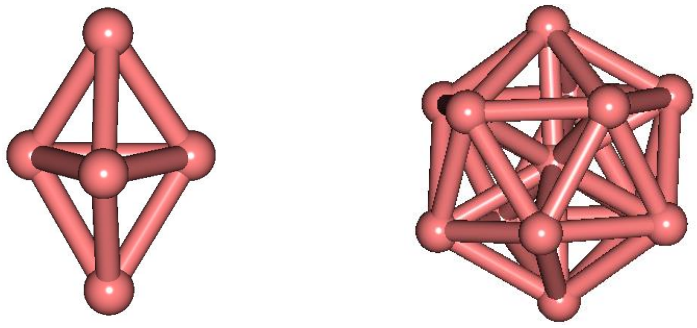

Figure 4-4: The geometric structures of the most energetically stable Fe clusters with 5 atoms and 13 atoms respectively

4.1.3 Nickel Cluster

The second energy difference and cohesive energy studies were performed to determine the most stable structures among all the neighboring clusters which consist of Ni atoms. Figure 4-5 shows the second energy graph and the cohesive energies in eV for Ni clusters ranging from 2 to 25.

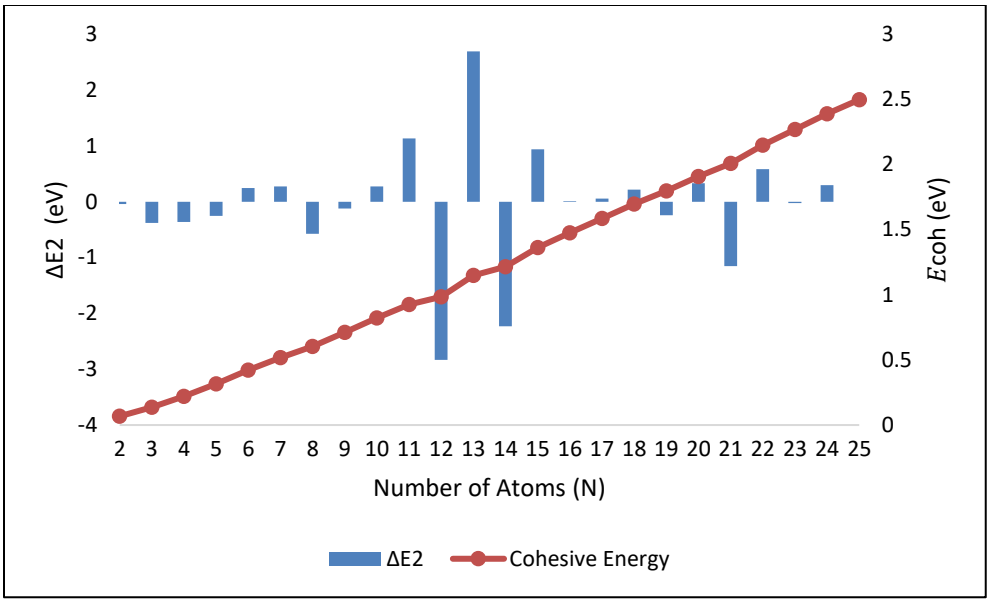

Figure 4-5: Stability test of pure Ni cluster (Ni_N, N = 2-25 atoms) showing second energy difference (ΔE_2) and cohesive energy (E_{coh}) results

According to the second energy graph, the most stable structures for Ni clusters are the clusters which consist of 11 atoms, 13 atoms, 15 atoms, 20 atoms, and 22 atoms. Although the cohesive energy is larger for the clusters containing 22 atoms, the peak obtained for this cluster from the second energy difference is weaker compared to the clusters containing 11 atoms, 13 atoms, and 15 atoms.

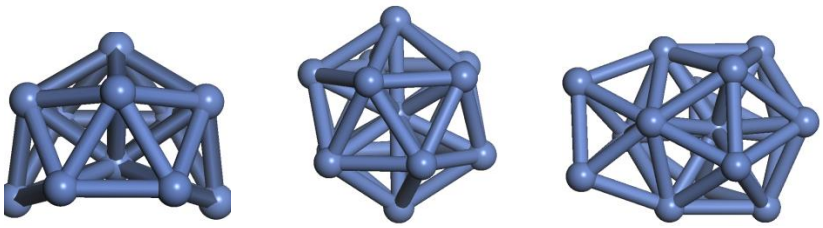

Figure 4-6: The geometric structures of the most energetically stable Ni clusters with 11 atoms (left), 13 atoms (center), and 15 atoms (right) respectively

4.1.4 Ruthenium Cluster

The structural stability test was performed for the Ru clusters that range from 1 through 21. Ru cluster with 13 atoms shows a strong peak with the maximum cohesive energy of 4.25 eV. This cohesive energy value for this cluster is the largest energy among all the cohesive energies of Ru clusters studied. According to the second energy difference calculation, other clusters such as Ru_5, Ru_7, Ru_9, and Ru_{16} also show weak peak which is illustrated in Figure 4-5. If characterized according to the intensity, then a Ru cluster with 5 atoms follows the most stable structure after the 13 atoms cluster followed by Ru_9, Ru_{16}, and Ru_7 respectively.

Ru cluster with 13 atoms and 5 atoms will be considered the most stable and energetically favored structures in this study. For Ru_n ($n < 20$), Figure 4-8 shows that Ru cluster with 5 atoms exhibits square pyramid as the most stable structure and with 13 atoms distorted icosahedral structure is predicted as the most stable structure.

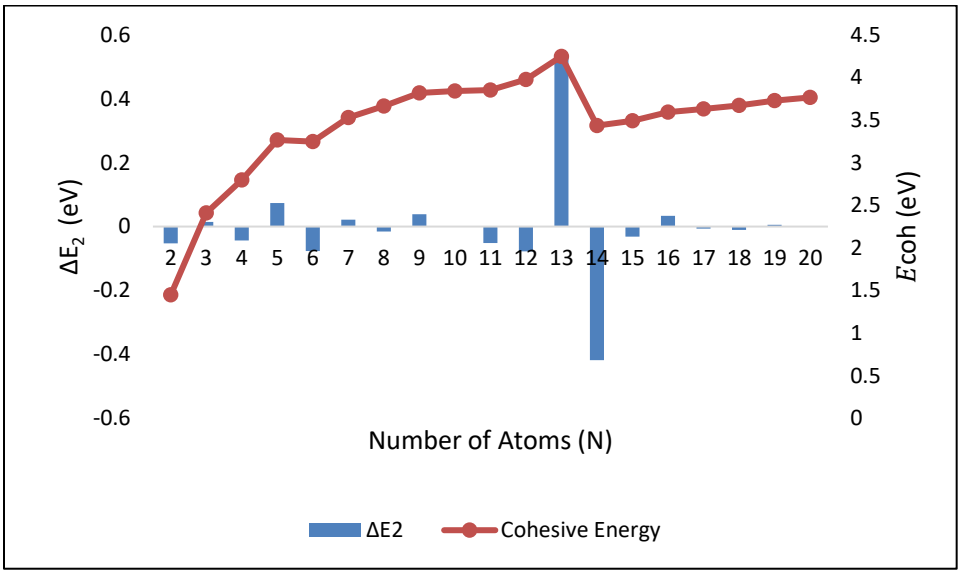

Figure 4-7: Stability test of pure Ru cluster (Ru_N, N = 1-21 atoms) showing second energy difference (ΔE_2) and cohesive energy (E_{coh}) results

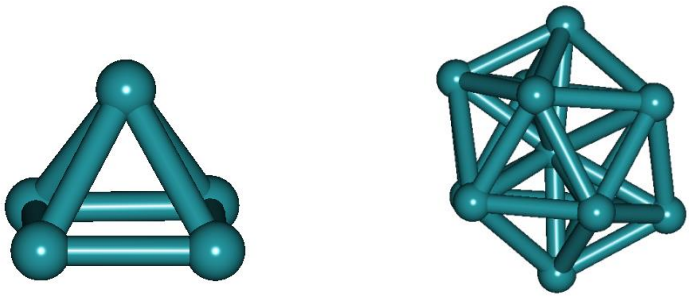

Figure 4-8: The geometric structures of the most energetically stable Ru clusters with 5 atoms and 13 atoms respectively

In summary, energetically and geometrically stable structures were obtained for Co, Fe, Ni, and Ru clusters with the atomic number (N) ranging from 1 to 21. Clusters with the common number of atoms (13) was found the most stable structures with distorted icosahedral symmetry. Based on the structural stability, 13 atoms cluster with an icosahedral structure will be chosen for the further study of CO adsorption and it's bond breaking. Because of the low coordinated atomic sites than other low-symmetry isomers, metal clusters with icosahedral symmetry are also expected to have special catalytic properties [56].

4.2 CO Adsorption and Its Bond Breaking

CO adsorption and its bond breaking is studied on the most stable structures of Co, Fe, Ni, and Ru clusters predicted from cohesive energies and second energy difference. Input structures for the 13 atoms clusters are taken from section 4.1, and the theory level at which geometry optimization is performed is explained in chapter 3 in section 3.2. Transition state theory has been implemented as described in chapter 3 in section 3.3. The energy cost to break the CO bond on the clusters is calculated using **Eq 2-16.**

4.2.1 CO Adsorption

CO adsorption on different adsorption sites such as top, bridge, and hollow was studied. Top, bridge and hollow sites are displayed in Figure 3-5 for the pure cases and **Eq. 2-15** is used to calculate the adsorption of CO on 13 atoms clusters with icosahedral symmetry. The values for the adsorption energies and the values for energies required to break CO bond length on the surface of the clusters are presented in Table 4-1.

Table 4-1: CO adsorption (eV) on different sites of 13 atoms clusters

Catalyst	Adsorption sites/ E_{ads} (eV)			PAS	E_{diss} (eV)
	Top	Bridge	Hollow		
Co	-1.64	-1.58	**-1.65**	Hollow	1.12
Fe	**-1.49**	-1.41	-1.49	Top	2.29
Ru	**-2.68**	-1.84	-1.77	Top	1.35
Ni	**-1.77**	-1.67	-1.74	Top	2.47

In Table 4-2, the different adsorption sites along with CO and metal-carbon (M-C) bond length are reported. The atomic index (numerical representation of the atoms onto which CO is adsorbed) numbers in the table can be seen in Figure 4-9. For instance, CO binds with a Co atom of atomic index 5 of the Co nanocluster when CO is adsorbed on the top site. The bond distance of CO when adsorbed on the top site is 1.18 Å and the bond distance of M-C {C-Co (5)} is 1.80 Å. When CO is adsorbed on the bridge sites, the CO binds with two Co atoms, Co (5) and Co (11). At the bridge configuration, the bond length of CO is 1.20 Å and the bond distances of C-M, C-Co (5) and C-Co (11), are 1.95 Å and 1.94 Å respectively. The bond distance of CO on the hollow configuration is 1.22 Å, and the bond distance of C-Co (9) is 2.20 Å, C-Co (5) is 2.03 Å, and C-Co (11) is

2.01 Å. 13 atom clusters of Co, Fe, Ni, and Ru with icosahedron symmetry are shown in Figure 4-9.

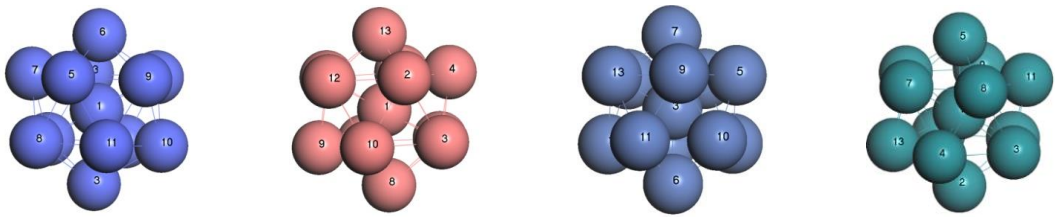

Figure 4-9: 13 atoms clusters with icosahedron symmetry with atomic index numbers for Co, Fe, Ni, and Ru respectively

Table 4-2: 13 atoms pure clusters of cobalt (Co), iron (Fe), ruthenium (Ru), and nickel (Ni), their atomic index number, CO bond length in Å when adsorbed on the different adsorption sites of the clusters, and metal-carbon (M-C) bond length in Å

Clusters	Sites	Index	CO (Å)	M-C (Å)
Co	Top	5	1.18	1.8
	Bridge	5, 11	1.20	1.95/ 1.94
	Hollow	9, 5, 11	1.22	2.20/ 2.03/ 2.01
Fe	Top	13	1.19	1.83
	Bridge	10, 2	1.20	1.98/ 1.98
	Hollow	13, 4, 7	1.23	2.04/ 2.04/ 2.03
Ru	Top	5	1.19	1.9
	Bridge	5, 9	1.20	2.00/ 2.14
	Hollow	5, 9, 6	1.21	2.16/ 2.17/ 2.17
Ni	Top	7	1.17	1.77
	Bridge	5, 7	1.20	1.91/ 1.90
	Hollow	4, 7, 5	1.21	1.98/ 1.97/ 1.98

From the study of CO adsorption on different adsorption sites on the clusters, it can be deduced that these clusters show potential for the heterogeneous catalytic reaction that involves CO adsorption as an initial reaction step. For FT catalysts, the ideal catalyst

follows surface carbide mechanism that could break CO without letting CO molecule to desorb from the surface. Therefore, low value for CO adsorption and low value for CO dissociation energies are preferred. In Table 4-1, Ru cluster shows strong interaction with the CO adsorption followed by Ni, Fe, and Co clusters. On the other hand, Co cluster shows lower barrier for CO dissociation followed by Ru, Fe, and Ni clusters. More information can be deduced by studying the percentage difference calculation which is mentioned in later section.

Similarly, M-C bond length and C-O bond length in Table 4-2 indicates that the carbon atom does not diffuse into the clusters during the CO adsorption process and the bond length of CO molecule is stretched when compared to the bond length of CO before adsorption that is 1.14 Å.

4.2.2 CO Bond Breaking

Figure 4-10 shows the complete CO breaking pathway on pure Co_{13}, Fe_{13}, Ni_{13}, and Ru_{13} nanoclusters. In figure, reactant corresponds to the structures with the PAS on their respective adsorption energies of pure clusters. For instance, in Table 4-1, the PAS of CO adsorption on pure Co_{13} cluster is the hollow site with the strongest adsorption energy of -1.65 eV compared to its top and bridge sites. Therefore, Co_{13} cluster with CO adsorbed on hollow position is the reactant for CO dissociation. This holds true for all the clusters. Similarly, the structures on the second row of Figure 4-10 correspond to the transition state structures as calculated by LST/QST methods implemented in DMol3. The vibrational analysis is performed to ensure that the computed transition state structures have one imaginary frequency. In some cases, more than one imaginary frequency has been obtained. When finding more than one negative frequency, the

corresponding (imaginary) modes of vibrations were animated in order to visualize the mode that would eventually follow the intended step from the particular reactant to product. Lastly, the third row of Figure 4-10 shows a completely split CO on the respective clusters and is termed as a product in the figure. These structures (reactant and product) resemble the energy minima structures exhibiting no negative frequency in the vibrational analysis.

The energy required to break the CO bond on the surface of the Co_{13} cluster is calculated to be 1.12 eV (Table 4-1). The transition state structure and the ground state structure of the completely split CO (product) are almost the same. The bond length of the CO when adsorbed on the hollow site (PAS on the Co_{13} cluster) is 1.22 Å. During the transition state, the CO bond breaks and oxygen bonds to a neighboring Co atom (Co (7)) and is 4.79 Å away from the carbon atom. The bond distance of O-Co (7) is 1.67 Å. Carbon atom binds at the hollow site and the bond distances for C-Co (9), C-Co (5), and C-Co (11) are 1.82 Å, 1.86 Å, and 1.79 Å respectively. On the completely separated CO on the Co_{13} cluster (product), the distance between the carbon atom and the oxygen atom is 5.38 Å. The bond distance of O-Co (7) changes to 1.65 Å. At the relaxed structure of completely dissociated CO, which is termed as the product in this study, the bond distance between C-Co (9), C-Co (5), and C-Co (11) are 1.83 Å, 1.82 Å, and 1.82 Å correspondingly. Similarly, the energy required to dissociate a CO molecule on the surface of Fe_{13} cluster is 2.29 eV. The PAS of a CO molecule on the Fe_{13} cluster is the top site with the CO bond length of 1.19 Å. At the transition state, CO bonds break completely, and carbon atom occupies the hollow position as in Figure 4-10. The oxygen atom is 2.02 Å away from the carbon atom and bonds with an Fe (4) atom with the bond

distance of 1.70 Å. A carbon atom occupies hollow position and the bond distances of C-Fe(13), C-Fe(4) and C-Fe(7) are 1.85 Å, 1.94 Å, and 1.85 Å respectively during the transition state. In the ground state structure of the completely detached CO molecule (product), oxygen atom occupies the hollow position with three Fe atoms (Fe (13), Fe (4), and Fe (7)) and is 3.60 Å away from the carbon atom which is bonded to three Fe atoms. At the product state, the bond distances between C-Fe (4), C-Fe (13), and C-Fe (7) are 1.86 Å, 1.85 Å, and 1.86 Å correspondingly. The oxygen atom binds at the hollow position of the Fe cluster with the bond lengths of 1.94 Å each with Fe (4), Fe (3), and Fe (11) atoms. Likewise, the PAS for CO molecule on the Ni_{13} cluster is the top site as seen in Figure 4-10 and from Table 4-1. The bond length of the CO molecule when adsorbed on the top site is 1.17 Å and C-Ni (7) is 1.77 Å. At the transition state, the CO bond breaks totally, and the oxygen bonds to two Ni atoms, namely Ni (7) and Ni (13). On the other hand, the carbon atom occupies a hollow position on Ni_{13} cluster making a bond with three Ni atoms, i.e. Ni (5), Ni (7) and Ni (9), with C-Ni (7) = 1.84 Å and C-Ni (9) = 1.80 Å. At this state, the oxygen atom is 1.95 Å away from the carbon atom and the bond distance of O-Ni (13) is 1.85 Å and O-Ni (7) is 1.92 Å. While on the ground state structure of the completely dissociated CO molecule on the Ni_{13} cluster (product), the carbon occupies the hollow position with three Ni atoms same as in the transition state and the oxygen atom also occupies the hollow position on the Ni_{13} cluster. The oxygen atom is 3.48 Å away from the carbon atom. The bond distances of the carbon atom with three metal atoms and the bond distances of the oxygen with three metal atoms are given as C-Ni (5) = 1.79 Å, C-Ni (7) = 1.81 Å, and C-Ni (9) = 1.79 Å and O-Ni (8) = 1.88 Å,

O-Ni (7) = Å, and O-Ni (13) = 1.88 Å. The energy required to break the CO bond on the surface of the Ni_{13} cluster is 2.47 eV.

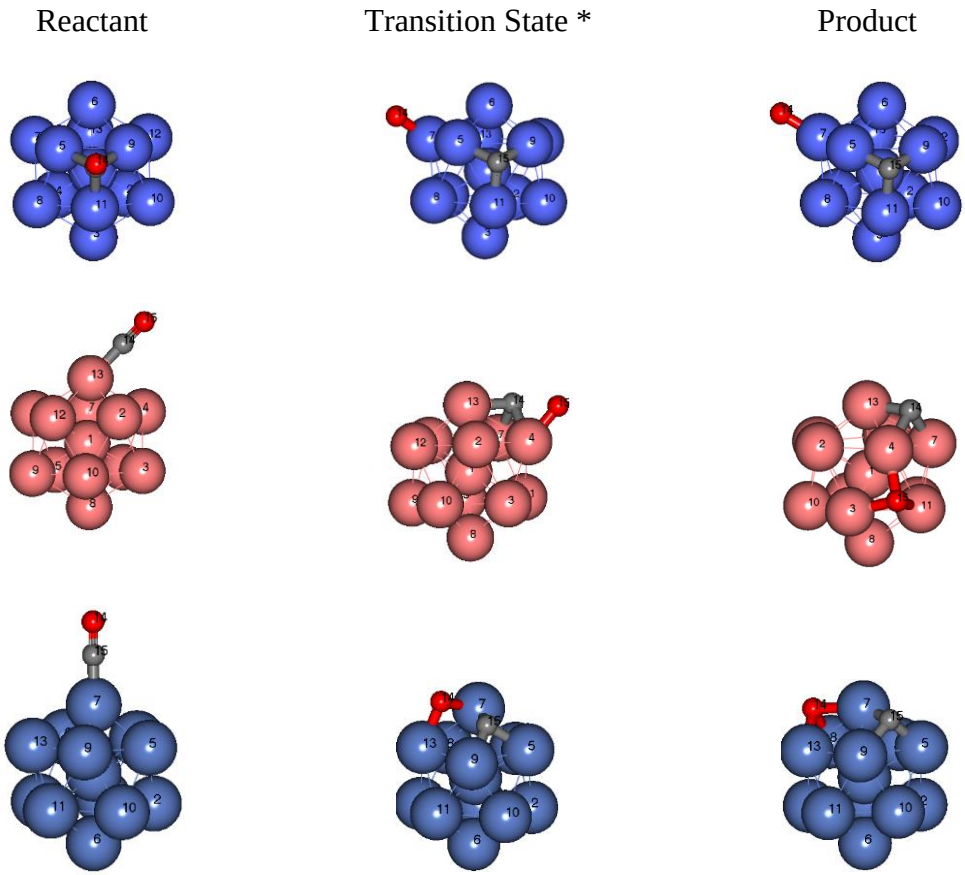

Figure 4-10: CO dissociation pathway on pure Co_{13}, Fe_{13}, Ni_{13}, and Ru_{13} nanoclusters. The first picture on each set corresponds to the reactant (cluster with CO adsorption on PAS), the middle corresponds to the transition state, and the last picture is the product (fully dissociated CO)

Last is the preferred adsorption site for the CO adsorption on the Ru cluster is top position (Table 4-1) with the binding energy of -2.68 eV. The CO bond length is measured to be 1.19 Å and C-Ru(5) is 1.89 Å. At the transition state, the oxygen atom completely detaches from the carbon atom, and bonds to another Ru atom (Ru (9)) in the cluster. The oxygen atom is 1.94 Å away from the carbon atom at the transition state. The bond distance between C-Ru(5) is 1.74 Å and O-Ru(9) is 1.97 Å. Fully relaxed structure

of completely dissociated CO on Ru cluster (product) has the oxygen atom bonded to the hollow site of the cluster with Ru(9)-Ru(11)-Ru(5). The bond distance between C-Ru(5) is 1.69 Å and O-Ru(9) is 2.08 Å, O-Ru(11) is 2.04 Å, and O-Ru(5) is 2.17 Å, and the oxygen is 3.36 Å away from the carbon.

After determining the PAS, transition states, and the energies to break CO bond, percentage difference is calculated as mentioned in **Eq. 2-17**. Looking at the adsorption energies and the dissociation energies, the percentage difference shows that the quantity is highest for the Ru cluster (66%), followed by the Co cluster (38 %). The percentage difference indicates negative values for the Fe cluster (-42%) and the Ni cluster (-33%). This information can also be used to construct bimetallic cluster for FT catalyst. Negative percentage difference indicates that the CO dissociation is not favorable on those pure clusters, and the reaction may proceed with the assistance of a hydrogen atom. Hence, according to the percentage difference catalysts, Ru and Co clusters show potential as FT catalysts and that these are the most active catalysts for the FTS.

4.3 Summary

Table 4-3 summarizes the finding of this chapter. All the 13-atom clusters have shown chemisorption of the CO molecule on their surface. Co_{13} and Ru_{13} clusters have shown the best potential to break the CO bond on their surface with the %Diff of 38 and 46% respectively. Fe_{13} showed the worse potential among all the 13 atoms pure clusters studied in this chapter with a percentage difference of -42%.

Table 4-3: Summary of the findings, PAS represents preferred adsorption site, E_{ads} is the CO adsorption energy on PAS, E_{diss} is the energy required to break the CO bond, and %Diff is the catalyst performance indicator based on CO adsorption and its bond breaking

System	PAS	E_{ads} (eV)	E_{diss}(eV)	%Diff
Co_{13}	Hollow	-1.65	1.12	38
Fe_{13}	Top	-1.49	2.29	-42
Ni_{13}	Top	-1.77	2.47	-33
Ru_{13}	Top	-2.68	1.35	46

CHAPTER 5

RESULT III-BINARY 13 ATOMS A_1B_{12} CATALYST MODELS (A, B= CO, FE, NI, RU, PT, PD)

In catalysis, the properties of the catalysts such as stability, enhanced surface properties towards the selectivity of the desired product, and withstanding catalysts poisoning can be achieved through various means such as by adding promoters, exploring different supporting materials, and investigating different catalysts surfaces. Because of the chemical composition of the bimetallic catalysts, the properties of the catalysts vary more dramatically than those of pure materials [59–61]. Therefore, bimetallic catalysts have received special attention in the past few years.

In the previous chapter, magic cluster structures for Co, Fe, Ru, and Ni were sorted out. Clusters with 13 atoms and icosahedra symmetry were determined as the most stable structure. These structures are known to have structural, electronic and thermodynamic stability [62]. Therefore, all the bimetallic clusters that will be studied in this chapter are based on the clusters with the most stable structures from the previous chapter. Core-shell configurations have been adopted as bimetallic clusters where well-defined 12 atoms shell embeds a single transition metal atom at the central position. The input structures for this core-shell model has been taken based on literature [61].

The computational details for this study are discussed in chapter 3 in section 3.2.

5.1 Stability of Bimetallic Cluster

Using a global optimization approach that directly searches for the global minima in both composition and configuration space, Doye and Meyer [61] were able to find particularly stable structures for binary Lennard-Jones (LJ) clusters with up to 100 atoms. In that study, the nature of the atomic species was introduced by varying the LJ parameters for a generic A-B binary system. Moreover, the strength of the interactions between atoms A and B was assumed to be the same, but the atom types were allowed to have different sizes. These authors found that those structures typically exhibited a core-shell type of arrangement, with the smaller atoms in the core of the cluster and the bigger ones surround them in the outermost shell. Thus, the cluster size of 13 atoms was found to be the very first cluster exhibiting great stability; a fact that seemed not to be very sensitive to the strength of the LJ parameters, i.e. nature of the atomic species forming the binary cluster [63]. Since, the most stable structure possesses an icosahedral structure that consists of two zig-zagged pentagonal rings, two apex atoms, and a central atom. In this study, therefore, clusters containing 13 atoms were selected as the cluster size of the models representing pure and binary combinations of Co, Fe, Ni, Pd, Pt, and Ru.

.In the case of binary systems A_nB_m, where A and B are different elements, B_m refers to the magic number clusters as computed from the previous chapter such as Co, Fe, and Ni and A refers to the single atom of Co, Fe, Ni, Ru, Pd, and Pt which embeds the central position of the cluster. For further detail about the structures of these binary clusters please refer to reference [60]. Doye and Meyer [61] have also found that 13 atom clusters with A_1B_{12} composition to be the most stable clusters. Figure 5-2 shows all the geometry optimized structures for bimetallic clusters.

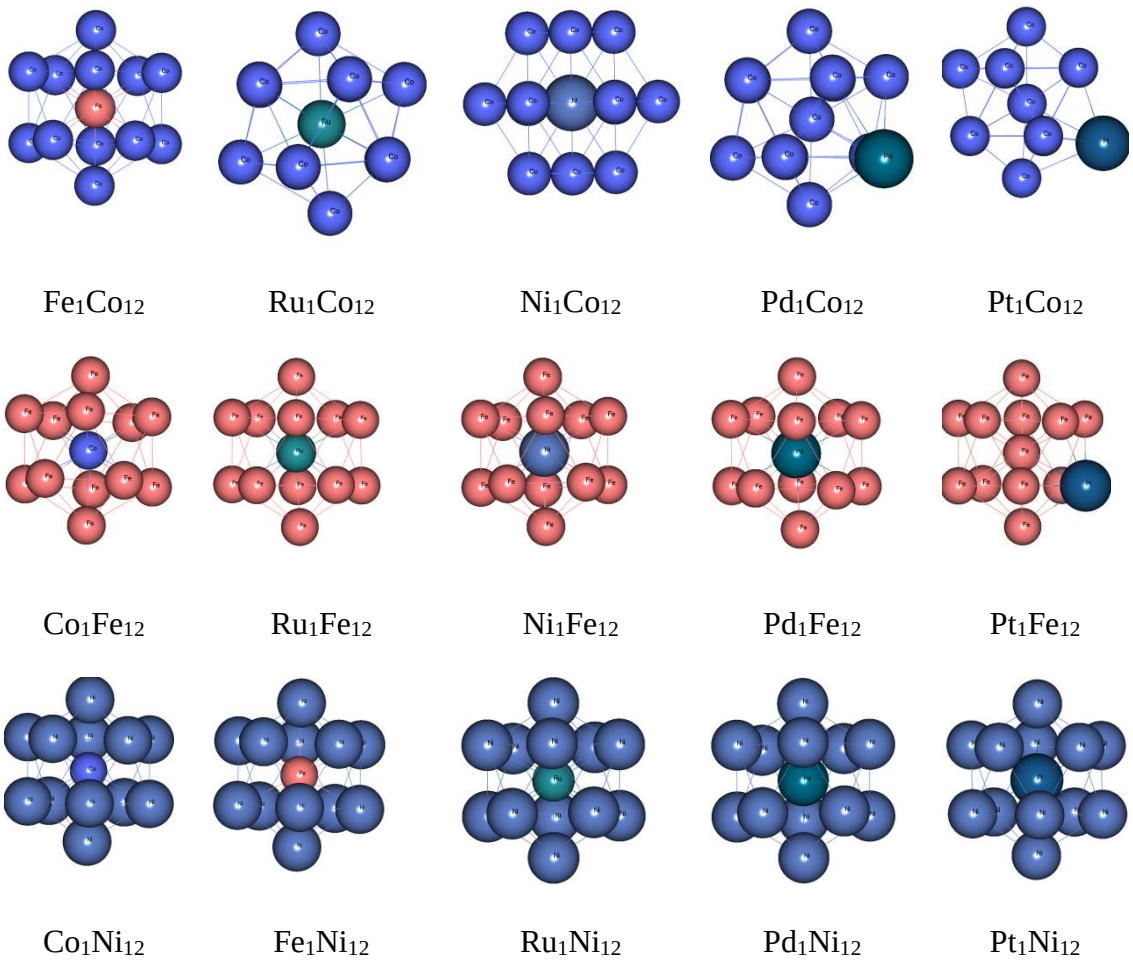

Figure 5-1: Geometry optimized structures of the most bimetallic 13-atom clusters containing combinations Co, Fe, Ni, Pt, and Pd at GGA/RPBE theory level

5.1.1 Nanoparticle Cohesive Energy

Input structures for the study of minimum energy structures and cohesive energies of the bimetallic clusters A_1B_{12} were created just by replacing the central atom of B_{13} presented in chapter 5 clusters with A atom. Figure 5-1 shows that all the structures hold icosahedra geometries except for Ni_1Co_{12} bimetallic cluster. Geometry optimization performed at the RPBE theory level suggests that the cluster Ni_1Co_{12} does not retain icosahedral symmetry after minimization. It rather preferred cub-octahedron structure as the most stable structure. On the other hand, bimetallic clusters such as Pd_1Co_{12}, Pt_1Co_{12},

and Pt_1Fe_{12} are the cases where the central atom (Pd and Pt) segregates to the surface of Co cluster and Pt segregates to the surface of the Fe cluster in search for the most stable configuration. At the same time, these clusters hold the icosahedra symmetry while finding the ground state geometry.

The cohesive energies were calculated using **Eq. 3-1** based on the energies of the ground state structures of the cluster illustrated in Figure 5-1. The calculated values of cohesive energies for the different combinations of the bimetallic clusters are presented in Figure 5-2.

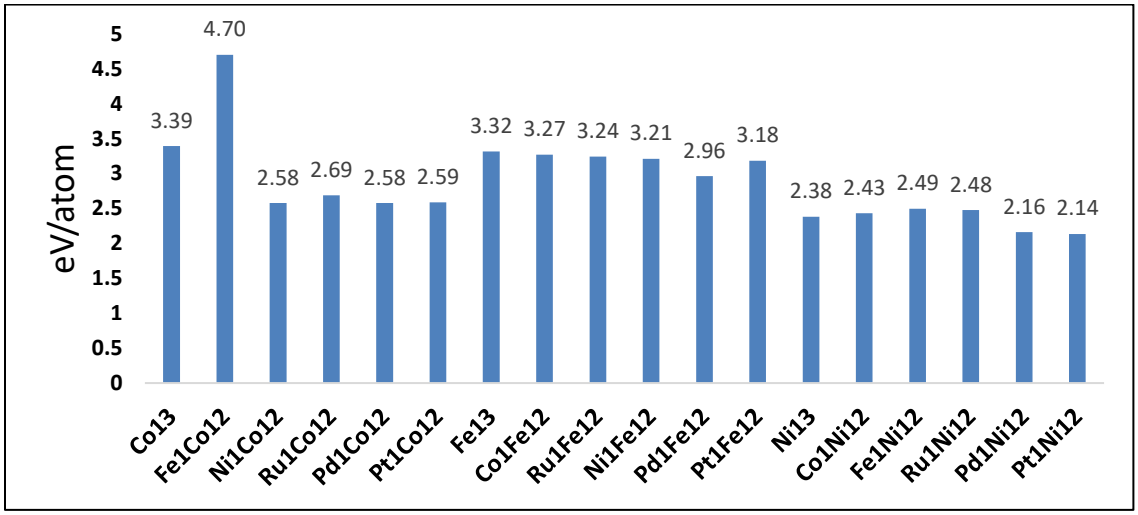

Figure 5-2: Cohesive energies of A_1B_{12} combinations of Co, Fe, Ru, Ni, Pd, and Pt

The Cohesive energies of the bimetallic clusters are compared with the 13 atom pure cases icosahedral structures. The cohesive energies of the pure cases, 13 atoms icosahedral clusters, were obtained from the previous chapter. Cohesive energy also determines the binding strength of respective atoms in that particular cluster. According to the cohesive energies, in the A_1Co_{12} family, Fe_1Co_{12} structure is more stable than the pure Co_{13} cluster by 1.31 eV and all the other bimetallic clusters based on A_1Co_{12}

combinations. The other clusters such as Ni_1Co_{12}, Ru_1Co_{12}, Pd_1Co_{12}, and Pt_1Co_{12} are less stable structures compared to pure Co_{13} cluster. In the case of the A_1Fe_{12} family, Co_1Fe_{12} and Ru_1Fe_{12} exhibit almost equivalent cohesive energies compared to the cohesive energy of an Fe_{13} cluster. The cohesive energy difference between Fe_{13} and Co_1Fe_{12} is 0.04 eV and Fe_{13} and Ru_1Fe_{12} is 0.07 eV. While other structures such as Ni_1Fe_{12}, Pd_1Fe_{12}, and Pt_1Fe_{12} are less stable than Fe_{13} cluster. Lastly, in the case of the A_1Ni_{13} family clusters, Co_1Ni_{12}, Fe_1Ni_{12}, and Ru_1Ni_{12} reveal stronger cohesive energies compared to Ni_{13} cluster. Clusters such as Pd_1Ni_{12} and Pt_1Ni_{12} exhibit weaker cohesive energies than pure Ni_{13} cluster by 0.22 eV and 0.25 eV respectively.

5.2 CO Adsorption and Its Bond Breaking

For the study of CO adsorption and CO bond breaking, the bimetallic cluster was selected based on their cohesive energies. Clusters with higher cohesive energies, when compared to the cohesive energies of the pure cluster, were selected. For the case of A_1Co_{12}, Fe_1Co_{12} shows enhanced cohesive energy compared to the Co_{13} cluster. Similarly, Co_1Fe_{12} and Ru_1Fe_{12} clusters were chosen among the bimetallic cluster based on their stability over the pure Fe_{13} cluster. Lastly, Co_1Ni_{12}, Fe_1Ni_{12}, and Ru_1Ni_{12} are chosen among the bimetallic clusters based on their stability over the pure Ni_{13} cluster.

5.2.1 CO Adsorption on Bimetallic Clusters

CO adsorption were investigated on the selected bimetallic clusters. The core atom (A) in the A_1B_{12} cluster does not create any adsorption site for the respective bimetallic cluster. CO is adsorbed only to the atoms (B) at the shell. Thus only three sites (top, bridge, and hollow) were studied for the CO adsorption. The configurations of CO when adsorbed in the top, bridge, and hollow position are shown in Figure 3-5. The

energy values for the adsorption of CO on different sites of the bimetallic cluster are presented in Table 5-1.

Table 5-1: CO adsorption and CO bond breaking on the bimetallic clusters

Catalyst	Adsorption sites/ E_{ads} (eV)			PAS	E_{diss}(eV)
	Top	Bridge	Hollow		
Fe_1Co_{12}	-0.91	-1.37	-0.89	**Bridge**	2.54
Co_1Fe_{12}	-1.13	-1.14	-1.15	**Hollow**	1.42
Ru_1Fe_{12}	-1.19	-1.18	-1.09	**Top**	2.61
Co_1Ni_{12}	-1.39	-1.31	-1.42	**Hollow**	1.80
Fe_1Ni_{12}	-1.34	-1.32	-1.41	**Hollow**	2.52
Ru_1Ni_{12}	-1.28	-1.29	-1.37	**Hollow**	2.50

Substitution of a Fe atom in Co_{13} cluster (Fe_1Co_{12}) do not show any enhancement in CO adsorption neither lowers CO dissociation energy. Similarly, substitution of impurities such as Co and Ru on the pure 13 atoms Fe cluster does not show any improvement in the adsorption of CO. Adsorption of CO has remained stronger in the Fe_{13} cluster with the adsorption energy of -1.49 eV at the top configuration. But the introduction of a Co atom in the cluster lowered the CO dissociation energy of pure Fe_{13} cluster from 2.29 eV to 1.42 eV. In the case of an A_1Ni_{12} cluster, the same pattern has been observed. The binding of CO on the top site of the Ni_{13} cluster has been the strongest with adsorption energy of -1.77 eV.

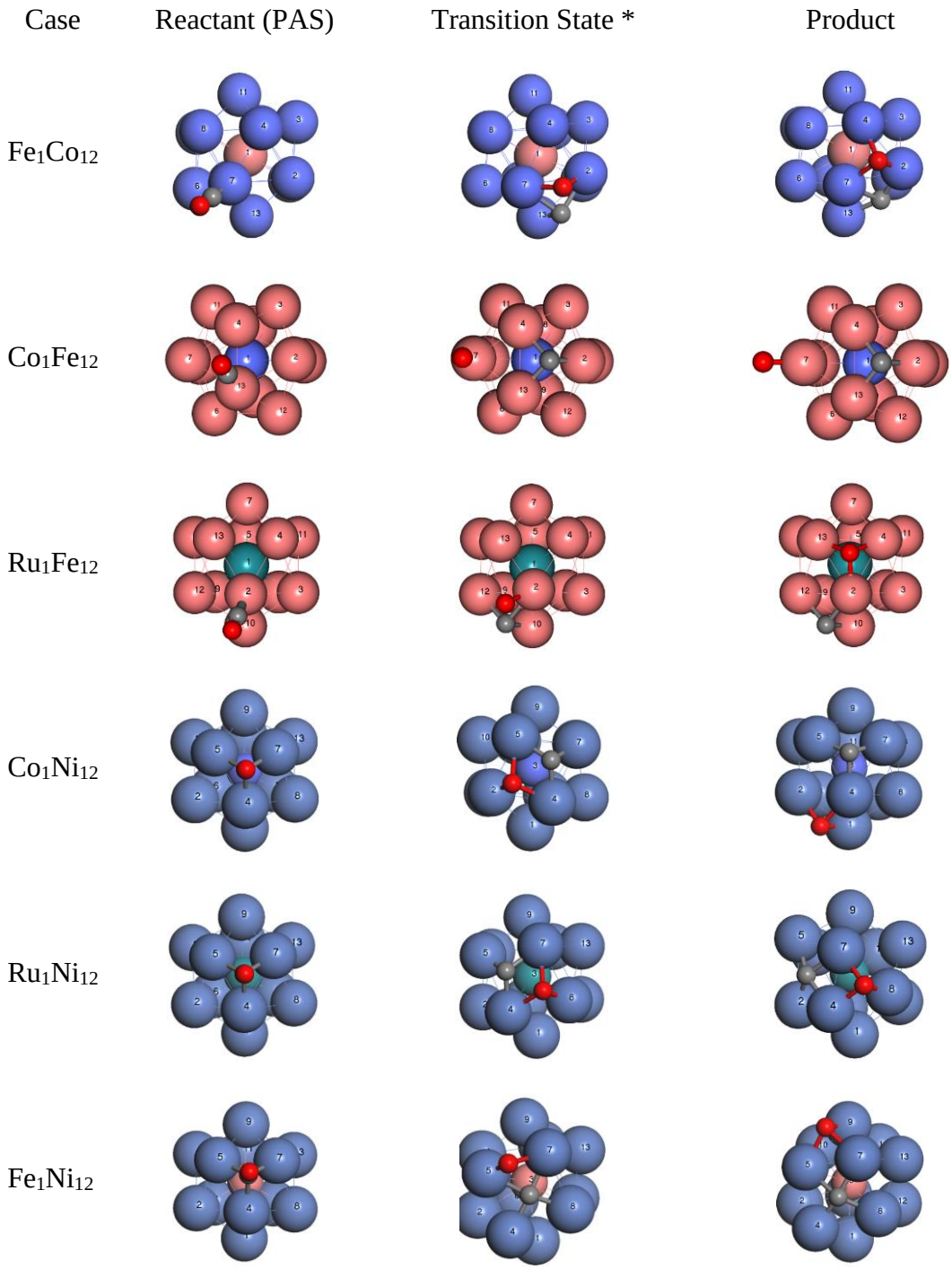

Figure 5-3: CO bond breaking pathway on bimetallic nanoclusters. The first picture on each set corresponds to the reactant (cluster with CO adsorption on PAS), the middle corresponds to the transition state, and the last picture is the product

When Co was added to Ni_{13} cluster, it lowered the CO dissociation energy from 2.47 eV to 1.8 eV. Therefore, addition of Co atom in Fe and Ni clusters may enhance the catalytic property of the cluster by lowering CO dissociation energy.

5.2.2 CO Bond Breaking on Bimetallic Clusters

The energy required to break the CO molecule or dissociation energy of CO (E_{diss}) on the selected catalysts is reported in Table 5-1. After finding the dissociation energy of CO on the surface of the bimetallic clusters, percentage difference calculation was carried out using **Eq. 2-18**. The calculated percentage difference is lowest for Ru_1Fe_{12} with the value of -75% followed by Ru_1Ni_{12} with the value of -58 %. Similarly, the percentage difference value for Co_1Fe_{12}, Co_1Ni_{12}, and Fe_1Ni_{12} are -21 %, -24 %, and -56%. But, looking at the pure Fe_{13} cluster (-42%), the percentage difference indicates that Co_1Fe_{12} (-21 %) is better than pure Fe_{13} cluster. This is an indication that Co-Fe bimetallic system at right composition can be an ideal catalyst for FT application. Compared to pure Ni_{13} cluster (-33%), Co_1Ni_{12} (-24%) is better than pure Ni_{13} cluster. Percentage difference calculations indicate that none of the bimetallic clusters will facilitate CO bond breaking on their surface.

5.3 Summary

Table 5-2 summarizes the findings of chapter 3, 4 and 5. The best catalysts for the FT synthesis out of those studied here are highlighted in bold. Pure ruthenium cluster with 13 atoms shows the best performance among all the clusters with the CO adsorption energy of -2.68 eV and %Diff of 66%. This is followed by the pure 13 atoms Co cluster with the adsorption energy of -1.65 eV and %Diff of 38%. Among all the bimetallic catalysts investigated in this study, CoFe catalyst with 10 cobalt atoms and 4 iron atoms

also show the best performance compared to the pure Co cluster. Similarly, FeCo system, despite having negative percentage difference, shows improved performance when compared with the pure clusters (Co_{14} and Fe_{14}). The CO adsorption energy is the strongest among all 13 atom and 14 atom catalysts with the value of -3.94 eV and % Diff is 37% which is almost like the pure Co_{13} cluster.

Table 5-2: Summary of all the systems (14 atom pure and binary clusters), 13 atom pure and binary clusters, PAS of CO adsorption on them, energy required to break the CO bond on those clusters, and %Diff

System	PAS	E_{ads} (eV)	E_{diss}(eV)	%Diff
Fe_1Co_{12}	Top	-1.37	2.54	-60
Co_1Fe_{12}	Top	-1.13	1.42	-21
Ru_1Fe_{12}	Top	-1.19	2.61	-75
Co_1Ni_{12}	Hollow	-1.42	1.80	-24
Fe_1Ni_{12}	Hollow	-1.41	2.52	-56
Ru_1Ni_{12}	Hollow	-1.37	2.50	-58
Co_{13}	**Hollow**	**-1.65**	**1.12**	**38**
Fe_{13}	Top	-1.49	2.29	-42
Ni_{13}	Top	-1.77	2.47	-33
Ru_{13}	**Top**	**-2.68**	**1.35**	**66**
Co_{14}	Top	-1.73	2.21	-24
Fe_{14}	Top	-2.00	3.20	-46
FeCo (10:4)	Top	-2.60	3.02	-15
FeCo (10:4)	Hollow	-2.72	2.78	-2
CoFe (10:4)	**Hollow**	**-3.81**	**2.67**	**35**
CoFe (10:4)	**Top**	**-3.94**	**2.71**	**37**

CHAPTER 6

RESULT IV- SILICA SUPPORTED 13-ATOM CO, RU, AND FE CLUSTERS

Supported catalysts have received widespread attention for Fischer-Tropsch synthesis. Highly dispersed Fe catalysts on supports not only lowered the water gas shift reaction but it also helped to achieve high conversion of hydrocarbon products [64]. A strong interaction between the catalysts and the support under the reacting conditions helps to prevent nanoclusters from aggregation as well as to maintain catalytic stability for an extended period. In order to preserve the activity and stability of the nanoparticles, supporting materials with strong metal-support interaction (SMSI) play a very important role [65]. This does not only prevent nanoclusters from being agglomerated but will also retain their chemical stability and adsorption sites [66]. Hence, different support materials such as alumina, silica, carbon nanofibers, and zeolites have been explored in search of SMSI for heterogeneous catalytic reactions [67].

There are many studies done with surface science techniques to understand the structural properties of the supported metal species at the atomic level. The electronic interaction of the metal catalysts and the metal oxide supports vary among catalysts and supporting materials. For instance, Au prefers to attach at the edge sites on Anatase TiO_2<101> while Pt prefers terrace and edges [68-69]. Similarly, there are studies which concluded that the use of TiO_2 as a support for metal clusters promotes the catalytic

activity of the metal clusters [67]. TiO_2 <110> is the most investigated surface out of different planes of rutile because it is thermodynamically stable. Studies have also addressed that surface defects also play an important role in the structural, electronic, and catalytic properties of deposited metal particles [70–73].

Therefore, the effect of support such as silica and rutile on the adsorption of a pure 13 atom cluster of Co, Fe, and Ru were investigated using DFT. The 13 atoms pure clusters based on Co, Fe, and Ru were selected based on their percentage difference performance which were better than any of the bimetallic clusters studied previously. DMol3 calculations and percentage differences study had shown that Ru_{13} and Co_{13} clusters show the best performance favoring CO dissociation as the first reaction step on the surface of the catalysts while on the other hand Ni_{13} and Fe_{13} cluster did not show the same result. With Ni, the primary product of the reaction is methane hence it will be no longer taken into consideration as a catalyst for the further study [74]. Similarly, none of the bimetallic clusters that were studied showed a tendency to break the CO bond on their surface. Therefore, the effect of support on CO adsorption is only studied for Co_{13}, Fe_{13}, and Ru_{13}.

All the calculations were performed using the Vienna Ab Initio Simulation Package (VASP)[21–23]. Details are explained in section 6.1. At first, CO adsorption was carried out on isolated clusters. Then the cluster adsorption, as well as CO adsorption on this adsorbed clusters on the different planes of silica support (this chapter) and rutile support (chapter 7) was studied.

6.1 Computational Details

Geometry optimization of the structures were performed using the GGA functional of Perdew, Burke, and Ernzerhof [75] with plane-wave basis sets was used for the study. Spin-polarized calculations were performed since transition metals are the subject of the study. The electron-ion interaction was described using the projector augmented wave methods with plane waves up to an energy of 450 eV. The Fermi level was smeared by the Methfessel and Paxton approach with a Gaussian width of 0.1 eV. For all the calculations, the equilibrium geometries were obtained when the atomic forces are less than 0.01 eV/Å and with the total energy convergence of within 10^{-5} eV. The geometry optimization procedure was carried out using the conjugate-gradient method as employed in VASP.

The breaking of the CO bond on the silica and rutile supported clusters was investigated using the Nudge Elastic Band method (NEB). For the transition state calculation, all the atoms except C and O were frozen during the geometry optimization of the product species. As mentioned in the earlier chapters, the transition state calculations require two energetically stable structures which are termed as reactant and product. The structures with CO adsorbed on the PAS on each silica and rutile supported clusters were considered as the reactant in each case. The products were the geometry optimized structures with CO fully split on the surface of the supported clusters. 5 images were created between the known reactants and product for each system for finding the transition state structures. Climbing image (CI) method was utilized along with NEB which allows for the more accurate finding transition state points along the MEP.

6.2 Isolated Clusters

Clusters based on Co, Fe, and Ru were created which consist of 13 atoms and icosahedron symmetry. Plane wave basis sets require periodic boundary conditions. Therefore, the clusters were placed at the center of a periodic box with a size of 25 Å x 25 Å x 25 Å. The size of the box is large enough to avoid interactions with the periodic image. A pictorial representation of this model can be seen in Figure 6-1.

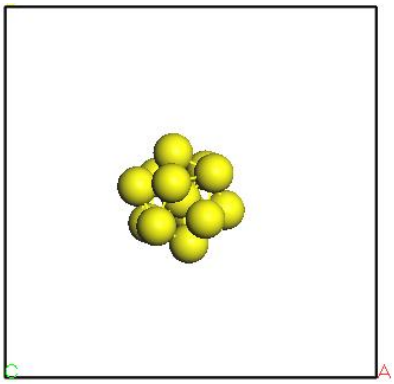

Figure 6-1: 13 atoms cluster in a cube box of 25Å x 25 Å x 25Å

CO adsorption was studied on these isolated 13 atoms clusters of Co, Fe, and Ru at the PBE and RPBE theory levels. The adsorption sites on these clusters are shown in Figure 3-5.

The adsorption energies calculated using the PBE functional are higher than the energies calculated using the RPBE functional. Although there is a difference in numbers, the same trend is seen in CO adsorption energies except for the Fe cluster. For example, the PBE functional predicts that the adsorption energies of CO on top, bridge, and hollow sites of the pure 13 atoms Co cluster are -2.42, -2.48, and -2.52 eV respectively. Therefore, the preferred adsorption site of CO on the surface of the Co cluster is the hollow site followed by the bridge, and finally the top.

Table 6-1: CO adsorption energy on 13 atom clusters of Co, Fe, and Ru calculated at PBE and RPBE theory levels with Plane-wave basis sets

Catalyst	Adsorption sites/ E_{ads} (eV)		
	Top	Bridge	Hollow
Cobalt			
PBE	-2.42	-2.48	-2.52
RPBE	-1.38	-1.56	-1.58
Iron			
PBE	-3.2	-3.7	-1.75
RPBE	-0.35	-2.24	-2.07
Ruthenium			
PBE	-2.34	-2.49	-2.38
RPBE	-1.8	-1.96	-1.86

Similarly, the RPBE functional predicts the same but with smaller adsorption energies (see Table 6-1). A similar trend is obtained for the CO adsorption on the Ru cluster. The PBE and RPBE functional predicts the PAS to be the bridge site followed by hollow and top sites. With the PBE functional, the PAS on the Fe cluster is calculated to be the bridge followed by the top and hollow site respectively while the RPBE functional predicts the bridge followed by the hollow and top site correspondingly as the PAS. In this case, although the PAS is identified the same at PBE and RPBE theory level, RPBE predicts that the CO adsorption on the bridge site is the second preferred site followed by the hollow site while PBE predicts hollow position as the second preferred site for the CO adsorption followed by the hollow site.

The comparative study of PBE and RPBE functionals on clusters also suggested that PBE was the best option with Plane wave basis sets over RPBE functional in terms

of computational time. Therefore, PBE functional is chosen for the further study that includes support.

6.3 Support

A catalyst support plays an important role in heterogeneous catalytic reactions such as the FT reaction. Supports such as silica, rutile, and alumina are widely studied for FT applications. In this work, different miller planes such as the <100>, <110>, and <111> of crystalline silica was chosen to study the interaction of the support with the clusters and the effect of support on the CO adsorption and dissociation. The number of surface atoms and surface dangling bonds is always different for silica when comparing between these surface planes. These surface atoms and dangling bonds play a very important role in the chemical interaction between the clusters and the surface. A p(2x2) unit cell was created for all the different planes of silica with a vacuum space of 30 Å. K space sampling was performed using the scheme of Monkhorst and Pack [76] with the k-point mesh of 4x4x1. All the other computational parameters are explained in section 6.1.

6.3.1 Silica as Support

Silica (SiO_2) has two allotropic phases, amorphous and crystalline. Silica is an important material from the geological and materials science points of view. Silica has a number of distinct crystalline forms and α-quartz is one of them [77]. α-quartz silica is abundantly available in nature and abundant info is available to check the accuracy of the input parameters in DFT. The lattice constants of the α-quartz silica unit cell obtained from this study were compared to available data and found to agree well with the corresponding experimental values for α-quartz silica.α-quartz silica has SiO_4 tetrahedral arranged around a hexagonal axis [71].

Table 6-2: Structural parameters such as experimental lattice constants, bond lengths (Å), and bond angles of α-quartz silica and also the corresponding ones obtained at the GGA/PBE theory level [71]

α-quartz Silica (exp)	α-quartz Silica (theory)
a=b=4.916Å	a=b=4.913 Å
c = 5.405 Å	c= 5.405 Å
Si-O-Si = 143.7 º	Si-O-Si = 143.7º
Si-O = 1.614 Å	Si-O = 1.609 Å

After optimizing the silica unit cell, the crystal is cleaved into three different planes, <100>, <110>, and <111>, with the size of a p(2x2) supercell. Geometry optimizations at a layer with a 20 Å vacuum slab were performed at the GGA/PBE theory level. Geometry optimized structures of silica <100>, <110>, and <111> are presented in Figure 6-2.

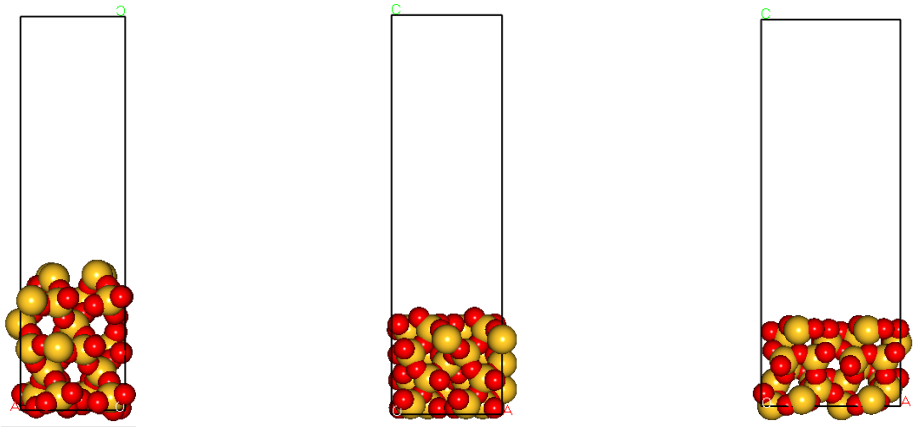

Silica <100> surface Silica <110> surface Silica <111> surface

Figure 6-2: Geometry optimized structures of silica <100>, <110>, and <111> at the GGA/PBE theory level (Yellow: Si, Red: O)

After finding the ground state structures for different surface terminated models of silica, cluster adsorption on these surfaces was performed. 13 atom clusters with icosahedron symmetry were placed at least 3 Å above on the different silica surfaces. Then, the relaxation of the structure was performed again at the same theory level. The binding energy (interaction of cluster on the different surface terminated models) was calculated using **Eq. 6-1**.

$$Binding\ Energy = Energy\ (slab + cluster) - Energy(slab) - Energy(cluster) \quad \textbf{Eq. 6-1}$$

where *Energy (slab+cluster)* = total energy of the geometry optimized surface with a cluster on top of it.

Energy (slab) = energy of the surface terminated models only,

Energy (cluster) = energy of the pure case 13 atom clusters.

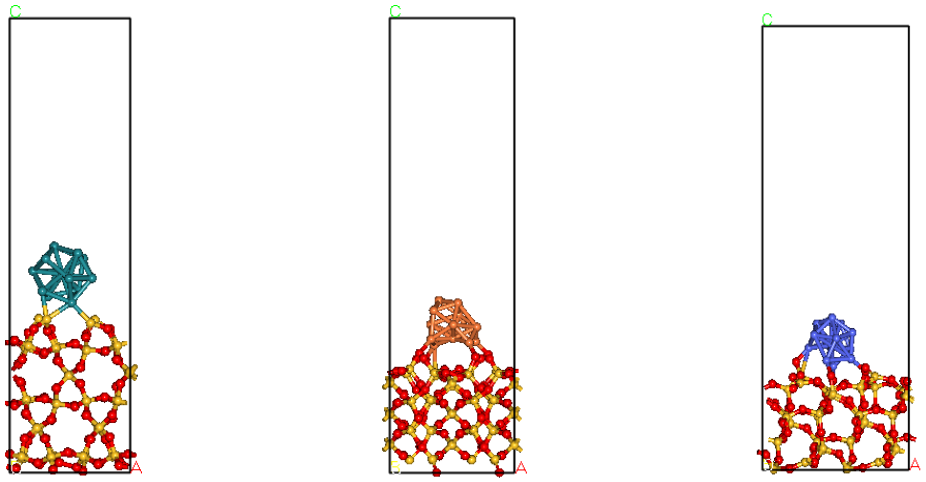

Ru_{13} on Silica <100> Fe_{13} on Silica<110> Co_{13} on Silica <111>

Figure 6-3: Side view of cluster adsorption on silica <100, <110>, and <111> surface

GGA/PBE predicts that the overall interaction between the clusters and the silica <100> surface is the strongest interaction. On silica <100> surface, the interaction of the

Fe cluster is the strongest followed by the Ru cluster and the Co cluster. The binding energies between the surfaces and the clusters can be seen in Table 6-3.

Table 6-3: Binding energy (eV) between the clusters (Co_{13}, Fe_{13}, and Ru_{13}) and the silica surfaces (Silica <100>, Silica <110>, and Silica <111>)

Clusters	Silica <100>	Silica <110>	Silica <111>
Co	-22.61	-15.85	-19.36
Fe	-25.26	-21.54	-20.62
Ru	-23.46	-16.03	-20.22

Fe cluster also shows strong interaction with all the planes of silica when compared among Fe, Ru, and Co clusters on different planes of silica. Ru cluster on different planes of silica also show strong interaction but is less reactive than the Fe cluster. Co cluster also shows strong interaction to the silica planes but is less compared to Fe and Ru clusters. In order to understand the interaction between the clusters and the different planes of silica, study of Bader charges was performed. Bader charge analysis (Table 6-5) shows that all these clusters transfer charges to the silica support during the adsorption. A significant charge transfer resulted in strong binding energies of the clusters with the support. Bader charge values also correspond to the values of the binding energies of the clusters on the different planes of the silica support. Strong interaction (in terms of binding energy) and a significant amount of charge transfer from the clusters to the surface indicate the possibility of the reduction of the surface.

6.3.2 CO Adsorption and Its Bond Breaking

The CO adsorption study on the Co, Fe, and Ru clusters with silica support was performed at GGA/PBE theory level. The CO adsorption on top, bridge, and hollow sites

of the clusters with silica support are as illustrated in Table 6-4. GGA/PBE predicts the chemisorption of CO on the silica supported 13 atom clusters of Co, Fe, and Ru. When compared to the CO adsorption on the isolated clusters (Table 4-1), the CO adsorption on the clusters is affected due to the presence of support. In the case of the isolated Ru cluster, bridge site is identified as the PAS for CO adsorption. This is not true when the Ru cluster is supported on silica. With the silica <100> support, the hollow site is identified as the PAS for CO adsorption while on the silica <110>, top site is predicted to be a PAS. Similarly, the hollow site is found to be the PAS for CO adsorption on the Ru cluster with the silica <111> surface.

Table 6-4: CO adsorption energy (E_{ads}) and CO bond length when CO is adsorbed on the surface of adsorption sites of the silica-supported clusters. Results are obtained at the GGA/PBE theory level with PW basis sets

	Ru cluster			Fe cluster			Co cluster		
Silica <100>									
	Top	Bridge	Holl	Top	Bridge	Holl	Top	Bridge	Holl
E_{ads}(eV)	-0.89	-2.36	-2.46	-0.64	-1.29	-1.33	-2.93	-2.97	-2.91
CO (Å)	1.17	1.18	1.20	1.18	1.19	1.20	1.17	1.19	1.20
Silica <110>									
E_{ads}(eV)	-2.79	-1.97	-1.92	-2.22	-2.03	-2.34	-0.74	-0.61	-1.49
CO (Å)	1.17	1.22	1.24	1.17	1.19	1.20	1.16	1.17	1.20
Silica <111>									
BE(eV)	-7.59	-1.93	-2.35	-0.62	-1.77	-1.89	-1.72	-1.88	-1.97
CO (Å)	1.17	1.17	1.20	1.20	1.22	1.22	1.16	1.19	1.21

In the case of the isolated Fe cluster, the PAS for the CO adsorption is the bridge site. The PAS for the CO adsorption changes to the hollow site when the Fe cluster is

supported on the silica <100>surface. Similarly, PAS on the Fe cluster supported on the silica <110> surface remained unchanged (hollow site) and the CO adsorption energy of -2.34 eV equal to the energy for the CO adsorption energy on the PAS of the isolated Fe cluster. For the Fe cluster on the silica <111> support, the PAS for CO adsorption changes to the hollow site.

Lastly, in the case of the Co cluster, a different scenario is observed. The PAS for CO adsorption on the isolated Co cluster is a hollow site. On the silica surface <100>, the PAS site for CO adsorption changes to the bridge site. The PAS for CO adsorption on Co cluster with silica <110> planes changes to the hollow site. On the silica <111> support, the PAS changes to the hollow site.

6.3.3 Binding Energy (BE) Ratio

With the introduction of the support, not only the PAS has changed, but a change in the CO adsorption values was also observed. In order to compare the cluster performance on CO adsorption, BE ratio has been calculated using the following mathematical expression:

$$BE\ ratio = \frac{\min(BE\ (cluster{+}support))}{\min(BE\ (isolated\ cluster))} \qquad \textbf{Eq. 6-2}$$

where *min (BE (cluster + support))* = adsorption energy of the CO corresponding to the PAS on the supported cluster and *min (BE (isolated cluster))* = adsorption energy of the CO corresponding to the PAS on the clusters without support.

The following graph shows the calculated BE ratio on different clusters with support.

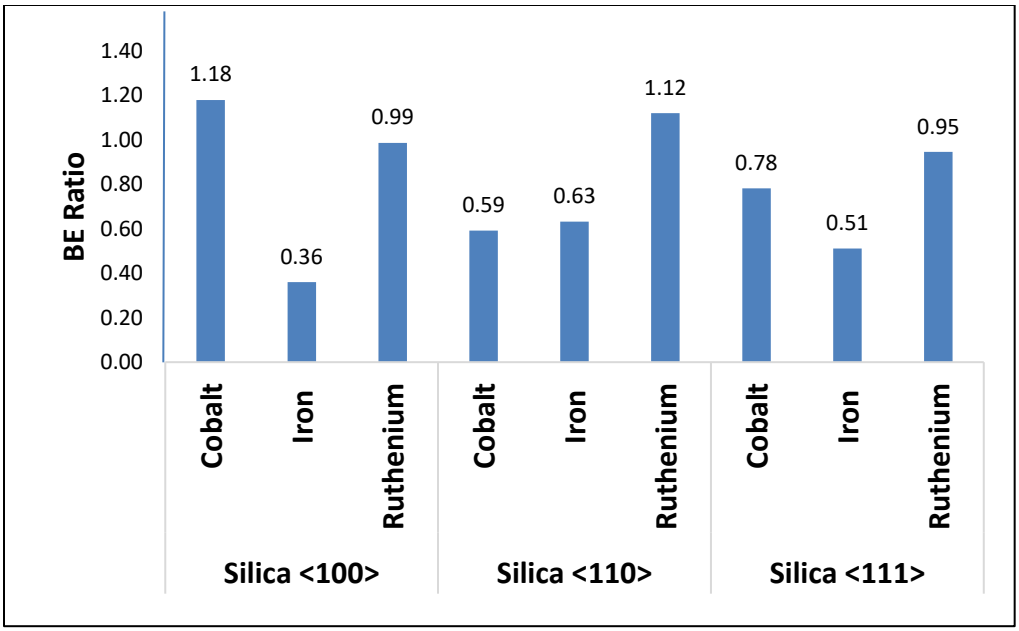

Figure 6-4: BE ratio of CO on clusters with silica support Vs isolated clusters

In Figure 6-4, the CO adsorption energy values for the PAS of the Fe and the Ru clusters on the silica <100> surface drops by 43% and 4% respectively compared to their respective isolated clusters. The Fe cluster on the silica <110> surface shows equal performance in adsorbing CO compared to the corresponding isolated cluster. The CO adsorption drops by approximately 40% on the PAS adsorption sites of the Co cluster on the silica <110> surface when compared to isolated Co cluster. Likewise, CO adsorption drops by 21% on the Co cluster, 19% on the Fe cluster, and 8% on the Ru cluster on the silica <111> support. Figure 6-4 shows that the Co cluster on the silica <100> has stronger CO adsorption than the corresponding isolated cluster on its PAS. Similarly, the next best cluster that strongly adsorbs CO on its surface is the Ru cluster on the silica <110> surface.

The binding of CO on the silica supported metal clusters has shown the chemisorption of CO on the isolated clusters as well as on the clusters with support

despite enhanced/diminished CO adsorption. For many heterogeneous catalytic reactions such as Fischer Tropsch, the reaction proceeds with the adsorption of CO at the beginning. As mentioned above, with the introduction of the catalyst support, the activity of the catalysts could be hindered, that can result in the deterioration of the catalytic properties.

6.3.4 Percentage Difference

CO dissociation on the surface clusters with different planes of the silica support was carried out in-order to calculate the percentage difference using NEB method. The theory level for transition state calculation is already discussed in section 6.1. The equation to calculate the percentage difference is given in **Eq 2-16**. The values for the CO adsorption on PAS, energy needed to break CO bond (E_{diss}), %Diff, and Bader charge on the clusters are given in Table 5-6. %Diff calculation show that none of the clusters on different planes of silica surface show tendency of breaking CO bond on their surface.

Table 6-5 CO adsorption on PAS (E_{ads}), CO dissociation energy (E_{diss}) , %Diff, and Bader (e)

Support	Catalyst	E_{ads} (eV) (PAS)	E_{diss}(eV)	%Diff (%)	Bader (e)
Silica <100>	Co_{13}	-2.97 (Bridge)	3.14	-6	3.91
	Fe_{13}	-1.33 (Hollow)	2.66	-67	4.69
	Ru_{13}	-2.46 (Hollow)	2.62	-6	3.94
Silica <110>	Co_{13}	-1.49 (Hollow)	3.11	-70	2.8
	Fe_{13}	-2.34 (Hollow)	3.15	-30	3.95
	Ru_{13}	-2.79 (Top)	-3.00	-7	3.39
Silica <111>	Co_{13}	-1.97 (Hollow)	3.18	-47	2.98
	Fe_{13}	-1.89 (Hollow)	3.46	-59	3.47
	Ru_{13}	-2.35 (Hollow)	2.59	-10	3.27

6.3.5 Structural Stability of Clusters on Silica Support

In order to study the stability of the clusters on the oxide support, the Radial Distribution Function (RDF) of the clusters have been generated. The first peak in the RDF corresponds to the bond distance between the first neighboring metal-metal atoms. The icosahedron symmetry of the metal clusters consists of two pentagonal rings, two apical atoms, and a center atom. All the atoms in the ring and at the apex are considered as the surface atoms in this report. The bond distance between the center atom and surface atoms of the cluster are included as the first neighboring atoms on these clusters. In order to analyze the structural stability of the clusters, the mean and standard deviation

(std) of the bond distances of the first neighbor i.e. the bond distances between the center atom and the surface atoms have also been calculated for all the clusters with/without support. The mean and std for the Co, Fe, and Ru clusters on different planes of silica is reported in Table 6-5, 6-6, and 6-7 respectively.

From the RDF of the Co cluster, the cluster is more stable on the silica <110> and <111> surfaces than on the silica <100> surface when compared with the ground state geometry of the isolated Co cluster. The Co cluster can retain its icosahedron symmetry on the silica <111> and silica <110> surfaces but this symmetry is broken when the cluster is supported on the silica <100> surface. The maximum distortion in the Co-Co bond length in the Co cluster is obtained when the cluster is on top of the silica <100> surface with the standard deviation of 0.22 Å followed by that on the <111> and <110> silica support with the standard deviation of 0.13 Å and 0.10 Å respectively.

From the RDF, the Fe cluster shows the most distortion when it is supported on silica <110> compared to other surfaces. The mean of the Fe-Fe bond distance between the center atom and surface atoms increases by 0.13 Å on the silica <110> surface, by 0.11 Å on the silica <100> surface, and by 0.05 Å on the silica <111> surface when compared with the ground state geometry of the isolated Fe cluster. The calculated standard deviation shows a big deviance in the Fe-Fe bond length between the center and surface atoms of the Fe cluster when the cluster is on the silica <110> surface ($\sigma = 0.29$ Å) and the least deviance is seen when the Fe cluster is on the surface of the silica <111> ($\sigma = 0.12$ Å). It is also very important to note the Fe cluster retains its symmetry on the silica <111> surface as well as on the silica <100> surface. In the case of the Ru cluster, the cluster exhibits a higher distortion when placed on the silica <100> surface where the

Ru-Ru bond distance mean shifts by 0.14 Å compared to the Ru-Ru mean bond distance in the isolated Ru cluster yielding the highest standard deviation (σ = 0.24 Å). Additionally, the structural symmetry of the Ru cluster also changes on the different silica surfaces, but the symmetry does not change much on the silica <111> surface.

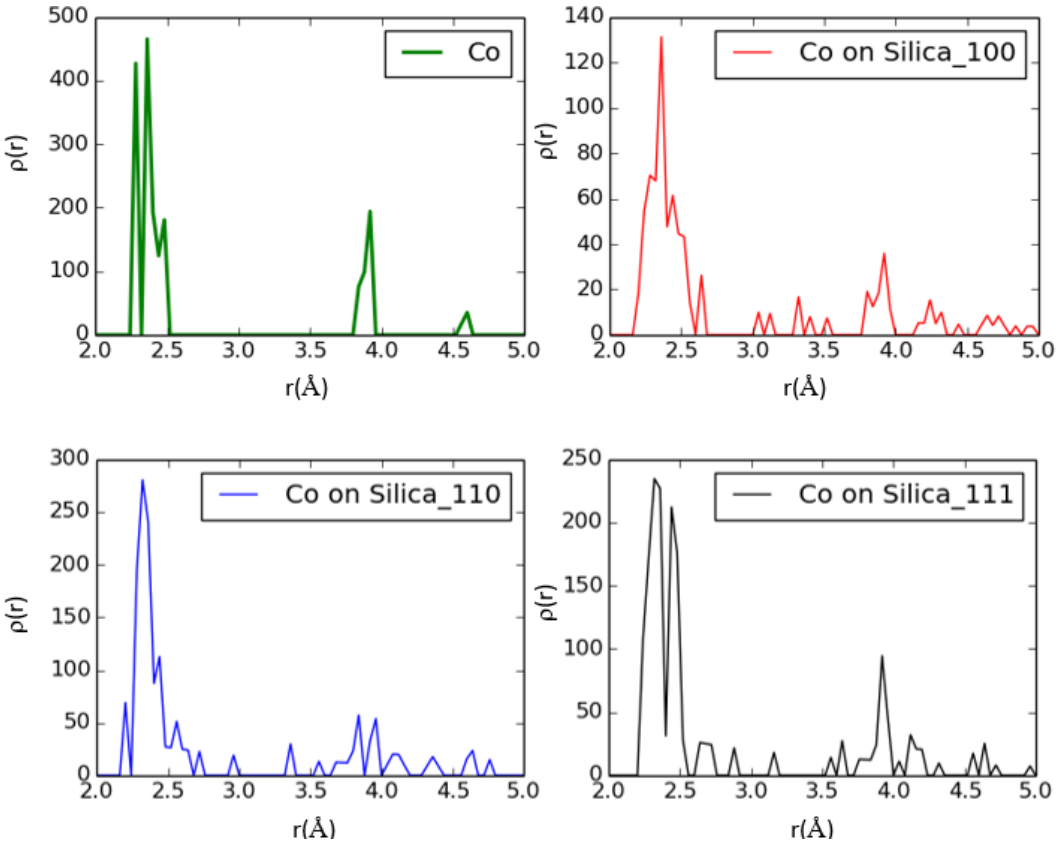

Figure 6-5: RDF of Co clusters. The first graph (green legend) shows the RDF for isolated Co cluster, the second graph (red legend) shows the RDF for the Co cluster on silica <100> surface. The third graph (blue legend) shows the RDF for the Co cluster on silica <110>surface, and the fourth graph (black legend) corresponds to the RDF for the Co cluster on silica <111> surface

Table 6-6: Mean bond length and standard deviation (σ) of bond length of the isolated cobalt cluster Vs cobalt cluster on the different planes of silica surface

Catalysts	Mean of the bond length (Å)	σ (Å)
Co_{13}	2.30	0.01
Co_{13} / Silica <100>	2.45	0.22
Co_{13} / Silica <110>	2.37	0.10
Co_{13} / Silica <111>	2.35	0.13

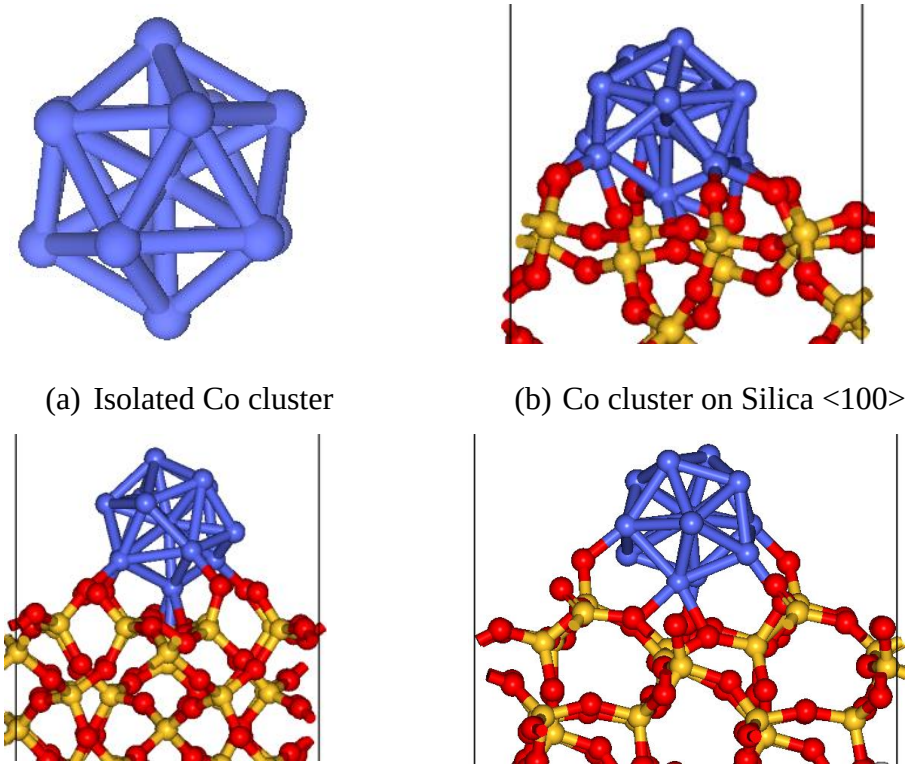

(a) Isolated Co cluster (b) Co cluster on Silica <100>

(c) Co cluster on Silica <110> (d) Co cluster on Silica <111>

Figure 6-6 Pictorial representation of unsupported and supported Co clusters. (a) Represents the isolated Co cluster. (b) Represents the geometrically relaxed Co cluster on the silica <100> surface. (c) Represents the geometrically relaxed Co cluster on silica <110> surface. (d) Represents the geometrically relaxed Co cluster on silica <111> surface

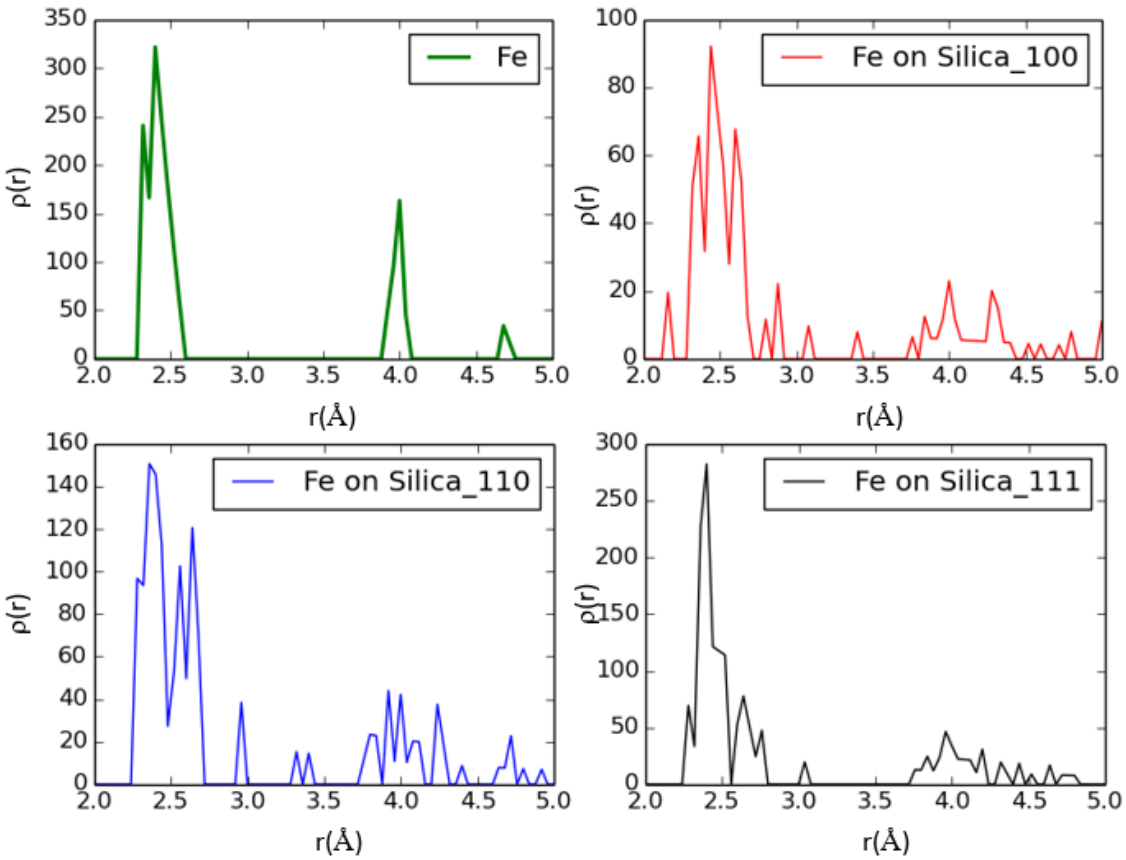

Figure 6-7: RDF of Fe-Fe bond distances on the Fe-clusters. The first graph (green legend) shows the RDF for the isolated Fe cluster, the second graph (red legend) shows the RDF for the Fe cluster on silica <100> surface. The third graph (blue legend) shows the RDF for the Fe cluster on silica <110 surfaces, and the fourth graph (black legend) corresponds to the RDF for the Fe cluster on silica<111> surface

Table 6-7 Mean bond length and standard deviation (σ) of bond length of the isolated iron cluster Vs iron cluster on the different planes of silica surface

Catalysts	Mean of the bond length (Å)	σ (Å)
Fe_{13}	2.36	0.01
Fe_{13} / Silica <100>	2.47	0.17
Fe_{13} / Silica <110>	2.49	0.29
Fe_{13} / Silica <111>	2.41	0.12

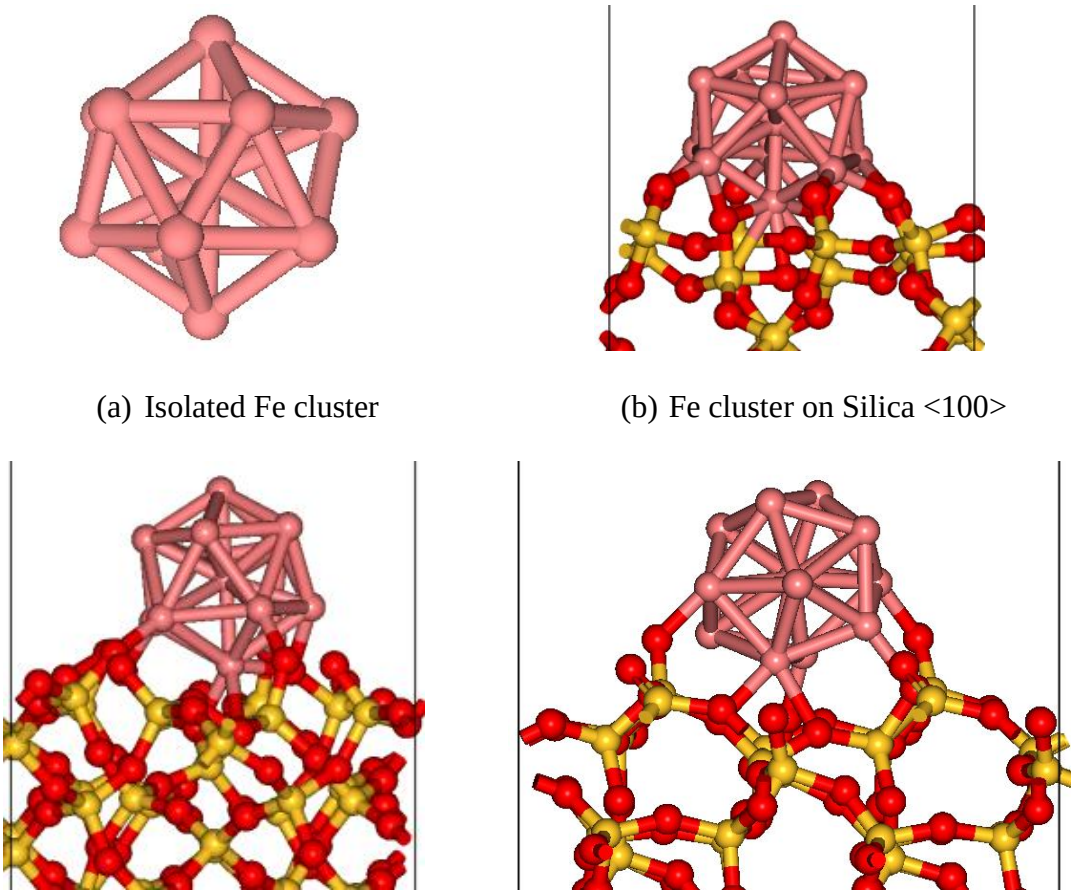

(a) Isolated Fe cluster

(b) Fe cluster on Silica <100>

(c) Fe cluster on Silica <110>

(d) Fe cluster on Silica <111>

Figure 6-8: Pictorial representation of unsupported and supported Fe clusters. (a) Represents the isolated Fe cluster. (b) Represents the geometrically relaxed Fe cluster on the silica <100> surface. (c) Represents the geometrically relaxed Fe cluster on silica <110> surface. (d) Represents the geometrically relaxed Fe cluster on silica <111> surface

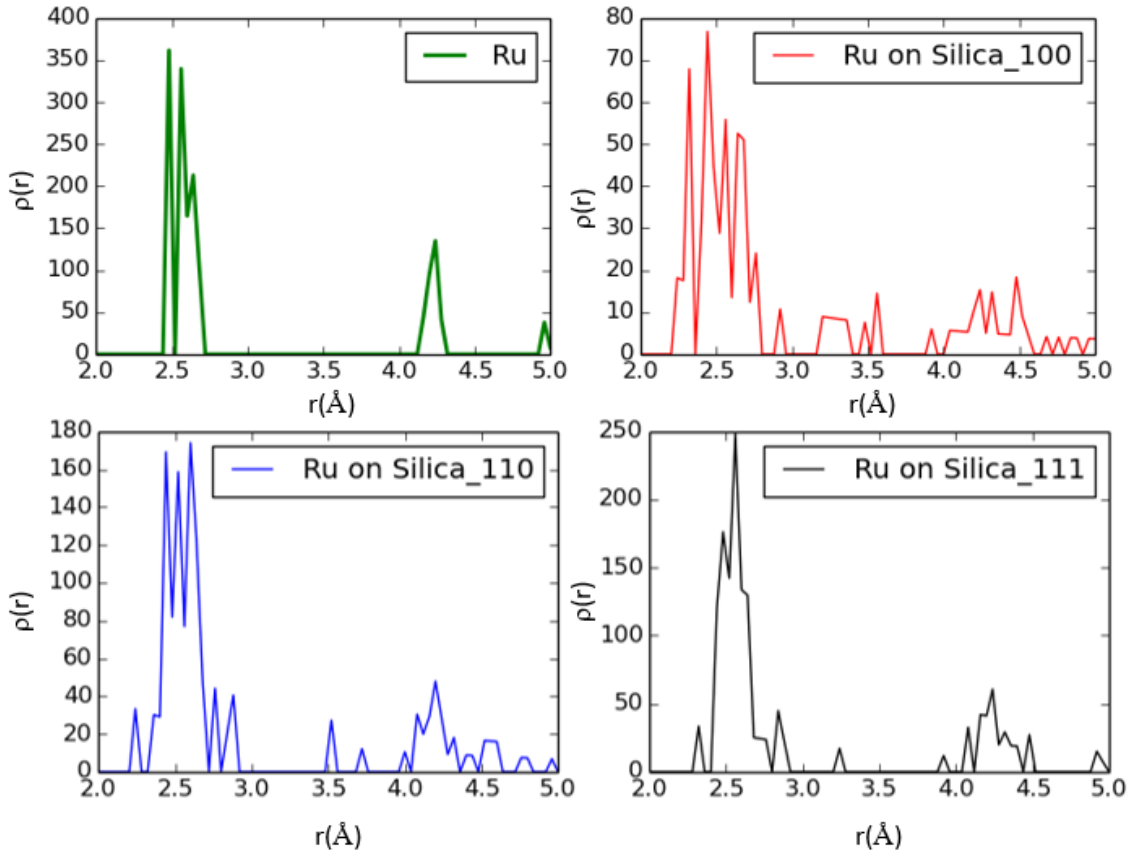

Figure 6-9: RDF of Ru-Ru bond distances on the Ru-clusters. The first graph (green legend) shows the RDF for the isolated Ru cluster, the second graph (red legend) shows the RDF for the Ru cluster on silica <100> surface. The third graph (blue legend) shows the RDF for the Ru cluster on silica <110 surfaces, and the fourth graph (black legend) corresponds to the RDF for the Ru cluster on silica <111> surface

Table 6-8: Mean bond length and standard deviation (σ) of bond length of the isolated ruthenium cluster Vs ruthenium cluster on the different planes of silica surface

Catalysts	Mean of the bond length (Å)	σ (Å)
Ru_{13}	2.50	0.00
Ru_{13} / Silica <100>	2.64	0.24
Ru_{13} / Silica <110>	2.53	0.09
Ru_{13} / Silica <111>	2.51	0.05

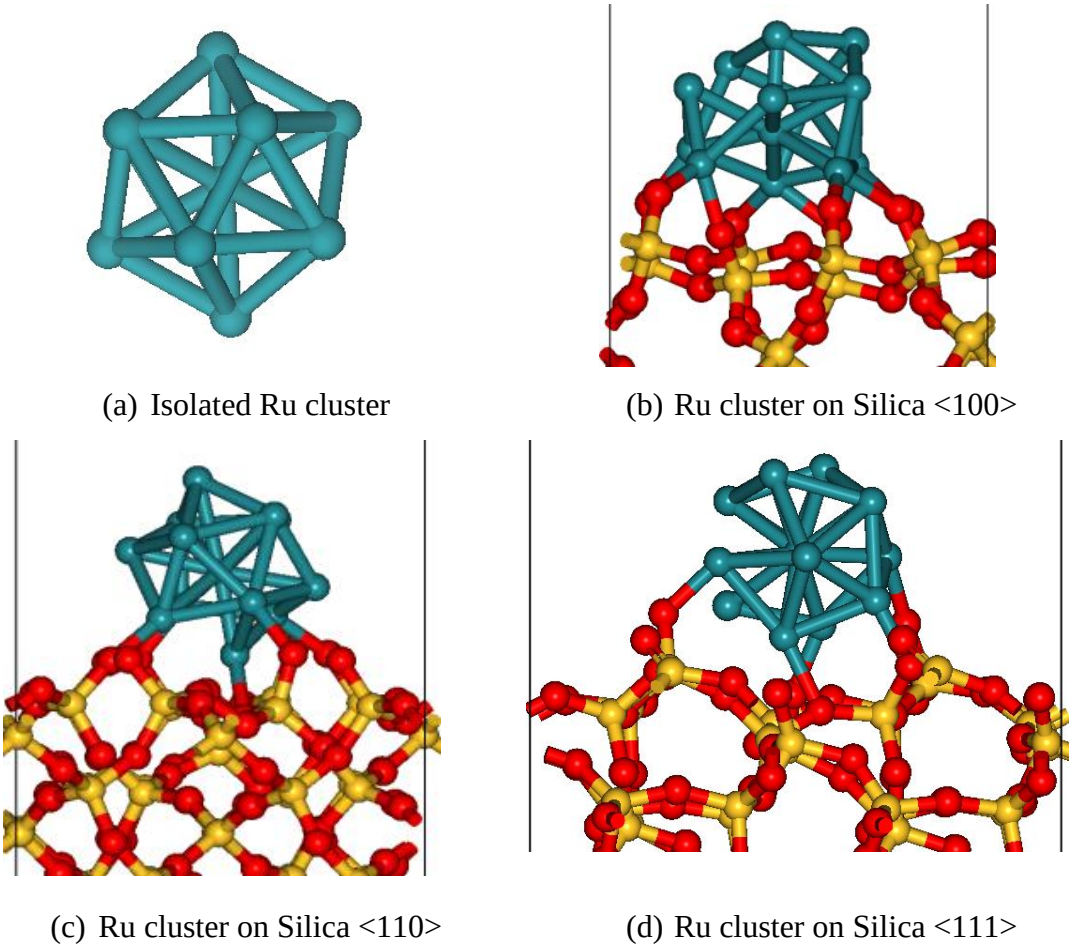

(a) Isolated Ru cluster (b) Ru cluster on Silica <100>

(c) Ru cluster on Silica <110> (d) Ru cluster on Silica <111>

Figure 6-10: Pictorial representation of Ru clusters. (a) Represents isolated Ru cluster. (b) Represents geometrically relaxed Ru cluster on silica <100> surface. (c) Represents geometrically relaxed Ru cluster on silica <110> surface. (d) Represents geometrically relaxed Ru cluster on silica <111> surface

6.4 Summary

The Fe cluster showed a strong interaction followed by the Ru and Co clusters with different silica planes. The presence of oxygen atoms at the surface of the support aided to the strong cluster support interaction. Fe, Ru, and Co have a tendency of forming metal oxides, and this has to be prevented as the formation of oxide reduces the FT catalytic activity by reducing the adsorption sites for CO adsorption. From the perspective of different silica surfaces, the silica <100> plane showed a strong interaction

to all the clusters. On the other hand, clusters on silica <100> showed higher distortions. Higher distortion (RDF and std) is an indication that the clusters are unstable, symmetry is broken, and could deform to other symmetries on the surface of the support. The most stable cluster in terms of structure is Ru on the silica <111> plane, followed by Ru cluster on the silica <110>. Co cluster on the silica <100> and Ru cluster on the silica <110> showed enhanced CO adsorption on the surface of the cluster. Moreover, the amount of charge transfer from the clusters to the surface of the support also indicates the possibility of strong reduction at the surface of the support. %Diff calculation for the Co, Fe, and Ru clusters on silica support indicate that these clusters do not have ability of breaking the CO bond on their surface.

CHAPTER 7

RESULT V - RUTILE SUPPORTED 13-ATOM CO, RU, AND FE CLUSTERS

Titanium dioxide (TiO_2) is a transition metal oxide which mainly occurs in four morphs. rutile, anatase, and brookite are the most popular ones. Rutile and anatase phases are the ones which are extensively used in industry in gas sensors, thin film capacitors, and photocatalysis applications [72]. Rutile has a tetragonal body-centered crystal structure with a $P4_2$ /mnm space group symmetry. The unit cell consists of six atoms in total. Comparison table of the rutile structural parameters between experimental and our theoretical calculations are shown in Table 7-1.

Table 7-1: Structural parameters such as lattice constants, bond lengths (Å), and bond angles of rutile at the GGA/PBE theory level. Experimental values are shown for comparison [72]

Rutile (exp)	Rutile (this work)
a=b=4.593 Å	a=b=4.696 Å
c = 2.958 Å	c = 2.987 Å
Ti-O-Ti = 98.79 º	Ti-O-Ti = 98.44 º
Ti-O = 1.98 Å	Ti-O = 1.97 Å

After obtaining the ground state of the unit cell of rutile at the GGA/PBE theory level, three supercells of p(3x2) for the rutile <100> plane, p(4x2) for the rutile <110> plane, and p(2x2) for the rutile <111> plane was created by cleaving the rutile surface

accordingly. A 30 Å vacuum slab was created like the silica slab in the previous chapter. Then the 13 atoms clusters based on Co, Fe, and Ru with icosahedron symmetry were placed at 3 Å above the surface of rutile for each surface terminated planes. Geometry optimizations were performed to find the ground state structures of the supported clusters. All the calculations performed to find the ground state structure of the supported clusters has been already mentioned in 6.1. Binding energy between the cluster and slab is computed according to **Eq. 6-1**.

7.1 Cluster Adsorption

Table 7-2 shows that the strength of the cluster interaction with rutile support is larger on the <100> surface than it is on the <111> and the <110> surfaces. The Ru cluster adsorbs strongly on the rutile <100> surface followed by the Co and Fe clusters. Similarly, on the rutile <110>, Ru cluster seems to bind strongly followed by the Fe and Co clusters. In the case of rutile <111> surface, the Co cluster shows stronger binding energy followed by the Ru and Fe clusters respectively.

Table 7-2: Binding energies of the clusters on different planes of rutile. All the reported energies are in eV

	Rutile<100>	Rutile<110>	Rutile<111>
Ru	-19.82	-6.81	-7.30
Co	-17.80	-5.22	-7.66
Fe	-16.53	-6.08	-7.20

It is very important to note that in fully relaxed rutile <100>, the oxygen atoms at the surface reconstruct and align horizontally (in-plane) with the Ti atoms at the surface. This behavior of oxygen atoms is very different compared to the bulk positions of the

oxygen atoms. Moreover, even after surface reconstruction of the oxygen atoms at the surface of the rutile <100>, the atoms succeed to make a double bond with the Ti atoms, and the Ti atoms at the surface make threefold occupancy with the oxygen atoms while at the bulk four-fold occupancy. In the rutile <110>, the oxygen atoms occupied the bridging position between two titanium atoms and surface reconstruction of the oxygen atoms was observed. At the surface, the Ti atoms occupy four-fold position with oxygen atoms and the oxygen atoms at the surface are slightly elevated (not in-plane with the Ti atoms). Mostly, the Ti atoms in the bulk region of the rutile <110> occupy the six-fold position with the oxygen atoms (Figure 7-1).

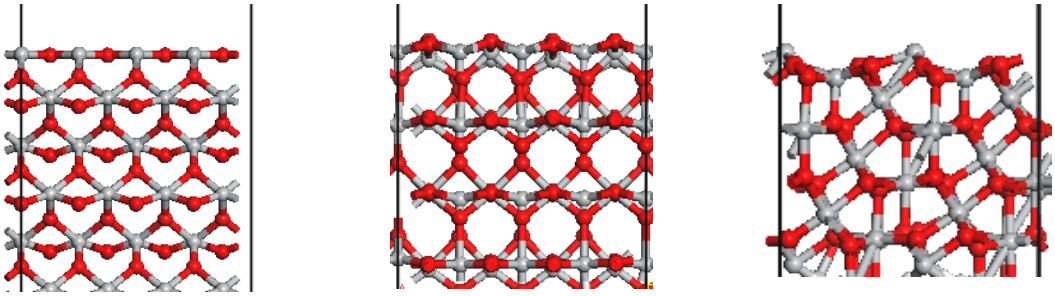

Rutile <100> Rutile <110> Rutile <111>

Figure 7-1: Side view of the geometry optimized structures of different rutile surfaces at GGA/PBE theory level (Silver: Ti, Red: O)

The layout of the oxygen and titanium atoms at the different rutile surfaces play an important role in the structural stability of the metal cluster when adsorbed on them. The metal atoms have a high tendency for oxidation; therefore, there is a high chance of structural deformation of the icosahedron symmetry of the metal clusters. Therefore, in this study, surfaces that will preserve the structural symmetry of the metal clusters with very less surface reconstruction of the atoms at the surface of the support during the binding of the metal clusters was subject of interest. In order to understand the interaction

behavior of different surfaces to metal clusters, a Bader charge analysis was performed. Calculations show that in the case of the rutile <100> surface, the charge is transferred from the surface of the support to the Co, Fe, and Ru clusters (Table 7-8). This behavior is very different from those for the rutile <110> and <111> surfaces where the charge is transferred from the clusters to the surface of the oxide support. Bader charge calculations show that for the Co cluster, 0.25 e of charge is transferred, 0.56 e of charge is transferred from the Fe cluster, and 0.07 e of charge is transferred from the Ru cluster to the rutile <110> surface. A similar trend is obtained for the rutile <111> surface with 0.52 e of charge transfer from the Co cluster, 0.27 e of charge transfer from the Fe cluster, and 0.41 e of charge transfer from the Ru cluster to the surface of rutile <111>. A study has confirmed that the interaction of transition metals on stoichiometric and reduced surfaces show different charge states on the transition metals [78]. Negative charge accumulation on the transition metal clusters has been observed with rutile <100> surface which could be because of a high degree of surface reconstruction upon the cluster binding. Similarly, negligible surface reconstruction on the rutile <110> and <111> surfaces are seen upon the binding of the metal clusters. Surface conditions, unsaturated bonds, defects, reconstruction, and surface orientations play an important role in the charge transfer phenomena as well as metal-support interaction. Depending on the different planes of TiO_2, the bonding strength of surface atoms (Ti and O) are also different. For instance, Ti-O bonding is relatively weaker on cleaved surfaces when compared to the bulk conditions. Additionally, the Ti-O bond strength in the rutile <001> surface is relatively weaker than that on the rutile <101> surface [79]. Weak bonds between the surface atoms of the surfaces tend to break easily and thus resulting in more

dangling bonds on the surface atoms which in turn results in the strong binding of clusters on the surface. Hence, metal particles on the surface do not disperse for a long time.

7.2 CO Adsorption and Its Bond Breaking

Table 7-3: CO adsorption on the rutile supported clusters on different adsorption sites and the energy required to break the adsorbed CO bond from the PAS

	Rutile<100>			Rutile<110>			Rutile<111>		
AS	Co	Fe	Ru	Co	Fe	Ru	Co	Fe	Ru
Top	-1.23	-1.22	-1.87	0.02	**-1.28**	-2.72	-1.40	-1.32	-0.51
Bridge	-1.66	-1.27	**-2.07**	**-2.39**	-1.23	-2.03	**-1.41**	-1.29	**-1.78**
Hollow	**-1.88**	**-1.39**	-2.01	-2.37	-1.25	**-3.85**	-1.35	**-1.61**	-1.70
E_{diss} (eV)	3.07	1.23	1.7	1.44	1.35	2.06	3.55	1.95	2.11

The CO adsorption energy calculation was carried out using **Eq. 2-17**. CO adsorption was carried out on the metal clusters that were supported by the rutile support. Three different adsorption sites were explored (top, bridge, and hollow). All the CO adsorption studies were carried out at the top section of the metal clusters. On rutile <100>, hollow site on Co cluster, hollow site on Fe cluster, and bridge site on Ru cluster are the PAS for CO adsorption. The adsorption energies with the PAS for CO adsorption on these clusters are highlighted in bold in the above table. Similarly, on rutile <110> surface, the PAS for CO adsorption on Co, Fe, and Ru clusters are bridge, top, and hollow sites respectively. Lastly, on rutile <111> surface, the PAS for CO adsorption on Co, Fe, and Ru clusters are bridge, hollow, and bridge sites respectively.

7.3 Binding Energy Ratio

In order to study the rutile supported cluster performance for CO adsorption, the BE ratio has been calculated using **Eq. 6-1**. The CO adsorption energy values for the PAS on the Co, Fe and Ru clusters on rutile <100> surface drops by 25%, 62%, and 17% respectively compared to those on their respective isolated clusters. Similarly, Fe cluster on rutile <110> surface shows degraded performance in adsorbing CO compared to its isolated clusters by 66%. The CO adsorption drops by approximately 5% on the PAS adsorption sites of the Co cluster on the rutile <110> surface. The Ru cluster on rutile <110> shows enhanced performance on adsorbing CO with the increment in the CO adsorption by 54%. But CO adsorption drops by 44% on the Co cluster, 57% on the Fe cluster, and 28% on the Ru cluster when they are supported on the rutile <111>. Like in the case of isolated metal clusters, the adsorption energy values of CO on the rutile supported metal clusters is the chemisorption of CO despite enhanced/diminished CO adsorption.

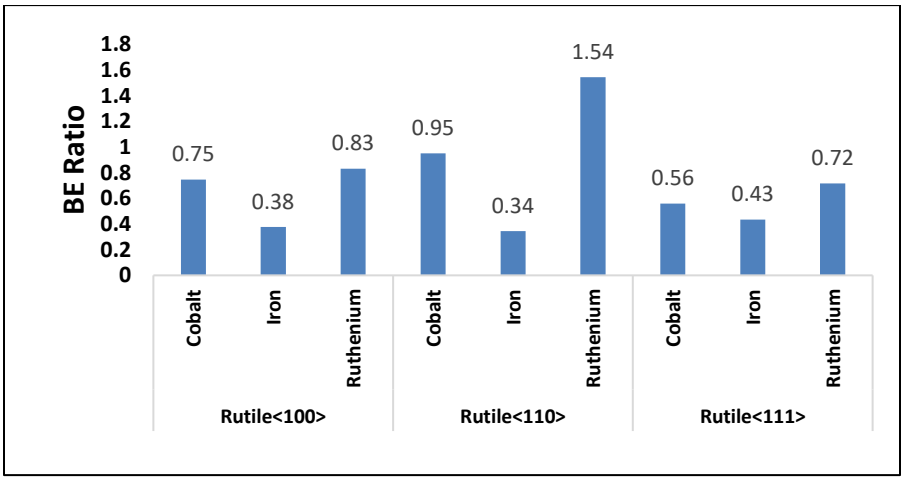

Figure 7-2: BE ratio of CO on isolated clusters Vs rutile supported clusters

7.4 Percentage Difference

In order to calculate the %Diff, it is necessary to calculate the energy required for splitting CO, which is calculated using **Eq. 2-16**. The calculated energy values for the CO bond breaking at the GGA/PBE theory level are shown in Table 7-3. In the table, E_{diss} represents the energy required to break the CO bond in eV. Similarly, the mathematical expression to calculate the %Diff is mentioned in **Eq. 2-17.** The GGA/PBE theory predicts that the Ru cluster supported on rutile <110> is the most effective catalyst with the highest %Diff of 60%. This is followed by the Co cluster supported on rutile <110> with the %Diff of 40 %. Fe and Ru clusters supported on rutile <100> also show good catalytic activity with the %Diff of 12 % and 20 % respectively. All the other clusters on the different rutile surfaces do not show any tendency to proceed with the surface carbide mechanism for the FT process. The calculated values of %Diff are shown in Figure 7-3.

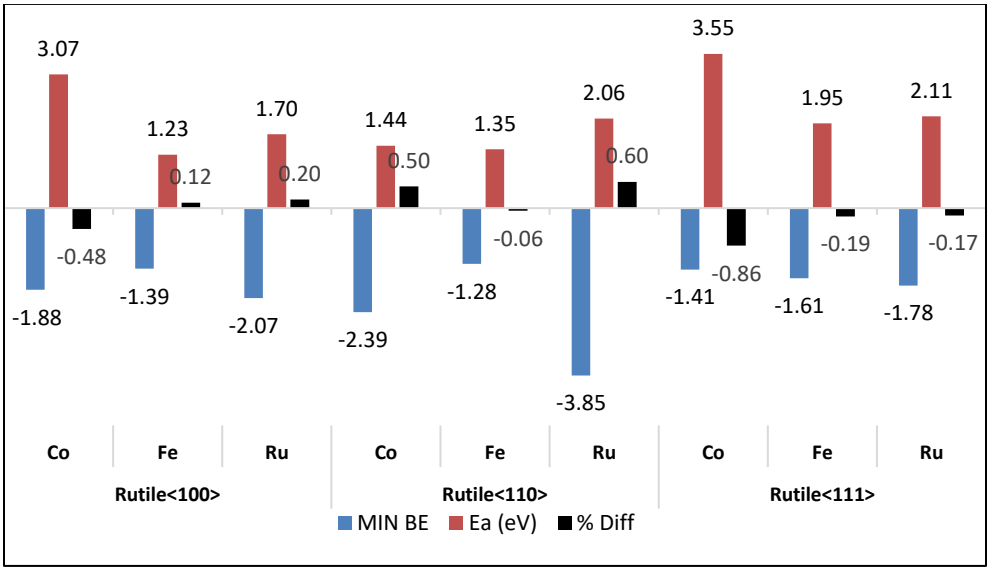

Figure 7-3: CO adsorption energy (eV) on each rutile supported cluster with PAS (MIN BE), E^{diss} (eV) the energy required to break the CO bond on the surface of the clusters, and the percentage difference (%Diff)

Table 7-4: CO bond length in Å obtained after the relaxations of the structures at the GGA/PBE theory level

	Rutile <100>			Rutile <110>			Rutile <111>			Isolated Cluster		
	Co	Fe	Ru	Co	Fe	Ru	Co	Fe	Ru	Co	Fe	Ru
Top	1.14	1.16	1.17	0	1.17	1.18	1.17	1.18	1.11	1.18	1.17	1.18
Bridge	1.20	1.20	1.19	1.21	1.20	1.20	1.20	1.20	1.20	1.20	1.19	1.20
Hollow	1.21	1.21	1.21	1.20	1.21	1.19	1.21	1.22	1.20	1.21	1.22	1.20

7.5 Structural Stability of Clusters on Surfaces

In order to study the stability of the clusters on the rutile support, the Radial Distribution Functions (RDF) of the metal-metal bonds in the clusters was generated. When the clusters are placed on the top of the different rutile surfaces, surface terminated with the <100>, <110>, and <111> planes, the mean of the metal-metal bond distances between the center atom and surface atoms changes. Distortion in the metal-metal bond distances can be seen with the RDF in Figure 7-4. The calculated values of the mean and the standard deviation (std) of the bond length of the Co, Fe, and Ru clusters on different planes of the rutile support is reported in Table 7-5, 7-6, and 7-7.

From the RDF for the Co-Co bond distance, the Co cluster is highly stable when supported on the rutile <100> followed by rutile <110> when compared with that of the ground state geometry of isolated Co cluster. The Co cluster can retain its icosahedron symmetry on rutile <100> and rutile <110>, but the symmetry is broken when the cluster is on the rutile <111> surface. Meanwhile, on rutile <111>, the Co-Co mean distance between the center atom and the surface atoms also increases by 0.1 Å when compared with that of the isolated Co cluster, yielding the highest standard deviation of 0.09 Å.

The Fe cluster, on the other hand, shows less distortion compared to the Co cluster. The mean of the Fe-Fe bond distance between the center atom and surface atoms increases by 0.12 Å on rutile <100>, 0.10 Å on rutile <110> surface and 0.11 Å on rutile <111> respectively when compared with that of the ground state geometry of isolated Fe cluster. The calculated standard deviation shows a big deviance in the Fe-Fe bond length when the cluster is on rutile <100> (σ = 0.08 Å), and the least deviance is seen when the cluster is on the surface of rutile <111> (σ = 0.05 Å). It is also very important to note that the Fe cluster retains its symmetry regardless of the rutile surfaces. In the case of the Ru cluster, the cluster exhibits a higher distortion when placed on rutile <110> surface where the mean shifts by 0.29 Å compared to that of the isolated Ru cluster, yielding the highest standard deviation of σ = 0.12 Å. The structural symmetry also changes on this surface, but the symmetry does not change much on rutile <100> and rutile <111> surface for the Ru cluster.

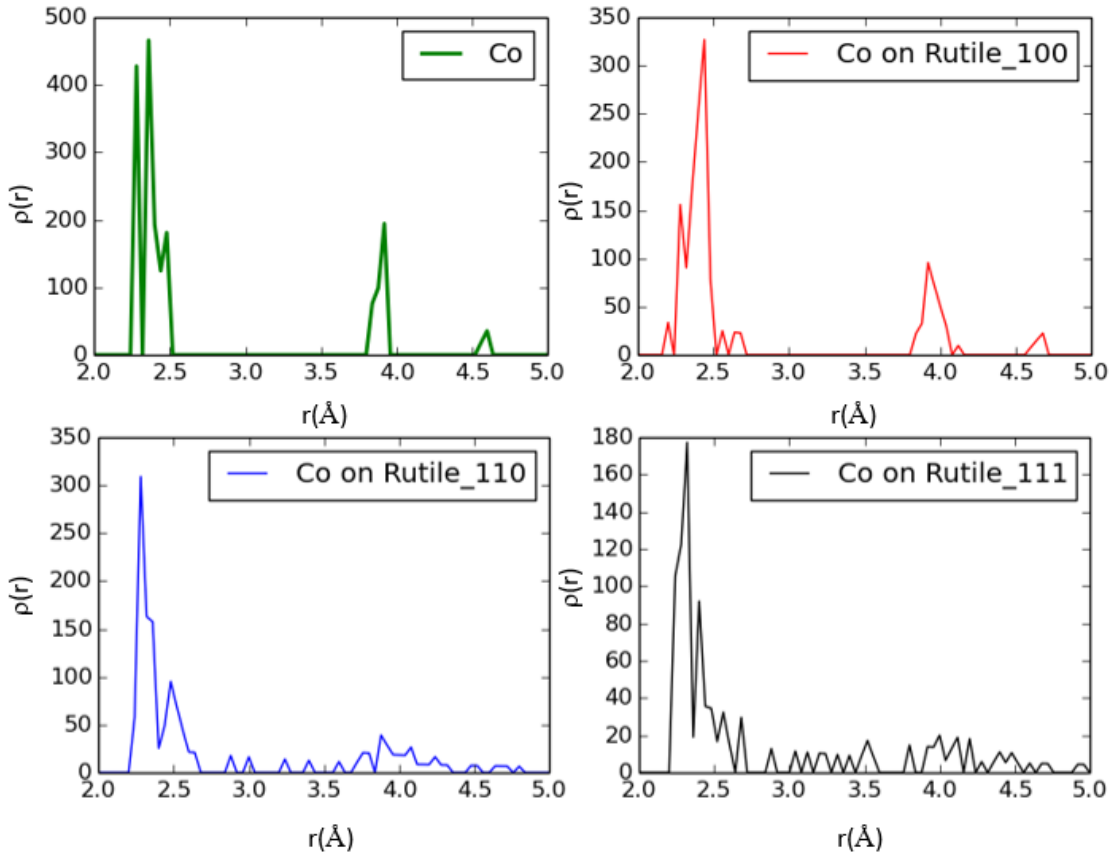

Figure 7-4: RDF of Co clusters. The first graph (green legend) shows the RDF of an isolated Co cluster, the second graph (red legend) shows the RDF of Co cluster on a rutile <100> surface. The third graph (blue legend) shows the RDF of Co cluster on a rutile<110 surface, and the fourth graph (black legend) corresponds to the RDF of Co cluster on a rutile <111> surface

Table 7-5: Mean bond length and standard deviation (σ) of bond length of the isolated cobalt cluster Vs cobalt cluster on the different planes of rutile surface

Catalysts	Mean of the bond length (Å)	σ (Å)
Co_{13}	2.30	0.01
Co_{13} / Rutile <100>	2.42	0.05
Co_{13} / Rutile <110>	2.35	0.08
Co_{13} / Rutile <111>	2.40	0.09

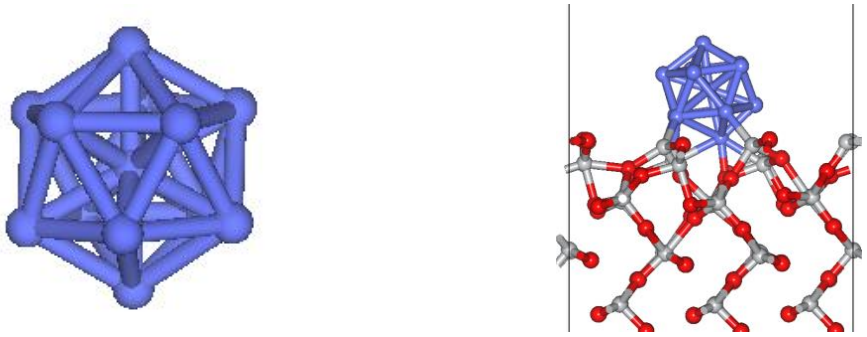

(a) Isolated Co cluster

(b) Co cluster on Rutile<100>

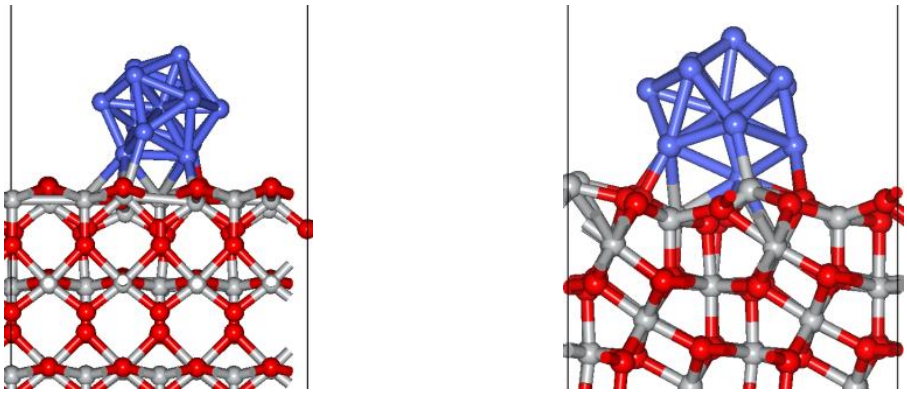

(c) Co cluster on Rutile<110>

(d) Co cluster on Rutile<111>

Figure 7-5: Pictorial representation of Co clusters. (a) Represents isolated Co cluster. (b) Represents geometrically relaxed Co cluster on rutile <100> surface. (c) Represents geometrically relaxed Co cluster on rutile <110> surface. (d) Represents geometrically relaxed Co cluster on rutile <111> surface

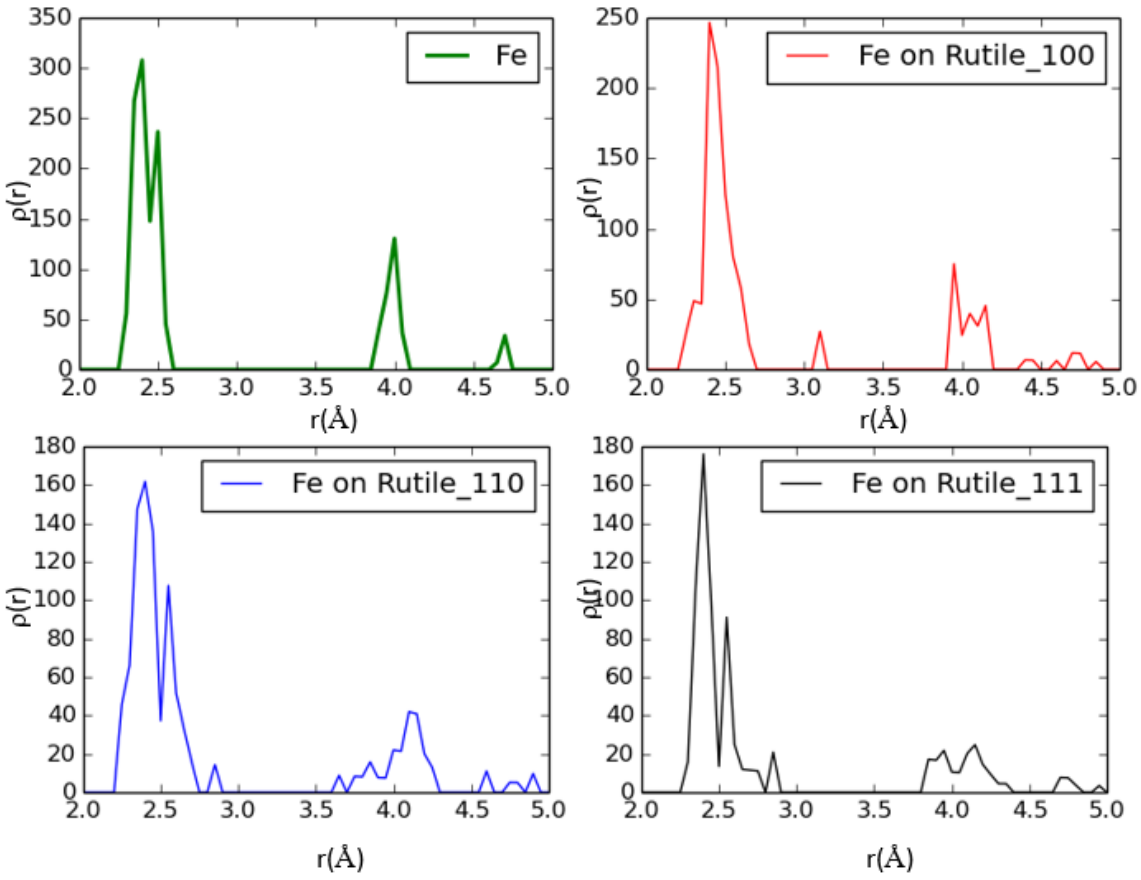

Figure 7-6: RDF of Fe clusters. The first graph (green legend) shows the RDF of an isolated Fe cluster, the second graph (red legend) shows the RDF of Fe cluster on a rutile <100> surface. The third graph (blue legend) shows the RDF of Fe cluster on a rutile <110> surface, and the fourth graph (black legend) corresponds to the RDF of Fe cluster on a rutile <111> surface

Table 7-6: Mean bond length and standard deviation (σ) of bond length of the isolated iron cluster Vs iron cluster on the different planes of rutile surface

Catalysts	Mean of the bond length (Å)	σ (Å)
Fe_{13}	2.30	0.01
Fe_{13} / Rutile <100>	2.42	0.08
Fe_{13} / Rutile <110>	2.40	0.07
Fe_{13} / Rutile <111>	2.41	0.05

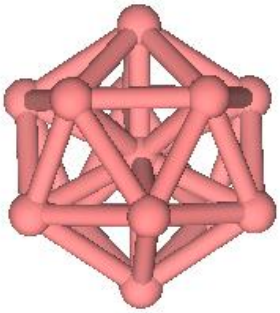

(a) Isolated Fe cluster

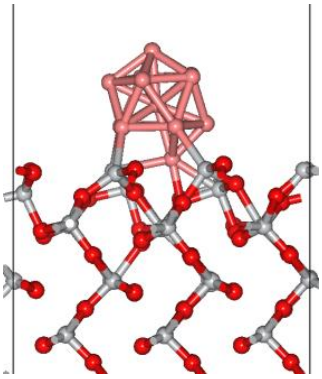

(b) Fe cluster on Rutile<100>

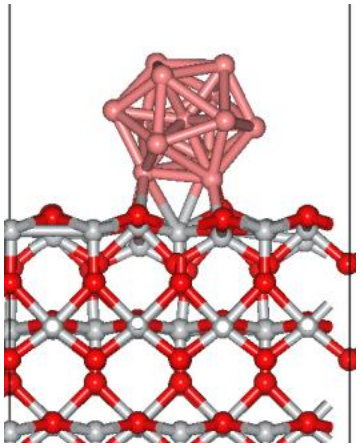

(c) Fe cluster on Rutile<110>

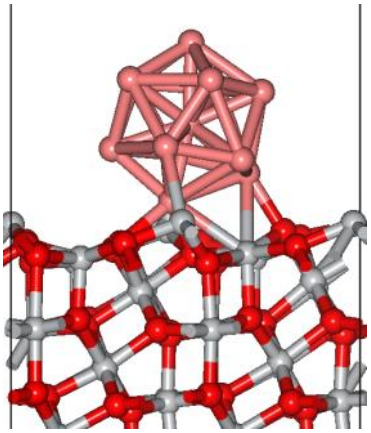

(d) Fe cluster on Rutile<111>

Figure 7-7: Pictorial representation of Fe clusters. (a) Represents isolated Fe cluster. (b) Represents geometrically relaxed Fe cluster on rutile <100> surface. (c) Represents geometrically relaxed Fe cluster on rutile <110> surface. (d) Represents geometrically relaxed Fe cluster on rutile <111> surface

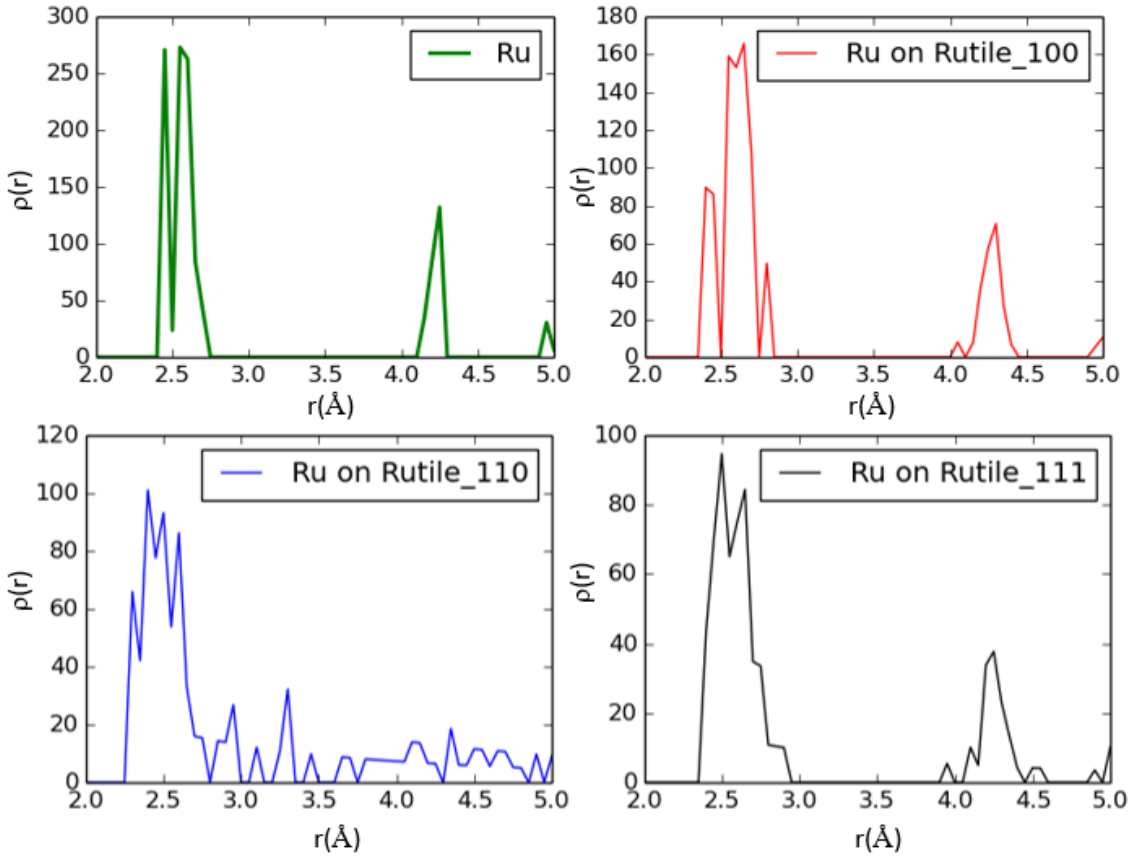

Figure 7-8: RDF of Ru clusters. The first graph (green legend) shows the RDF of an isolated Ru cluster, the second graph (red legend) shows the RDF of Ru cluster on a rutile <100> surface. The third graph (blue legend) shows the RDF of Ru cluster on a rutile <110 surface, and the fourth graph (black legend) corresponds to the RDF of Ru cluster on a rutile <111> surface

Table 7-7: Mean bond length and standard deviation (σ) of bond length of the isolated ruthenium cluster Vs ruthenium cluster on the different planes of rutile surface

Catalysts	Mean of the bond length (Å)	σ (Å)
Ru_{13}	2.30	0.01
Ru_{13} / Rutile <100>	2.42	0.09
Ru_{13} / Rutile <110>	2.59	0.12
Ru_{13} / Rutile <111>	2.52	0.10

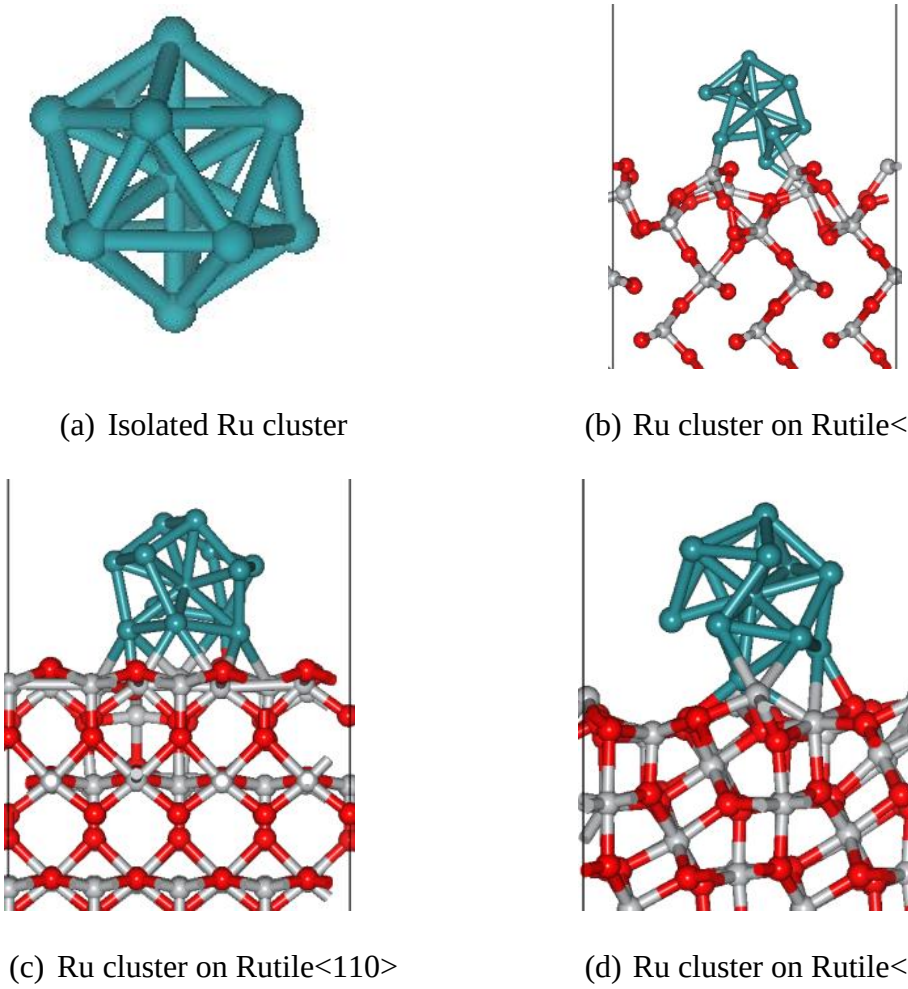

(a) Isolated Ru cluster (b) Ru cluster on Rutile<100>

(c) Ru cluster on Rutile<110> (d) Ru cluster on Rutile<111>

Figure 7-9: Pictorial representation of Ru clusters. (a) Represents isolated Ru cluster. (b) Represents geometrically relaxed Ru cluster on rutile <100> surface. (c) Represents geometrically relaxed Ru cluster on rutile <110> surface. (d) Represents geometrically relaxed Ru cluster on rutile <111> surface

7.6 Summary

Based on the Bader charge and RDF analysis, we have found that the rutile <110> surface exhibits better performance in retaining the structural symmetry of the nanoclusters and in adsorption of CO for further hydrogenation reactions. The transfer of charges from the surfaces to the nanoclusters as revealed by the rutile <100> surface could be useful for the CO oxidation catalytic reaction. Similarly, the BE ratio has been calculated to see the effect of the support that could either enhance or degrade the CO

adsorption on the clusters. Although CO adsorption energies have been affected with the presence of the support, Ru cluster on rutile <110> shows enhanced performance among all the cases that were studied and is followed by Ru on rutile <100> and rutile <111> surfaces. On the other hand, Fe cluster shows the worst performance in CO adsorption regardless of the support surfaces when compared to Co and Ru clusters. From the perspective of the %Diff study, Ru and Co clusters on rutile <110> show effective catalytic activity in breaking the CO bond on the surface of the cluster which facilitates surface carbide mechanism.

From Table 7-8, cobalt and ruthenium clusters on rutile <110> show the best performance among all the other surfaces with the percentage difference of 50% and 60%. This is followed by the iron and ruthenium clusters on the surface of the rutile <100> surface with the percentage difference of 12% and 20%. On the hand, the binding of clusters on rutile <100> surface is also stronger than other rutile surfaces. The strong binding energy of the clusters indicates that the agglomeration of the clusters on the surface will be minimum. Although silica surfaces show strong binding of the clusters on their surfaces, %Diff indicates that the CO bond breaking on the clusters supported with silica is not likely. Similarly, Bader charge analysis shows that there is a possibility of the reduction at the surface of the silica support. Hence, this study suggests rutile support is preferable than the silica support for the clusters as FT catalyst.

Table 7-8: Comparison table between supports (different surface planes of rutile and silica). BE (eV) represents the binding energy of the clusters (pure 13 atom Co, Fe, and Ru) on the support, E_{ads} represents the adsorption of CO on the PAS of the supported clusters, E_{diss} represents the energy required to break the CO bond, %Diff represents percentage difference, BE-R is binding energy ration, and Bader represents Bader charge

Support	Catalyst	BE (eV)	E_{ads} (eV) (PAS)	E_{diss}(eV)	%Diff	BE-R	Bader (e)
Rutile <100>	Co_{13}	-17.80	-1.88 (Hollow)	3.07	-48	0.75	-1.01
	Fe_{13}	-16.53	-1.39 (Hollow)	1.23	**12**	0.38	-0.46
	Ru_{13}	-19.82	-2.07 (Bridge)	1.70	**20**	0.83	-0.32
Rutile <110>	**Co_{13}**	-5.22	-2.39 (Bridge)	1.44	**50**	0.95	0.25
	Fe_{13}	-6.08	-1.28 (Top)	1.35	-6	0.34	0.56
	Ru_{13}	-6.81	-3.85 (Hollow)	2.06	**60**	1.54	0.07
Rutile <111>	Co_{13}	-7.66	-1.41 (Bridge)	3.55	-86	0.56	0.52
	Fe_{13}	-7.20	-1.61 (Hollow)	1.95	-19	0.43	0.27
	Ru_{13}	-7.30	-1.78 (Bridge)	2.11	-17	0.72	0.41
Silica <100>	Co_{13}	-22.61	-2.97 (Bridge)	3.14	-6	1.20	3.91
	Fe_{13}	-25.26	-1.33 (Hollow)	2.66	-67	0.57	4.69
	Ru_{13}	-23.46	-2.46 (Hollow)	2.62	-6	0.96	3.94
Silica <110>	Co_{13}	-15.85	-1.49 (Hollow)	3.11	-70	0.60	2.80
	Fe_{13}	-21.54	-2.34 (Hollow)	3.15	-30	1.00	3.95
	Ru_{13}	-16.03	-2.79 (Top)	-3.00	-7	1.09	3.39
Silica <111>	Co_{13}	-19.36	-1.97 (Hollow)	3.18	-47	0.79	2.98
	Fe_{13}	-20.62	-1.89 (Hollow)	3.46	-59	0.81	3.47
	Ru_{13}	-20.22	-2.35 (Hollow)	2.59	-10	0.92	3.27

CHAPTER 8

CONCLUSION AND FUTURE WORK

8.1 Conclusions

In this research, DFT was used to study CO adsorption and its bond breaking on isolated clusters (14 atoms and magic-sized clusters) and some selected clusters with supports such as silica and rutile. The isolated clusters correspond to the pure and binary combinations of known catalysts for FT synthesis (Co, Fe, Ni, and Ru). The overall goal of this research was to identify the best catalysts for FT application based on the surface carbide reaction mechanism.

8.2 Cluster without Support

From the CO adsorption and its bond breaking energies on the pure clusters, the material with the potential to exhibit greater catalytic activity was predicted by looking at the cases for which %Diff is increased. For the pure magic sized clusters (stable clusters), the ones with the highest to lowest %Diff were Ru, Co, Ni, and Fe clusters, which is consistent with the current state of knowledge of material that have FT activity [60]. This suggested that the %Diff is a good predictor of a catalyst performance and was used to predict the binary cluster systems. It was found that CoFe system, cluster with 10 Co atoms at the shell and 4 Fe atoms at the core, has a potential for FT catalyst.

%Diff can be maximized with stronger CO adsorption and lower CO dissociation energy; therefore, information from the CO adsorption and dissociation energy on the

cluster can be used to design a system with greater catalytic activity. CO adsorption study for the pure cases of 14 atoms clusters (unstable system) suggested that Fe_{14} cluster showed the stronger CO adsorption compared to Co_{14} cluster. However, bimetallic clusters comprised of 14 atoms (CoFe and FeCo) showed stronger CO adsorption when compared to the pure Co_{14} and Fe_{14} clusters. In the FeCo system, two PAS for the CO molecule were identified; the top site, on top of Fe atom, and the hollow site, between two Fe atoms and a Co atom. The CO adsorption energy corresponds that the hollow site is much stronger than the top site. Similarly, in the CoFe system, the CO adsorption energies were found to be the strongest among all the 14 atom clusters. Two PAS identified for CoFe were the hollow and top sites. Top site (on top of a Fe atom) was identified to have stronger CO adsorption than the hollow site (between three Co atoms). Therefore, this study suggests that the involvement of a Fe atom could aid in enhancing the CO adsorption in an unstable system. But this does not hold true for the 13 atoms pure Co and Fe clusters which were identified as the stable system from the second energy difference study. CO adsorption study showed that Co_{13} cluster has stronger interaction to the CO molecule than the Fe_{13} cluster.

Similarly, CO dissociation study on the 14 atoms clusters suggests that the pure Co_{14} cluster has lower CO dissociation energy than the Fe_{14} cluster. CO dissociation energy for the CoFe and the FeCo systems are lower than the CO dissociation energy for the pure Fe_{14} cluster and higher than the pure Co_{14} cluster. CoFe with %Diff of 35%, which consists of 10 Co atoms at the shell and 4 Fe atoms at the core, showed the potential of breaking the CO bond. The %Diff calculation for the FeCo (-15%), which consists of 10 Fe atoms at the shell and 4 Co atoms at the core, showed increased

performance compared to the pure Co_{14} (-24%) and Fe_{14} (-46%) clusters. This also holds true for the stable clusters with 13 atoms. CO dissociation energy on the Co_{13} cluster is lower than the Fe_{13} cluster. Similarly, for the 13 atom bimetallic system, Co_1Fe_{12} cluster, introduction of a Co atom in the cluster lowered the CO dissociation energy of the pure Fe_{13} cluster from 2.29 eV to 1.42 eV. In Co_1Ni_{12} cluster, substitution of Co atom in Ni_{13} cluster also aided in lowering the CO dissociation energy from 2.47 eV to 1.8 eV. Hence, it can be concluded that a Co atom contribute to lower the CO dissociation energy. Therefore, a system with higher concentration of Co atoms and lower concentration of Fe such as CoFe or a right composition of 3-d transition metals (Co, Ni, and Fe) could be the best catalyst for the FT application.

8.3 Effect of Supports

CO adsorption is a key step in FT reaction mechanism. CO adsorption study on 13 atom (Co, Fe, and Ru) clusters accompanied by support such as silica and rutile on different planes (<100>, <110>, and <111>) showed that these clusters have potential for adsorbing CO. Binding energy of the clusters on different planes of silica support showed strong adsorption of the clusters compared to the rutile support. Bader charge analysis revealed that significant amount of charge was transferred from the clusters to the silica surfaces compared to the rutile surfaces. This indicates that the strong reduction on the surfaces of the silica support is possible which results in the decrease in catalytic activity. On the other hand, clusters were structurally distorted more on the silica support compared to the rutile support except for the Ru cluster on <110> and <111>. % Diff calculation showed that none of the clusters on different planes of silica support had a tendency of breaking CO bond on the surface of the clusters. Hence, rutile <110> support

with the Ru and Co clusters and rutile <100> support with Ru and Fe clusters were identified as the best clusters with support for FT catalytic activity. Furthermore, in terms of less distortion and strong binding energy of the cluster, Ru and Fe clusters on rutile <100> surface was identified as the best catalysts for FT application compared to Ru and Co clusters on rutile <110> support.

8.4 Future Work

- CO adsorption along with hydrogen adsorption is the preliminary step in surface carbide mechanism. Hence, CO adsorption and dissociation accompanied by hydrogen on the clusters can be studied to elucidate the reaction kinetics of CO bond breaking.
- Pure and alloyed clusters of bigger sizes (size > 1 nm) made up of cobalt, iron, and ruthenium can be studied for realistic models. Generally, cluster sizes of 13 atoms, 55 atoms, and 147 atoms are found to be geometrically stable structures [80].
- In order to determine the potential of catalysts towards some reaction, it is very important to study the complex issues in catalysis which are selectivity, poisoning, activity, and surface reconstruction. Sulfide plays a crucial role in poising the catalysts in FT reaction [81]. It binds to the adsorption sites of the catalysts, thus reducing the surface reaction area which hinders the reaction rate of the reaction. Hence, sulfide adsorption can be studied on the surface of the proposed catalysts to examine its chemistry with the element.
- The nanoclusters can also be accompanied with supports like Alumina and Graphene to see the effect of these supports in the reaction [82].

BIBLIOGRAPHY

[1] A. Y. Khodakov, W. Chu, and P. Fongarland, "Advances in the Development of Novel Cobalt Fischer−Tropsch Catalysts for Synthesis of Long-Chain Hydrocarbons and Clean Fuels," *Chem. Rev.*, vol. 107, no. 5, pp. 1692–1744, May 2007.

[2] J.-X. Liu, P. Wang, W. Xu, and E. J. M. Hensen, "Particle Size and Crystal Phase Effects in Fischer-Tropsch Catalysts," *Engineering*, vol. 3, no. 4, pp. 467–476, Aug. 2017.

[3] J. Hu, F. Yu, and Y. Lu, "Application of Fischer–Tropsch Synthesis in Biomass to Liquid Conversion," *Catalysts*, vol. 2, no. 2, pp. 303–326, Jun. 2012.

[4] H. Schulz, "Short history and present trends of Fischer–Tropsch synthesis," *Appl. Catal. Gen.*, vol. 186, no. 1, pp. 3–12, Oct. 1999.

[5] V. D. J. Loosdrecht and J. W. Niemantsverdriet, "Synthesis gas to hydrogen, methanol, and synthetic fuels," *Chem. Energy Storage*, pp. 443–458, 2012.

[6] S. Li, S. Krishnamoorthy, A. Li, G. D. Meitzner, and E. Iglesia, "Promoted Iron-Based Catalysts for the Fischer–Tropsch Synthesis: Design, Synthesis, Site Densities, and Catalytic Properties," *J. Catal.*, vol. 206, no. 2, pp. 202–217, Mar. 2002.

[7] C.-F. Huo, Y.-W. Li, J. Wang, and H. Jiao, "Insight into CH4 Formation in Iron-Catalyzed Fischer−Tropsch Synthesis," *J. Am. Chem. Soc.*, vol. 131, no. 41, pp. 14713–14721, Oct. 2009.

[8] D. Leckel, "Diesel Production from Fischer−Tropsch: The Past, the Present, and New Concepts," *Energy Fuels*, vol. 23, no. 5, pp. 2342–2358, May 2009.

[9] R. Luque, A. R. de la Osa, J. Manuel Campelo, A. Angel Romero, J. Luis Valverde, and P. Sanchez, "Design and development of catalysts for Biomass-To-Liquid-Fischer–Tropsch (BTL-FT) processes for biofuels production," *Energy Environ. Sci.*, vol. 5, no. 1, pp. 5186–5202, 2012.

[10] S. N. Rashkeev and M. V. Glazoff, "Fischer–Tropsch Synthesis over Supported Pt–Mo Catalyst: Toward Bimetallic Catalyst Optimization," *J. Phys. Chem. C*, vol. 117, no. 9, pp. 4450–4458, Mar. 2013.

[11] M. Zhuo, K. F. Tan, A. Borgna, and M. Saeys, “Density Functional Theory Study of the CO Insertion Mechanism for Fischer−Tropsch Synthesis over Co Catalysts,” *J. Phys. Chem. C*, vol. 113, no. 19, pp. 8357–8365, May 2009.

[12] O. R. Inderwildi, S. J. Jenkins, and D. A. King, “Fischer−Tropsch Mechanism Revisited: Alternative Pathways for the Production of Higher Hydrocarbons from Synthesis Gas,” *J. Phys. Chem. C*, vol. 112, no. 5, pp. 1305–1307, Feb. 2008.

[13] T. N. Veziroğlu and S. Şahiin, “21st Century’s energy: Hydrogen energy system,” *Energy Convers. Manag.*, vol. 49, no. 7, pp. 1820–1831, Jul. 2008.

[14] Z.-P. Liu and P. Hu, “General Rules for Predicting Where a Catalytic Reaction Should Occur on Metal Surfaces: A Density Functional Theory Study of C−H and C−O Bond Breaking/Making on Flat, Stepped, and Kinked Metal Surfaces,” *J. Am. Chem. Soc.*, vol. 125, no. 7, pp. 1958–1967, Feb. 2003.

[15] Z.-P. Liu and P. Hu, “General trends in CO dissociation on transition metal surfaces,” *J. Chem. Phys.*, vol. 114, no. 19, pp. 8244–8247, May 2001.

[16] D. B. Bukur, D. Mukesh, and S. A. Patel, “Promoter effects on precipitated iron catalysts for Fischer-Tropsch synthesis,” *Ind. Eng. Chem. Res.*, vol. 29, no. 2, pp. 194–204, Feb. 1990.

[17] E. Iglesia, S. L. Soled, R. A. Fiato, and G. H. Via, “Bimetallic Synergy in Cobalt Ruthenium Fischer-Tropsch Synthesis Catalysts,” *J. Catal.*, vol. 143, no. 2, pp. 345–368, Oct. 1993.

[18] V. Roberto Calderone, N. Raveendran Shiju, D. Curulla Ferré, and G. Rothenberg, “Bimetallic catalysts for the Fischer–Tropsch reaction,” *Green Chem.*, vol. 13, no. 8, pp. 1950–1959, 2011.

[19] J. J. Spivey and A. Egbebi, “Heterogeneous catalytic synthesis of ethanol from biomass-derived syngas,” *Chem. Soc. Rev.*, vol. 36, no. 9, pp. 1514–1528, Jul. 2007.

[20] “Accelrys. Materials Studio, 6.0 ed., Accelrys Software, Inc., San Diego, CA, USA, 2010.”

[21] G. Kresse and J. Hafner, “Ab initio molecular-dynamics simulation of the liquid-metal--amorphous-semiconductor transition in germanium,” *Phys. Rev. B*, vol. 49, no. 20, pp. 14251–14269, May 1994.

[22] G. Kresse and J. Furthmüller, “Efficient iterative schemes for ab initio total-energy calculations using a plane-wave basis set,” *Phys. Rev. B*, vol. 54, no. 16, pp. 11169–11186, Oct. 1996.

[23] J. Hafner, “Materials simulations using VASP—a quantum perspective to materials science,” *Comput. Phys. Commun.*, vol. 177, no. 1, pp. 6–13, Jul. 2007.

[24] I. N. Levine, *Quantum Chemistry*, Third ed., Allyn and Bacon, Inc, 1983.

[25] M. D. Segall, P.J.D. Lindan, M.J. Probert, C.J. Pickard, P.J. Hasnip, S.J. Clark, and M.C. Payne, “First-principles simulation: ideas, illustrations and the CASTEP code,” *J. Phys. Condens. Matter*, vol. 14, no. 11, p. 2717, 2002.

[26] L. S. Cederbaum, “Born–Oppenheimer approximation and beyond for time-dependent electronic processes,” *J. Chem. Phys.*, vol. 128, no. 12, p. 124101, Mar. 2008.

[27] P. Hohenberg and W. Kohn, “Inhomogeneous Electron Gas,” *Phys. Rev.*, vol. 136, no. 3B, pp. B864–B871, Nov. 1964.

[28] W. Kohn and L. J. Sham, “Self-Consistent Equations Including Exchange and Correlation Effects,” *Phys. Rev.*, vol. 140, no. 4A, pp. A1133–A1138, Nov. 1965.

[29] R. G. Parr and W. Yang, *Density-Functional Theory of Atoms and Molecules*, Oxford University Press, USA, 1994.

[30] W. Kohn, A. D. Becke, and R. G. Parr, “Density Functional Theory of Electronic Structure,” *J. Phys. Chem.*, vol. 100, no. 31, pp. 12974–12980, Jan. 1996.

[31] E. G. Lewars, *Computational Chemistry: Introduction to the Theory and Applications of Molecular and Quantum Mechanics*, Second ed., Springer, 2011.

[32] S. Kurth and J. P. Perdew, “Role of the exchange–correlation energy: Nature’s glue,” *Int. J. Quantum Chem.*, vol. 77, no. 5, pp. 814–818.

[33] N. Mardirossian and M. Head-Gordon, “Thirty years of density functional theory in computational chemistry: an overview and extensive assessment of 200 density functionals,” *Mol. Phys.*, vol. 115, no. 19, pp. 2315–2372, Oct. 2017.

[34] F. G. Cruz, K.-C. Lam, and K. Burke, “Exchange−Correlation Energy Density from Virial Theorem,” *J. Phys. Chem. A*, vol. 102, no. 25, pp. 4911–4917, Jun. 1998.

[35] W. J. Hehre, R. F. Stewart, and J. A. Pople, “Self-Consistent Molecular-Orbital Methods. I. Use of Gaussian Expansions of Slater-Type Atomic Orbitals,” *J. Chem. Phys.*, vol. 51, no. 6, pp. 2657–2664, Sep. 1969.

[36] R. Fournier, J. Andzelm, and D. R. Salahub, “Analytical gradient of the linear combination of Gaussian-type orbitals—local spin density energy,” *J. Chem. Phys.*, vol. 90, no. 11, pp. 6371–6377, Jun. 1989.

[37] E. R. Davidson and D. Feller, “Basis set selection for molecular calculations,” *Chem. Rev.*, vol. 86, no. 4, pp. 681–696, Aug. 1986.

[38] A. R. Leach, *Molecular modelling principles and applications*, Second ed., Pearson Education Limited, 2001.

[39] G. K. H. Madsen, P. Blaha, K. Schwarz, E. Sjöstedt, and L. Nordström, “Efficient linearization of the augmented plane-wave method,” *Phys. Rev. B*, vol. 64, no. 19, p. 195134, Oct. 2001.

[40] K. Cho, T. A. Arias, J. D. Joannopoulos, and P. K. Lam, “Wavelets in electronic structure calculations,” *Phys. Rev. Lett.*, vol. 71, no. 12, pp. 1808–1811, Sep. 1993.

[41] N. A. Benedek, I. K. Snook, K. Latham, and I. Yarovsky, “Application of numerical basis sets to hydrogen bonded systems: A density functional theory study,” *J. Chem. Phys.*, vol. 122, no. 14, p. 144102, Apr. 2005.

[42] V. Blum, R. Gehrke, F. Hanke, P. Havu, X. Ren, K. Reuter, and M. Scheffler, “Ab initio molecular simulations with numeric atom-centered orbitals,” *Comput. Phys. Commun.*, vol. 180, no. 11, pp. 2175–2196, Nov. 2009.

[43] J. G. Lee, *Computational Materials Science An Introduction*, CRC press, 2012.

[44] D. R. Hamann, M. Schlüter, and C. Chiang, “Norm-Conserving Pseudopotentials,” *Phys. Rev. Lett.*, vol. 43, no. 20, pp. 1494–1497, Nov. 1979.

[45] N. Troullier and J. L. Martins, “Efficient pseudopotentials for plane-wave calculations,” *Phys. Rev. B*, vol. 43, no. 3, pp. 1993–2006, Jan. 1991.

[46] D. G. Truhlar, B. C. Garrett, and S. J. Klippenstein, “Current Status of Transition-State Theory,” *J. Phys. Chem.*, vol. 100, no. 31, pp. 12771–12800, Jan. 1996.

[47] G. Henkelman, G. Jóhannesson, and H. Jónsson, “Methods for Finding Saddle Points and Minimum Energy Paths,” in *Theoretical Methods in Condensed Phase Chemistry*, S. D. Schwartz, Ed. Dordrecht: Springer Netherlands, 2002, pp. 269–302.

[48] T. A. Halgren and W. N. Lipscomb, “The synchronous-transit method for determining reaction pathways and locating molecular transition states,” *Chem. Phys. Lett.*, vol. 49, no. 2, pp. 225–232, Jul. 1977.

[49] C. Peng and H. B. Schlegel, “Combining Synchronous Transit and Quasi-Newton Methods to Find Transition States,” *Isr. J. Chem.*, vol. 33, no. 4, pp. 449–454, 1993.

[50] G. Henkelman, B. P. Uberuaga, and H. Jónsson, “A climbing image nudged elastic band method for finding saddle points and minimum energy paths,” *J. Chem. Phys.*, vol. 113, no. 22, pp. 9901–9904, Nov. 2000.

[51] G. Henkelman and H. Jónsson, “Improved tangent estimate in the nudged elastic band method for finding minimum energy paths and saddle points,” *J. Chem. Phys.*, vol. 113, no. 22, pp. 9978–9985, Nov. 2000.

[52] H. Jónsson, G. Mills, and K. W. Jacobsen, “Nudged elastic band method for finding minimum energy paths of transitions,” in *Classical and Quantum Dynamics in Condensed Phase Simulations*, World Scientific, 1998, pp. 385–404.

[53] “Materials Studio Materials Modeling & Simulation Application | Dassault Systèmes BIOVIA.” [Online]. Available: http://accelrys.com/products/collaborative-science/biovia-materials-studio/. [Accessed: 14-Jun-2018].

[54] B. Hammer, L. B. Hansen, and J. K. Nørskov, “Improved adsorption energetics within density-functional theory using revised Perdew-Burke-Ernzerhof functionals,” *Phys. Rev. B*, vol. 59, no. 11, pp. 7413–7421, Mar. 1999.

[55] B. Delley, “From molecules to solids with the DMol3 approach,” *J. Chem. Phys.*, vol. 113, no. 18, pp. 7756–7764, Oct. 2000.

[56] Y. Gao, N. Shao, Y. Pei, and X. C. Zeng, “Icosahedral Crown Gold Nanocluster Au43Cu12 with High Catalytic Activity,” *Nano Lett.*, vol. 10, no. 3, pp. 1055–1062, Mar. 2010.

[57] H. Li, L. Li, A. Pedersen, Y. Gao, N. Khetrapal, H. Jonsson, and X.C. Zeng, “Magic-Number Gold Nanoclusters with Diameters from 1 to 3.5 nm: Relative Stability and Catalytic Activity for CO Oxidation,” *Nano Lett.*, vol. 15, no. 1, pp. 682–688, Jan. 2015.

[58] Z. Xie, Q.-M. Ma, Y. Liu, and Y.-C. Li, “First-principles study of the stability and Jahn–Teller distortion of nickel clusters,” *Phys. Lett. A*, vol. 342, no. 5, pp. 459–467, Jul. 2005.

[59] G. Rossi, A. Rapallo, C. Mottet, A. Fortunelli, F. Baletto, and R. Ferrando, “Magic Polyicosahedral Core-Shell Clusters,” *Phys. Rev. Lett.*, vol. 93, no. 10, p. 105503, Sep. 2004.

[60] S. Gyawali, S. Godara, F. A. Soto, and D. S. Mainardi, “In Search of Initial Predictors of Fischer Tropsch Catalytic Activity,” *IEEE Trans. Nanotechnol.*, vol. 15, no. 5, pp. 738–745, Sep. 2016.

[61] J. P. K. Doye and L. Meyer, “Mapping the Magic Numbers in Binary Lennard-Jones Clusters,” *Phys. Rev. Lett.*, vol. 95, no. 6, p. 063401, Aug. 2005.

[62] A.K. Datye and J. Schwank, “Fischer-Tropsch synthesis on bimetallic ruthenium-gold catalysts, ” *J. Catal.,* vol.93, no. 2, pp. 256-269, Jun. 1985.

[63] D. K. Limbu, R. Atta-Fynn, D. A. Drabold, S. R. Elliott, and P. Biswas, “Structural properties of transition-metal clusters via force-biased Monte Carlo and ab initio calculations: A comparative study,” *Phys. Rev. B*, vol. 96, no. 17, p. 174208, Nov. 2017.

[64] S. Storsæter, Ø. Borg, E. A. Blekkan, and A. Holmen, “Study of the effect of water on Fischer–Tropsch synthesis over supported cobalt catalysts,” *J. Catal.*, vol. 231, no. 2, pp. 405–419, Apr. 2005.

[65] S. J. Tauster, S. C. Fung, R. T. K. Baker, and J. A. Horsley, “Strong Interactions in Supported-Metal Catalysts,” *Science*, vol. 211, no. 4487, pp. 1121–1125, Mar. 1981.

[66] S. Bagheri, N. Muhd Julkapli, and S. Bee Abd Hamid, “Titanium Dioxide as a Catalyst Support in Heterogeneous Catalysis,” *Sci. World J.*, vol. 2014, 2014.

[67] L. A. J. Garvie, P. Rez, J. R. Alvarez, P. R. Buseck, A. J. Craven, and R. Brydson, “Bonding in alpha-quartz (SiO2): A view of the unoccupied states,” *Am. Mineral.*, vol. 85, no. 5–6, pp. 732–738, 2015.

[68] C. Sun and S. C. Smith, “Strong Interaction between Gold and Anatase TiO2(001) Predicted by First Principle Studies,” *J. Phys. Chem. C*, vol. 116, no. 5, pp. 3524–3531, Feb. 2012.

[69] X.-Q. Gong, A. Selloni, O. Dulub, P. Jacobson, and U. Diebold, “Small Au and Pt Clusters at the Anatase TiO2(101) Surface: Behavior at Terraces, Steps, and Surface Oxygen Vacancies,” *J. Am. Chem. Soc.*, vol. 130, no. 1, pp. 370–381, Jan. 2008.

[70] S. C. Parker and C. T. Campbell, “Reactivity and sintering kinetics of Au/TiO2(110) model catalysts: particle size effects,” *Top. Catal.*, vol. 44, no. 1, pp. 3–13, Jun. 2007.

[71] T. Demuth, Y. Jeanvoine, J. Hafner, and J. G. Ángyán, “Polymorphism in silica studied in the local density and generalized-gradient approximations,” *J. Phys. Condens. Matter*, vol. 11, no. 19, p. 3833, May 1999.

[72] F. Labat, P. Baranek, C. Domain, C. Minot, and C. Adamo, “Density functional theory analysis of the structural and electronic properties of TiO2 rutile and anatase polytypes: Performances of different exchange-correlation functionals,” *J. Chem. Phys.*, vol. 126, no. 15, p. 154703, Apr. 2007.

[73] Y. Cai, Z. Bai, S. Chintalapati, Q. Zeng, and Y. P. Feng, “Transition metal atoms pathways on rutile TiO2 (110) surface: Distribution of Ti3+ states and evidence of enhanced peripheral charge accumulation,” *J. Chem. Phys.*, vol. 138, no. 15, p. 154711, Apr. 2013.

[74] R. C. Brady and R. Pettit, “Reactions of diazomethane on transition-metal surfaces and their relationship to the mechanism of the Fischer-Tropsch reaction,” *J. Am. Chem. Soc.*, vol. 102, no. 19, pp. 6181–6182, Sep. 1980.

[75] J. P. Perdew, K. Burke, and M. Ernzerhof, “Generalized Gradient Approximation Made Simple,” *Phys. Rev. Lett.*, vol. 77, no. 18, pp. 3865–3868, Oct. 1996.

[76] H. J. Monkhorst and J. D. Pack, “Special points for Brillouin-zone integrations,” *Phys. Rev. B*, vol. 13, no. 12, pp. 5188–5192, Jun. 1976.

[77] L. A. J. Garvie, P. Rez, J. R. Alvarez, P. R. Buseck, A. J. Craven, and R. Brydson, “Bonding in alpha-quartz (SiO2): A view of the unoccupied states,” *Am. Mineral.*, vol. 85, no. 5–6, pp. 732–738, 2015.

[78] Y. Cai, Z. Bai, S. Chintalapati, Q. Zeng, and Y. P. Feng, “Transition metal atoms pathways on rutile TiO2 (110) surface: Distribution of Ti3+ states and evidence of enhanced peripheral charge accumulation,” *J. Chem. Phys.*, vol. 138, no. 15, p. 154711, Apr. 2013.

[79] C. Sun and S. C. Smith, “Strong Interaction between Gold and Anatase TiO2(001) Predicted by First Principle Studies,” *J. Chem. Phys.*, vol. 116, no. 5, pp. 3524-3531, 2012.

[80] M. Sakurai, K. Watanabe, K. Sumiyama, and K. Suzuki, “Magic numbers in transition metal (Fe, Ti, Zr, Nb, and Ta) clusters observed by time-of-flight mass spectrometry,” *J. Chem. Phys.*, vol. 111, no. 1, pp. 235–238, Jun. 1999.

[81] W. Chu, P. A. Chernavskii, L. Gengembre, G. A. Pankina, P. Fongarland, and A. Y. Khodakov, “Cobalt species in promoted cobalt alumina-supported Fischer–Tropsch catalysts,” *J. Catal.*, vol. 252, no. 2, pp. 215–230, Dec. 2007.

[82] R. Tran, Z. Xu, B. Radhakrishnan, D. Winston, W. Sun, K.A. Persson, and S.P Ong, “Surface energies of elemental crystals,” *Sci. Data*, vol. 3, p. 160080, Sep. 2016.